

Collective Behavior of Swimming Bimetallic Motors
in Chemical Concentration Gradients.

by

Philip Matthew Wheat

A Dissertation Presented in Partial Fulfillment
of the Requirements for the Degree
Doctor of Philosophy

Approved March 2011 by the
Graduate Supervisory Committee:

Jonathan D. Posner, Chair
Patrick Phelan
Kangping Chen
Daniel Buttry
Ronald Calhoun

ARIZONA STATE UNIVERSITY

May 2011

ABSTRACT

Locomotion of microorganisms is commonly observed in nature. Although microorganism locomotion is commonly attributed to mechanical deformation of solid appendages, in 1956 Nobel Laureate Peter Mitchell proposed that an asymmetric ion flux on a bacterium's surface could generate electric fields that drive locomotion via self-electrophoresis. Recent advances in nanofabrication have enabled the engineering of synthetic analogues, bimetallic colloidal particles, that swim due to asymmetric ion flux originally proposed by Mitchell. Bimetallic colloidal particles swim through aqueous solutions by converting chemical fuel to fluid motion through asymmetric electrochemical reactions.

This dissertation presents novel bimetallic motor fabrication strategies, motor functionality, and a study of the motor collective behavior in chemical concentration gradients. Brownian dynamics simulations and experiments show that the motors exhibit chemokinesis, a motile response to chemical gradients that results in net migration and concentration of particles. Chemokinesis is typically observed in living organisms and distinct from chemotaxis in that there is no particle directional sensing. The synthetic motor chemokinesis observed in this work is due to variation in the motor's velocity and effective diffusivity as a function of the fuel and salt concentration. Static concentration fields are generated in microfluidic devices fabricated with porous walls. The development of nanoscale particles that swim autonomously and collectively in chemical concentration gradients can be leveraged for a wide range of applications such as directed drug delivery, self-healing materials, and environmental remediation.

ACKNOWLEDGEMENTS

I would like to thank my committee comprised of Dr. Patrick E. Phelan, Dr. Kangping Chen, Dr. Daniel A. Buttry, and Dr. Ronald J. Calhoun for all of their help and guidance from my comprehensive exams through my dissertation defense. I especially thank my advisor and committee chair Dr. Jonathan D. Posner for inviting me to be a part of his research team and for his guidance and support throughout my graduate studies at Arizona State University.

I also thank my colleagues in the Posner Research Group who have been great friends and have always been selfless in providing ideas, instruction, and assistance in my work. Specifically I thank Abishek Jain for teaching me how to use the tools in the clean room and how to make PDMS structures. I also want to specifically acknowledge Steve Klein, Guru Navaneetham, Kamil Salloum, Juan Tibaquira, Carlos Perez, Wen-Che Hou, and Charlie Corredor for thoughtful discussions and input throughout my studies. I especially thank Jeffrey Moran and Nathan Marine for their tremendous collaborative effort in my publications accompanying this research. I also thank Babak Yagoupi for staying up late Friday nights making structures with me for the experiments.

I would like to thank the staff in CSSER and CSSS for their instruction and for the use of their facilities throughout my research, especially Grant Baumgardner and Karl Weiss for their help with sample preparation and electron microscopy, and Carrie Sinclair for all of her help securing clean room supplies.

I am extremely grateful to the Marines at the Phoenix Officer Selection Office for their continual efforts to accommodate my studies, specifically Captain

Mark Beasely, Gunnery Sergeant Edgar Arriaga, and Master Sergeant Mike Edmonds (Ret.).

I am eternally grateful to my wife Stacy, and my daughters Kaitlyn, Danielle, and Amanda, who bore the greatest burden of my long hours in the lab and at home studying for the last five and a half years. I also thank my mother, Charlene, for all of her help with the kids.

Finally I wish to thank my father, Dr. Stephen R. Wheat. Without his guidance, encouragement, and support it is doubtful I would have embarked on this journey.

TABLE OF CONTENTS

	Page
LIST OF FIGURES	vi
CHAPTER	
1. INTRODUCTION	1
1.1 Motivation	1
1.2 Literature Review	1
1.3 Significance	4
2. BACKGROUND	6
2.1 Nanomotors	6
2.2 Synthetic Nanomotors	8
2.3 Directional Control.....	10
2.4 Chemical Gradients for Directional Control	12
2.5 Chemotaxis-Chemokinesis Terminology	13
2.6 Biological Chemotaxis	21
2.7 Biological Chemokinesis.....	23
2.8 Synthetic Chemotaxis and Chemokinesis.....	23
2.9 Chemotactic Assays	26
2.10 Chemotactic Measures.....	34
2.11 Bimetallic Nanomotors.....	36

CHAPTER	Page
2.12 Bimetallic Nanomotor Efficiency.....	37
3. THEORETICAL FRAMEWORK.....	40
3.1 Analytical Approach.....	40
3.2 Computational Approach.....	51
4. EXPERIMENTAL METHODS.....	54
4.1 Fabrication of Rod-Shaped Nanomotors.....	54
4.2 Fabrication of Spherical Motors.....	59
4.3 Synthetic Chemokinesis Assays.....	68
4.4 Experimental Apparatus.....	74
5. RESULTS AND DISCUSSION.....	88
5.1 Brownian Dynamics Simulation Results:.....	88
5.2 Variable Diffusion PDE Model:.....	98
5.3 Experimental Results.....	103
6. SUMMARY.....	128
REFERENCES.....	129
APPENDIX	
A MATLAB SIMULATION OPTIONS.....	133
B BROWNIAN DYNAMICS CODE.....	148
C COPYRIGHT RELEASE AGREEMENTS.....	163

LIST OF FIGURES

Figure	Page
1. Motion of motor proteins.....	6
2. F1-ATPase modified nanopropellar.....	7
3. Bacteria driven micro-rotator.....	8
4. Tethered Au-Ni nanorotor.....	9
5. Bimetallic nanomotor hauling cargo.....	10
6. Magnetic field directed Au-Ni-Au-Pt nanorods	11
7. Leukocytes oriented along a gradient	16
8. Depiction of different types of chemotaxis.....	17
9. One-dimensional depiction of an orthokinetic cell.....	19
10. One-dimensional depiction of an orthokinetic cell without walls	20
11. Conceptual design for chemotaxis nanomotor.....	24
12. Depiction of a nanomotor containing nickel.....	25
13. A depiction an Au-Ni-Au-Pt nanomotor attached to cargo	26
14. Boyden chamber.	30
15. Flow cell design	32
16. Schematic of a gold/platinum nanomotor.....	37
17. Effective diffusivity as a function of position.....	48
18. Chemotactic index as a function of time.....	49
19. Bimetallic nanorod fabrication process.	55
20. Exploded view of the electrochemical cell	57
21. Schematic of the fabrication method.	62

Figure	Page
22. Scanning electron microscope image.....	63
23. Representative traces for 3 μm microspheres	67
24. Average bimetallic, spherical micromotor speeds.....	68
25. Nanomotor speed as a function of the electrical resistance.....	70
26. Electrochemical modulation of bimetallic nanomotor speed.....	71
27. Experimental apparatus used by Calvo-Marzal et al.	71
28. Interdigitated working and counter electrode	72
29. Concentration profiles of salt.....	75
30. Schematic of the structure.....	76
31. Exploded view of the gradient generator	79
32. Initial channel structure design.....	82
33. Generation 2 channel design.....	82
34. Generation 3 channel design.....	83
35. Generation 4 channel design.....	83
36. Generation 5 channel design.....	84
37. Final channel design.....	84
38. Micromotor speeds versus H_2O_2	89
39. Average polystyrene sphere speed versus H_2O_2 concentration.....	89
40. Average speed versus silver salt concentration.....	90
41. The inverse of the average rotational diffusivity	90
42. Initial distribution of nanomotors	92
43. Final steady-state distribution of nanomotors.....	94

Figure	Page
44. Chemotactic index phase diagram.	94
45. Chemotactic index versus time.	95
46. Response time vs chemotactic velocity at maximum fuel concentration.	96
47. Normalized motor concentration	100
48. Normalized motor concentration 2	101
49. Comparison between PDE and Brownian dynamics	102
50. Experimental set-up for microscopy.....	104
51. Average nanomotor velocity as a function of position	106
52. Example of a discretized nanomotor path.....	110
53. Total displacement squared.....	110
54. Mean squared displacement	111
55. Average nanomotor effective diffusivity.	111
56. Channel regions used to measure chemotactic index.	112
57. Chemotactic index measured as a function of time	113
58. Vertically-averaged fluorescence intensity.....	115
59. Vertically-averaged fluorescence intensity integrated horizontally	115
60. Initial distribution of nanomotors subject to a linear gradient in KCl.	117
61. Distribution of nanomotors subject to a linear gradient.....	117
62. Histogram contour map.....	118
63. Case 1 results.	119
64. Case 2 results..	120
65. Case 3 results.	120

Figure	Page
66. Case 4 results	121
67. Case 5 results.	121
68. Case 6 results.	122
69. Case 7 results.	122
70. Experimental, Brownian dynamics simulation, PDE model.	123
71. Steady state chemotactic index phase map.	125
72. Response time phase map.	126
73. Steady state chemotactic index vs. $\text{grad}(\text{Deff}) \times w / \text{Deff}, \text{min}$	126

CHAPTER 1

INTRODUCTION

1.1 Motivation

Synthetic nanomotors are of particular interest in the research community because of their potential ability to mimic biological nanomotors. In many cases, biological nanomotors are responsible for delivering cargo to very specific destinations in biological systems. Synthetic nanomotors have been developed that are capable of picking up, transporting, and dropping off cargo. Unfortunately a sufficient method of steering the nanomotors to a specific location has not been developed. Often biological cells utilize variations in the chemical concentrations in their immediate vicinity to move to very specific locations. If synthetic nanomotors were developed capable of responding to chemical concentration gradients as a means of passively guiding them to a destination, it would be a tremendous step in realizing the use of nanomotors for applications such as highly specific drug delivery. There are three distinct locomotive responses to chemical concentration gradients: chemotaxis, chemokinesis, and diffusiophoresis. While chemotaxis and chemokinesis are commonly leveraged in biological systems, to date there is no account of a demonstration of either synthetic chemotaxis or synthetic chemokinesis in the literature.

1.2 Literature Review of Synthetic Nanomotor Responses to Chemical Gradients

Chemotaxis, since its discovery as a means of guiding the direction of motion by

Engelmann in 1881,(Engelmann 1881) has been the topic of more than 22,000 publications. The primary means of determining chemotactic behavior of a cell has been the observation of the global response of large numbers of the cells. Unfortunately, it is quite possible to mistake a global accumulation of cells at the source of a chemical as a chemotactic response, when in actuality it is a purely random diffusive type response. This mistake has been made so frequently in the literature that several articles have been written in attempts to address the pervasive underlying misconceptions that lead to this mistake. In 1973, Zigmond et al. established a crude method of distinguishing between the purely random response and a chemotactic response that is only applicable for a specific type of assay.

In 2007, Hong et al. claimed to demonstrate “the first experimental example of chemotaxis outside biological systems” using synthetic bimetallic nanomotors.(Hong et al. 2007) They used two different types of assay to demonstrate this. First they used the capillary assay in which a capillary is filled with hydrogen-peroxide, capped at one end and then placed in an aqueous solution containing several bimetallic nanomotors. In this case, the evidence of a chemotactic response is the mild accumulation of nanomotors in the capillary over time. The second assay used a gel plug that was saturated with hydrogen-peroxide and then placed in an aqueous solution containing the synthetic nanomotors. In this case, the evidence of a chemotactic response is the global motion of the nanomotors predominantly towards the gel plug. Finally, the authors back up their claim using Brownian dynamics simulations. In the case of

the first assay, it is impossible to say that the accumulation of a small number of the nanomotors in a capillary containing hydrogen-peroxide is the result of chemotactic behavior as oppose to random motion. The authors argue that the increased speed due to the higher concentration of hydrogen-peroxide is necessary for the nanomotors, which are otherwise scurrying along the lower surface of the chamber, to climb up over the lip of the capillary. However, the increased speed would have the same effect on a nanomotor that just happens to be in the region as a result of random motion.

However, if the global behavior of the nanomotors is governed by a purely random process, then the results of the second assay are counter-intuitive. As the nanomotors approach the hydrogen-peroxide saturated gel plug, they should move faster and quickly move away, resulting in higher dwell times at lower concentrations such that the equilibrium distribution of nanomotors shows an accumulation at regions of lower hydrogen-peroxide concentration. Instead, what is reported is an accumulation at the gel plug. There are at least two possible explanations for this discrepancy. First, the nanomotors become stuck in the vicinity of the gel plug and remain there through the duration of the experiment, such that over time the nanomotors accumulate in the vicinity of the gel plug. Second, there is actual chemotaxis taking place in which the nanomotors have a directional bias towards the region of higher concentration. It is difficult to imagine where such a bias might originate when dealing with a simple bimetallic nanorod. If it were due to surface irregularities resulting from the non-precise fabrication process, then one would expect to observe a substantial number of the

nanomotors displaying an opposite bias, down the gradient. Fortunately, there is a video accompanying these results. Upon inspection, one can see that the nanomotors drift towards the gel plug regardless of whether they are oriented towards or away from the gel plug. This is a clear indication that the experiment is invalidated by the presence of a pressure driven or otherwise generated superimposed flow, or the global behavior observed may be a dominating diffusiophoretic response. Furthermore, the authors' supporting Brownian Dynamics simulation admittedly incorporated a slight bias directed toward higher hydrogen-peroxide concentrations. Such a bias is necessary for a chemotactic response, but again is not characteristic of bimetallic nanomotors.

1.3 Significance

Here, I present Brownian dynamic simulations I use to argue that the global behavior of synthetic nanorods, as currently, constructed is limited to chemokinesis and without modification will not exhibit any form of chemotactic response. Furthermore, I experimentally validate these conclusions. For this work, I fabricated two different types of bimetallic nanomotors. First I use the traditional bimetallic nanorods that I fabricated using the methods prescribed in the literature.(Paxton et al. 2004) Then I use bimetallic spherical motors that I fabricated using a technique that I developed and recently published in Langmuir.(Wheat et al.) My experimental approach utilizes the structure conceived by Diao et al. and used by Palacci et al. for the purpose of studying diffusiophoresis.(Palacci et al. 2010) This approach provides substantial

improvement over most chemotaxis and chemokinesis assays in that it generates a static spatial chemical concentration gradient without flow. Using these experiments I demonstrate the first case of synthetic chemokinesis. The Brownian Dynamics model can be used to predict the chemokinetic component of a perceived chemotactic response in both biological and synthetic systems. Finally, results of the model are reduced to a partial differential equation that can be solved rapidly for a quantitative analysis of the global behavior of chemokinetic cells.

CHAPTER 2

BACKGROUND

2.1 Nanomotors

The term nanomotor refers to an object less than a micrometer in one or more spatial dimension that takes a form of non-mechanical energy and converts it into mechanical work. Biological nanomotors, sometimes referred to as molecular motors, have long been known to exist in the form of protein motors and nucleic acid motors. Nucleic acid motors include RNA polymerases, which transcribe RNA from DNA, and DNA polymerases, which produce double-stranded DNA from single stranded DNA. Protein motors include myosins, which are responsible for muscle contractions, kinesins, which carry cargo along microfilaments within a cell, and dyneins, which are responsible for ciliary and flagellar motility.(Bloom 1996) Figure 1 depicts the typical motion of the different types of motor proteins.

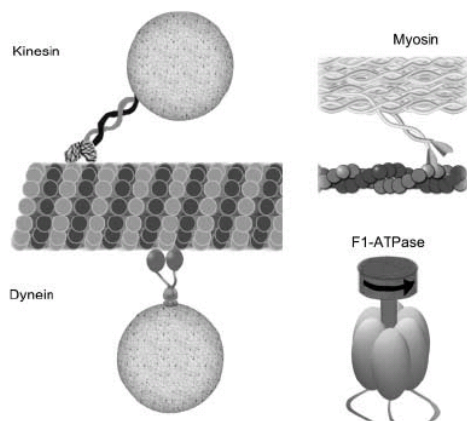


Figure 1: Motion of motor proteins and an F1-ATPase rotator. Hess, H., Bachand, G. D. & Vogel, V. *Powering nanodevices with biomolecular motors. Chemistry-a European Journal* 10, 2110-2116 (2004). Copyright Wiley-VCH Verlag GmbH & Co. KGaA. Reproduced with permission.

The existence and functionality of dynein were accurately predicted as early as 1965(Gibbons 1965) and were proven in 1987.(Paschal, Shpetner and Vallee 1987) In the following decade work was done to characterize protein motors, such as determining the force a kinesin protein is capable of exerting.(Meyhofer and Howard 1995) During the late 1990's and early 2000's, research efforts shifted towards incorporating protein motors into synthetic systems to create functionally specific, hybrid bio-synthetic nanomotors.(van den Heuvel and Dekker 2007) In one instance, a synthetic nanorod was attached to an F₁-ATPase (a protein dubbed factor F1 that synthesizes Adenosine Triphosphate) motor to create a hybrid bio-synthetic nanopropellar (Figure 2).(Soong et al. 2000) In another instance, a microrotor powered by bacteria was created by confining unidirectionally swimming bacteria in a rotor track (Figure 3).(Hiratsuka et al. 2006)

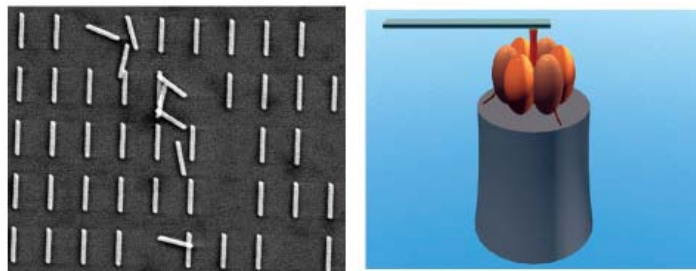


Figure 2: F1-ATPase modified nanopropellar. From [Soong, R. K. et al. *Powering an inorganic nanodevice with a biomolecular motor. Science* 290, 1555-1558 (2000)]. Reprinted with permission from AAAS. <http://dx.doi.org/10.1126/science.290.5496.1555>

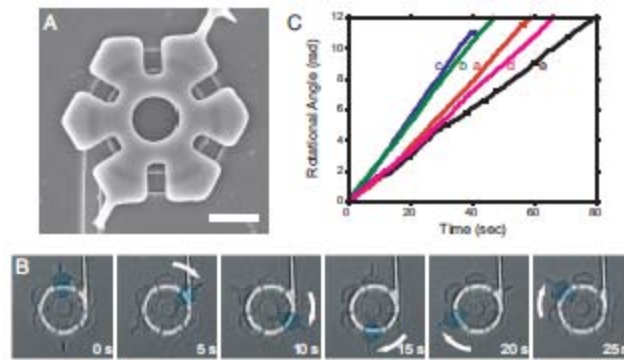


Figure 3: Bacteria driven micro-rotator. *Hiratsuka, Y., Miyata, M., Tada, T. & Uyeda, T. Q. P. A microrotary motor powered by bacteria. Proceedings of the National Academy of Sciences of the United States of America 103, 13618-13623 Copyright (2006) National Academy of Sciences, U.S.A. <http://dx.doi.org/10.1073/pnas.0604122103>*

2.2 Synthetic Nanomotors

Within the past decade, efforts have shifted towards the development of fully synthetic nanomotors in an effort to take advantage of the relative experimental simplicity associated with non-biological environments. In 2004, Paxton et al. discovered the autocatalytic motion of bimetallic nanorods in the presence of hydrogen peroxide. (Paxton et al. 2004) In this seminal work, the nanorods were 370 nm in diameter with adjoined 1 μm gold and 1 μm platinum segments. In 2 to 3% hydrogen-peroxide the nanomotor velocities were on the order of 10 body lengths per second. Paxton et al. observed the dimensions and velocities to be comparable to multiflageller bacteria.

Shortly thereafter, Fournier-Bidoz et al. published their discovery of a different bimetallic combination that also exhibited autonomous motion in the presence of hydrogen-peroxide.(Fournier-Bidoz et al. 2005) In the Fournier-Bidoz et al. paper, the nanorods were half gold and half nickel, with one side tethered to a substrate these nanorods behaved as nanorotors, pivoting around the attachment point. These papers sparked significant research interest in bimetallic nanomotors. In 2005, Catchmark et al. produced gold gears 150 μm in diameter with a platinum coating on only one side of each cog, resulting in autonomous rotation in the presence of hydrogen-peroxide.(Catchmark, Subramanian and Sen 2005) In 2008, we collaborated with Burdick, Laocharoensuk, and Wang to demonstrate nanomotors capable of picking up, hauling, and releasing micron-scale cargo.(Burdick et al. 2008) Sundararajan et al. demonstrated similar capabilities the same year. (Sundararajan et al. 2008)

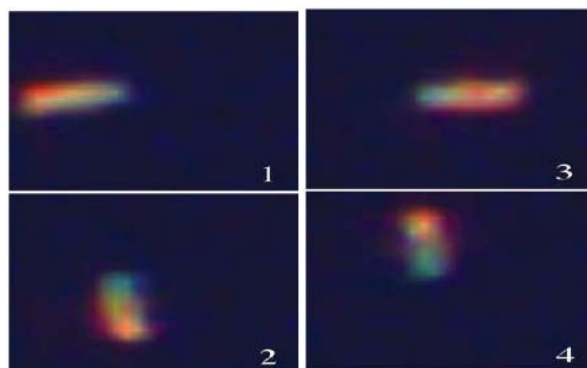


Figure 4: Tethered Au-Ni nanorotor. [Fournier-Bidoz, S., Arsenault, A. C., Manners, I. & Ozin, G. A. *Synthetic self-propelled nanorotors. Chemical Communications*, 441-443 (2005).]– Reproduced by permission of The Royal Society of Chemistry <http://dx.doi.org/10.1039/b414896g>

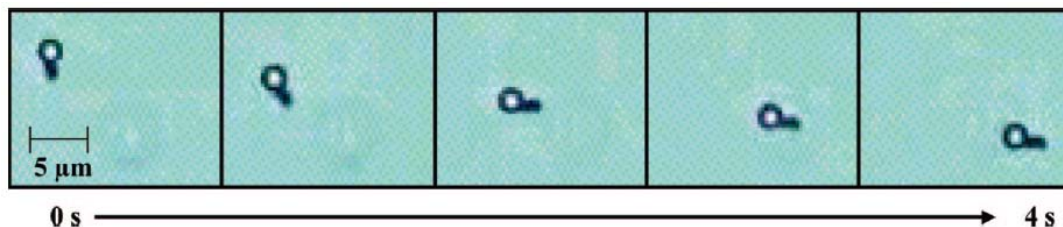


Figure 5: Bimetallic nanomotor hauling cargo. Adapted with permission from Sundararajan, S., Lammert, P. E., Zudans, A. W., Crespi, V. H. & Sen, A. *Catalytic motors for transport of colloidal cargo.* *Nano Letters* 8, 1271-1276. Copyright 2008 American Chemical Society. <http://dx.doi.org/10.1021/nl072275j>

2.3 Directional Control

Currently significant research efforts in the nanomotor field are focused on directional control, particularly the ability to guide the nanomotors to a specific destination for the purpose of delivering cargo or for self-assembly processes. Their motion can be controlled using external magnetic fields(Sundararajan et al. 2008; Burdick et al. 2008) as well as chemical([Calvo-Marzal et al. 2009](#); [Ibele, Mallouk and Sen 2009](#); [Hong et al. 2007](#)) and thermal([Balasubramanian et al. 2009](#)) fields. In 2008, we demonstrated the use of magnetic fields to guide gold-nickel-gold-platinum nanorods through a PDMS channel network.(Burdick et al. 2008)

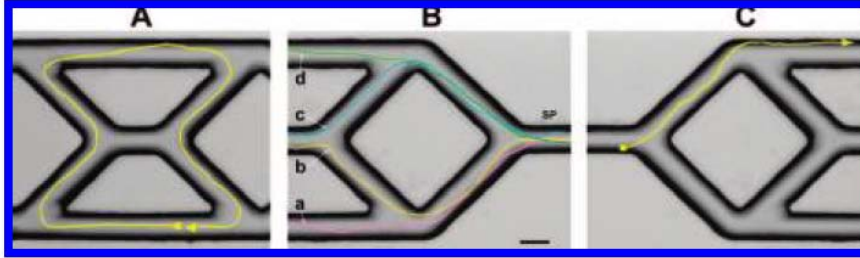


Figure 6: Magnetic field directed Au-Ni-Au-Pt nanorods through a PDMS channel network. *Adapted with permission from Burdick, J., Laocharoensuk, R., Wheat, P. M., Posner, J. D. & Wang, J. Synthetic nanomotors in microchannel networks: Directional microchip motion and controlled manipulation of cargo. Journal of the American Chemical Society 130, 8164-+ Copyright 2008 American Chemical Society. <http://dx.doi.org/10.1021/ja803529u>*

Calvo-Marzal et al. demonstrated the ability to accelerate and decelerate nanomotors by varying local oxygen concentrations in the presence of electric fields sufficiently small to preclude electrophoretic effects, but large enough to electrochemically affect the local concentrations of oxygen.(Calvo-Marzal et al. 2009) Autonomous micromotors composed of AgCl have been shown to asymmetrically decompose when exposed to UV illumination resulting in local chemical concentration gradients inducing a diffusiophoretic response. In this case the angle and intensity of the illumination can be manipulated to control the global behavior of the motors. Balasubramanian et al. demonstrated a linear relationship between temperature and bimetallic nanorod speed and the ability to thermally modulate the speed of nanomotors.(Balasubramanian et al. 2009)

2.4 Chemical Gradients for Directional Control

For most perceived future nanomotor applications, it would be ideal to guide the nanomotors to their destination without the use of externally applied fields. Two distinct types of such passive guidance that have been observed in biological systems in response to chemical concentration gradients are chemotaxis and chemokinesis. For the purposes of drug delivery, it would be ideal for nanomotors carrying cargo to passively seek out the location in the body where the drugs are needed. It has been shown that surface wounds emanate hydrogen-peroxide, and it is suspected that the resulting gradient in hydrogen-peroxide concentration is the signal that guides leukocytes to the wound for healing. If nanomotors could be engineered to swim up such gradients, it is conceivable that drugs aiding in the healing of a wound could navigate to the wound in response to the increase in hydrogen-peroxide concentration at that location. Thus far, very limited work has been done to determine the chemotactic potential of synthetic nanomotors.(Hong et al. 2007) Furthermore, while there has been an enormous amount of research on biological chemotaxis and chemokinesis over the past 122 years, there is still a lot that is not well understood. Basic questions, such as whether or not active-directional sensing is a necessary component for chemotaxis, persist in the literature.(Hong et al. 2007) There is a lot of confusion in the field on terminology and how to distinguish between the purely random responses to chemical gradients characteristic of chemokinesis and the directional sensing nature of chemotaxis.

2.5 Chemotaxis-Chemokinesis Terminology

In 1881, Engelmann first postulated the concept of chemotaxis, wherein a cell would navigate to sources of chemical concentration gradients.(Engelmann 1881) This type of navigation was first observed in bacteria by Pfeffer and in Leukocytes by Leber in 1888.(Pfeffer 1888; Leber 1888) Since then, there have been more than 22,000 papers on the topic of chemotaxis. Many of the papers focus on what cells exhibit chemotaxis and what chemicals trigger chemotactic responses. Other papers focus on the fundamental mechanisms of chemotaxis in efforts to determine how cells sense gradients, whether or not temporal or spatial sensing are required, whether or not cells or the chemicals they are sensing or both have to be surface bound, etc. However, in 1973, Zigmond et al. pointed out a fundamental flaw in many of the preceding assays used to determine whether or not cells exhibited a chemotactic response to certain chemicals.(Zigmond and Hirsch 1973) In nearly all of the chemotactic assays, the chemotactic response was measured by analyzing the end state distribution of cells. For example, if cells were initially distributed uniformly across two regions, one region having a particular chemical in question, and the other region not having the chemical, and then the cells tended towards a non-uniform equilibrium, then the cells were said to have responded chemotactically to the chemical. However, as Zigmond points out, a non-uniform equilibrium response could be due to purely random motion. For example, if a cell swims faster in higher concentrations of a certain chemical but its orientation is random, then the motion will continue to be random in the presence of a concentration gradient of that chemical. If that cell and the chemical

concentration gradient are both located in a bounded region with reflective walls, then the region within the chamber with the lowest chemical concentration will ultimately be the region with the greatest accumulation of cells. This accumulation is because the cells go slower in the region of low concentration and end up having a higher dwell time in that region than in the high concentration regions where they speed through. This accumulation is a response to the chemical concentration gradient, but it is a response that comes about because of purely random motion and can not to be considered chemotaxis. In 1981, Dunn wrote a chapter in a book edited by Wilkinson underscoring the importance of making this distinction between purely random motion, which he calls chemokinesis, and chemotaxis.(Dunn 1981) As Dunn points out, if the walls of the bounded region were removed, these particular cells would diffuse infinitely to a concentration of nearly zero everywhere including the region with the low chemical concentration. On the other hand, if a cell were exhibiting true chemotactic behavior, when the bounding walls are removed, the cell will eventually find its way towards or away from the source of the chemical concentration gradient, depending on whether it is attracted or repelled by that chemical. In chemotaxis, containing walls are not required for the accumulation of cells at a source or sink of a particular chemical concentration this allows for the process to be a long distance process where a single cell will eventually reach its destination. In chemokinesis, the strength of the accumulation of cells is dependent on the proximity of the walls, and at steady state there is a non-uniform pseudo-equilibrium distribution throughout the bounded region with cells

randomly moving in and out of the region of accumulation.

Both Dunn's 1981 chapter and Wilkinson's 1998 review article on chemotaxis attempt to realign the field of chemotaxis with the following internationally accepted, but far too frequently neglected, terminology:

Chemotaxis is where chemical substances, more specifically gradients in concentration of chemical substances, alone determine the direction of locomotion. A form of directional sensing is absolutely necessary for chemotaxis. This can be accomplished using spatial or temporal sensing mechanisms. A chemotactic response cannot come about by purely random locomotion. An additional point of confusion in the literature is the mistaken idea that the orientation of the cell or object must be in alignment with gradients in chemical concentration, as is the case with leukocytes, see Figure 7. E-coli, on the other hand, will travel with a constant speed in some arbitrary direction, then stop, reorient (or tumble), and then travel (or run) at that same speed in a new direction (termed "run and tumble" behavior). The frequency of tumbling events increases as the bacteria moves down the gradient in concentration of certain chemicals. The bacteria use a temporal sensing mechanism to determine the current concentration is greater than a previous concentration. As a result, once the E-coli bacteria reach a peak in concentration, they begin tumbling very frequently because every direction results in a decrease in concentration. The net result being that they migrate towards a peak in concentration where they linger. In this case, the orientation of the cell is random with persistence (which comes about from the temporal sensing mechanism) in the direction of increasing concentration.

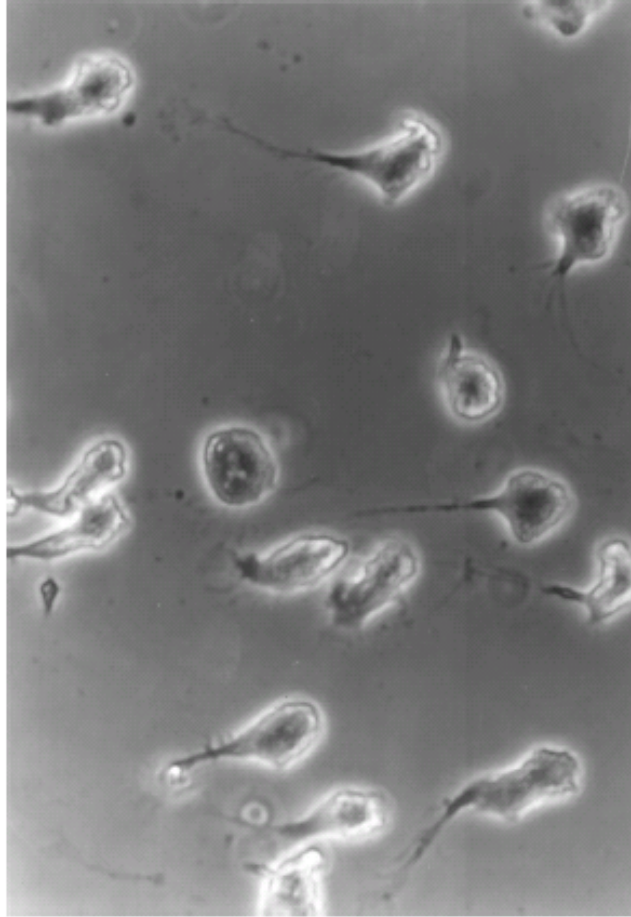


Figure 7: Leukocytes oriented along a gradient in chemoattractant concentration, with the source to the right of the image. *Reprinted from Zigmond, S. H. "Ability of Polymorphonuclear Leukocytes to Orient in Gradients of Chemotactic Factors." Journal of Cell Biology 75.2: 606-16., Copyright (1977), with permission from Elsevier.*

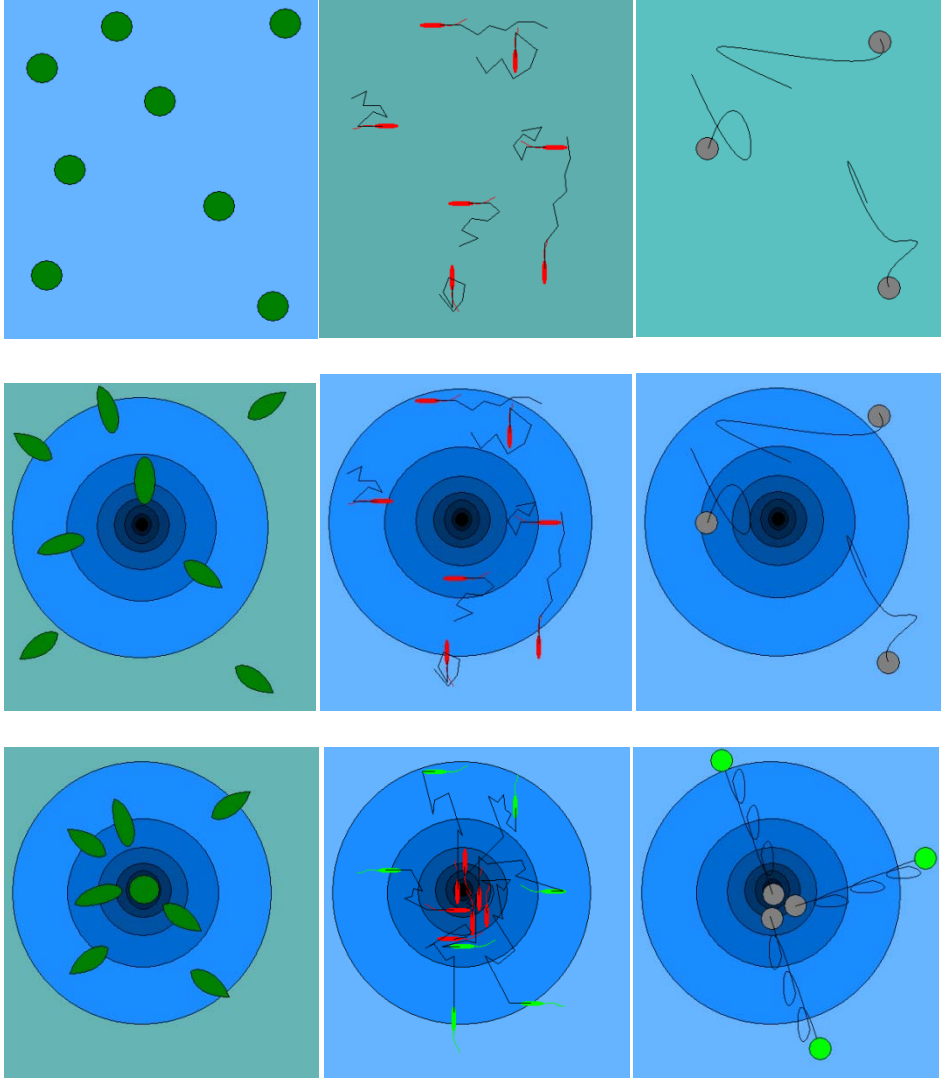


Figure 8: Depiction of different types of chemotaxis, a) gradient aligned migration (as is the case with leukocytes), b) random walk behavior with a temporal sensing mechanism such that the rate of turning increases when the object is moving down the gradient and decreases when moving up the gradient (as is the case with *E. coli*), c) biased random motion with a persistence in the direction of increasing concentration.

Chemokinesis is where chemical substances determine the speed and/or turning frequency (or rotational diffusivity). The subcategories of chemokinesis are **orthokinesis** where the speed is only determined by the chemical substances and **klinokinesis** where only the turning frequency is determined by the chemical substances. Furthermore, the changes in speed or turning frequency corresponding to changes in chemical concentration are termed **chemokinetic** responses. It is possible, and in many cases necessary, for an object undergoing chemotaxis to exhibit chemokinetic responses.

To further clarify the distinction between chemotaxis and chemokinesis, consider a one dimensional scenario with a single object subject to a chemical gradient in a region bound by two reflective walls as shown in Figure 9. First consider a cell that exhibits orthokinesis. The cell travels in one direction until it encounters a boundary and then it travels in the other direction until it encounters the other boundary, and so on. The chemical present causes the object to travel slow in high concentrations and fast in low concentrations. There is a linear concentration gradient with very low concentrations on the left side and very high concentrations on the right side. As a result, the object moving from the right wall to the left wall travels very slowly at first and then speeds up and quickly moves through the region to the left side encountering the wall and quickly moving back towards the right when it begins to slow down again and very slowly approaches the right wall. Over time, the object spends an equal time moving up the gradient as it does moving down the gradient. However, the object clearly spends more time located in the region of high concentration on the right where it is moving

very slowly. Furthermore, if one were to extend this example to include several objects that do not interact with each other, then an accumulation of the objects would appear in the region of higher concentration. This sort of behavior is exactly what is often mistaken for chemotaxis. In reality, this is chemokinesis.

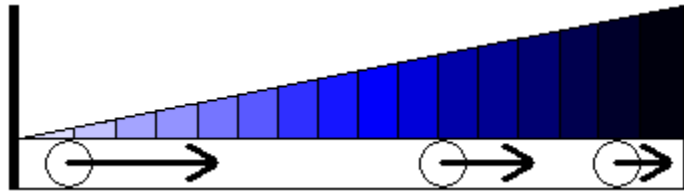


Figure 9: One-dimensional depiction of an orthokinetic cell bound by reflective walls on the left and right subject to a chemical concentration gradient, where the velocity decreases with an increase in concentration.

Now consider a second scenario in which the same region is used, but the object in question utilizes a directional sensing mechanism that causes it to move very fast when the chemical concentration is increasing and very slowly when the chemical concentration is decreasing. Also modify the object such that it turns around at regular time intervals. As a result, the object will move large distances to the right when facing the right, and then when facing the left it will not move very far at all, resulting in a ratcheting motion to the right. Even though half of the time the object is oriented to the left, its net motion is always to the right, where it will linger when it reaches the maximum concentration. Again, if this example were extended to include several objects that do not interact with each other, then an accumulation of the objects would appear in the region of higher concentration. In this case, the observed behavior is chemotaxis.

In both scenarios, the objects spend more time on the right side of the chamber. As a result, both objects may appear to exhibit chemotaxis. An obvious distinction is that chemotaxis results in a continued migration towards the region of accumulation, whereas chemokinesis ultimately reaches a non-uniform pseudo equilibrium distribution. Unfortunately this distinction is less obvious experimentally where most objects exhibiting chemotaxis have a substantial portion of the population that is defective and does not respond to the chemical concentration gradient. The defective population causes the end-state distribution to appear as a non-uniform pseudo-equilibrium distribution. However, if the objects truly exhibited chemotaxis, then if the chemical concentration were mirrored about the right wall and both walls were removed, as shown in Figure 10; the objects would find their way to the region of maximum chemical concentration. However, if the walls, which are the only means of reorienting the object in the first scenario, are removed in the first scenario, then the object will clearly wander increasingly far from the maximum chemical concentration. In the second scenario, the object would still work its way towards the maximum in chemical concentration, exhibiting true chemotaxis.

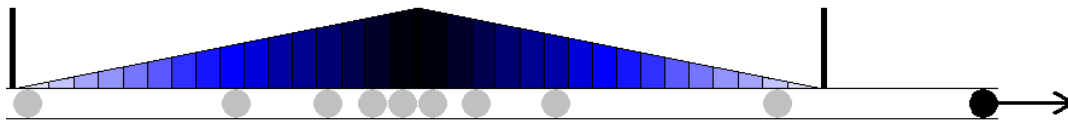


Figure 10: One-dimensional depiction of an orthokinetic cell without walls subject to a chemical concentration gradient, where the velocity decreases with an increase in concentration.

2.6 Biological Chemotaxis

Several different types of cells have been observed to respond to the presence of certain chemicals, called **chemoattractants** (or **chemokines** if they are proteins secreted from cells), by working their way up gradients in concentration of that chemical, seeming to seek out or forage for regions of maximum concentration. This behavior is referred to as **positive chemotaxis**. In some cases the cells migrate down gradients in chemical concentration, the chemical in this case is frequently referred to in the literature as a **toxin** or a **chemorepellent**. In such cases, the behavior is referred to as **negative chemotaxis**.

The most studied cell that exhibits chemotaxis is *Escherichia coli* (E-coli) which propels itself using flagellar motors and works its way up concentration gradients of chemicals such as MeAsp (α -methyl-DL-aspartate) and down concentration gradients of chemicals such as NiCl_2 . (Mello and Tu 2007; Sourjik and Berg 2002) The motion of chemotactic bacteria is typically characterized as random walk. The E-coli bacteria swim in relatively straight lines for periods in which the flagellar motors are rotating in one direction, and then the bacteria tumble and rotate relatively quickly when the motors are reversed. The tumbling motion has the effect of reorienting the bacteria such that subsequent straight motion will be in a different direction. The time between tumbling events appears random with a dependence on the gradient in local concentrations of attractants and repellents. When the concentration of a chemoattractant increases or a chemorepellent decreases, the bacteria swim straight for longer periods (i.e. have lower turning frequencies). As the concentration of a chemoattractant decreases or a

chemorepellent increases, the turning frequency increases reducing the movement in less favorable directions.

The E-coli bacteria has been shown to have a temporal sensing mechanism that initiates changes in turning frequency based on receptor binding events.(Brown and Berg 1974) At each moment in time, the cell compares the current chemoattractant concentration with the concentration from some previous time. If the current concentration is lower than the previous, the turning frequency increases and vice versa. The velocity of the E-coli bacteria during the run portion of the run and tumble behavior is independent of the chemoattractant concentration. Different chemotaxiing cells have been observed with fundamentally different chemokinetic responses. The chemotaxiing planktonic bacteria *P. haloplanktis* increases velocity and turning frequency with increasing chemoattractant concentrations.(Seymour et al. 2008) In both cases, positive chemotaxis is observed, with entirely different responses to increased concentrations. Leukocytes have an entirely different chemotactic mechanism as well. Leukocytes, which are otherwise spherically shaped, elongate when exposed to chemoattractants. They swim in the direction that their long axis points in, and that direction is random in the absence of a gradient in the chemoattractant concentration. When subject to a gradient in the chemoattractant concentration the long axes align with the gradient and the cells swim up the gradient. These cells also have a distinctly orthokinetic response, accompanying their directional sensing abilities. As the local chemoattractant concentration increases, so does the translational velocity.

2.7 Biological Chemokinesis

For every three papers focused on biological chemotaxis there has been one focused on biological chemokinesis. Chemokinesis has sparked less interest because it is not an effective means of long distance navigation. However, in many cases chemotaxis has been shown not to be the cause of observed biological migration. In 2007, Inamdar et al. identified the primary purpose of the jelly coat of a sea urchin egg is to locally increase the motility of the sperm and thereby the sperm-egg collision frequency. The response of sperm to the extracellular jelly coat is purely chemokinetic without any directional sensing component. In this case a chemical concentration gradient is established to guide cells via chemokinesis. Other cells have been shown to exhibit chemokinesis including human sperm,(Ralt et al. 1994) human neural cells,(Richards et al. 2004) and several types of bacteria.(Brown et al. 1993)

2.8 Synthetic Chemotaxis and Chemokinesis

It has been suggested that synthetic nanomotors exhibit chemotaxis in fuel concentration gradients.(Hong et al. 2007) At low concentrations of hydrogen-peroxide (less than 5 wt %), both spherical and rod-shaped nanomotor exhibit a chemokinetic response as their velocities have been shown to increase roughly linearly with an increase in hydrogen –peroxide.(Laocharoensuk, Burdick and Wang 2008; Wheat et al.) This chemokinetic relationship parallels the biological response of certain cells that exhibit chemotaxis and all cells that exhibit

chemokinesis, but does not involve any directional sensing. Therefore, the bimetallic nanomotors can be expected to mimic biological motors that utilize chemokinesis. However, in order for synthetic, bimetallic, nanomotors to exhibit chemotaxis, they would have to incorporate some form of temporal or spatial concentration gradient sensing abilities. This is clearly not present in the case of the simple bimetallic nanorods. However, it is possible to design synthetic motors in a way that effectively incorporates a spatial sensing capacity. Consider a bimetallic rod modified as shown in Figure 11 with a non-conducting segment leading to a smaller perpendicularly oriented bimetallic segment. This perpendicular segment would induce a rotational component that will cause the motor to rotate faster when the tail is in higher concentrations, and slower in lower concentrations such that as the nanomotor circles around it moves further when facing up the gradient than it does when facing down the gradient. The end result would be a ratcheting behavior up the concentration gradient.



Figure 11: Conceptual design for a gold-platinum nanomotor that would undergo chemotaxis in a hydrogen-peroxide concentration gradient, the black segment is non-conducting.

In previous work, we joined nanomotors containing a nickel segment to polystyrene spheres with super paramagnetic iron oxide nanocrystal shells, as shown in Figure 12.(Burdick et al. 2008) In this work, I present a method of coating polystyrene spheres such that half of the surface is covered with one metal, and the other half with another, creating a bimetallic spherical motor. One approach to realizing a synthetic motor capable of directional sensing as depicted in Figure 11, would be to coat a magnetic sphere to make it a bimetallic motor, and then join that to a nanorod containing a nickel segment, as shown in Figure 13. Such a combination would result in a ratcheting behavior up a chemical concentration gradient and could be the first case of synthetic chemotaxis.

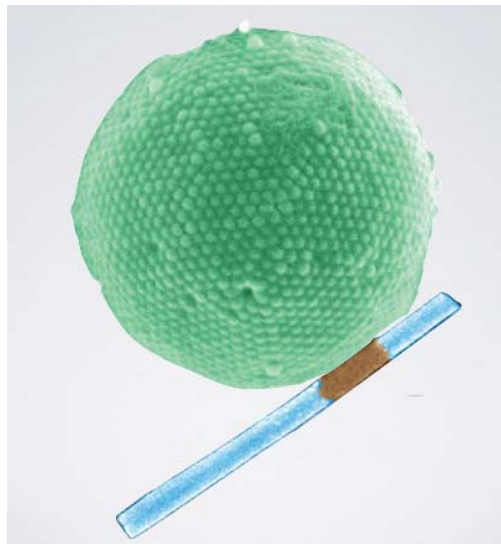


Figure 12: Depiction of a nanomotor containing a nickel segment joined to a polystyrene sphere with a super paramagnetic iron oxide nanocrystal shell.

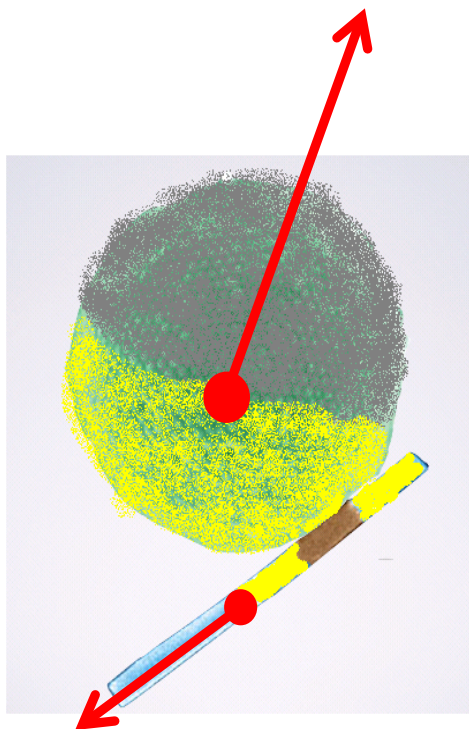


Figure 13: A depiction an Au-Ni-Au-Pt nanomotor attached to a magnetic microsphere that is half coated in gold and half coated in platinum, resulting in a chemotaxis capable synthetic motor.

2.9 Chemotactic Assays

There are a variety of assays for studying chemotaxis and chemokinesis, but until recently, none of these were ideal. An ideal assay incorporates a steady gradient in chemoattractant concentration and the ability for the object being tested for a chemotactic response to pass from low concentration to high concentration and then back down again without trapping the object.

One type of chemotactic assay utilizes a capillary containing the chemoattractant and capped at one end. The capillary is placed in a solution containing the

chemotactic object (cell or motor), and the chemoattractant diffuses out of the capillary into the solution setting up a transient gradient in fuel concentration.(Hong et al. 2007) If the diffusion of the attractant is slow relative to the response of the cells or motors, then the capillary provides a local, high attractant concentration. When the attractant diffuses to motors or cells capable of positive chemotaxis, the motors or cells will migrate up the concentration gradient and into the capillary. Over time, all chemotactically functional motors or cells will accumulate in the capillary. At even longer times, the attractant will diffuse towards a uniform distribution throughout the system, and the motors or cells will also diffuse back to a uniform distribution. If the motors or cells exhibit negative chemotaxis (i.e. the attractant is a toxin/repellent), then all of the functional motors or cells will migrate towards the regions of the system far away from the capillary opening where the concentration is lowest.

If the motors or cells exhibit positive orthokinesis and negative (or no) klinokinesis they will, and the system is enclosed, then the motors will migrate with asymmetric diffusion towards a non-uniform equilibrium distribution, with an accumulation at the low attractant concentration region far away from the capillary opening. It is important to note this is distinct from the negative chemotaxis case because in this case there will still be motors migrating both up and down the concentration gradient and at equilibrium there will be no net flux of motors or cells and there will be motors or cells in the capillary.

The appeal of this assay is its simplicity. It is very easy to fill a capillary, cap an end, and place it in a solution containing motors or cells. Furthermore, the lip of the capillary reduces the number of motors that enter by pure random motion, as the thickness of the side walls of the capillary must be overcome by random vertical displacement. For cells or motors that generally settle and move along the lower surface of a chamber, very few will enter the capillary without a deterministic motion up the gradient. This barrier makes it easier to distinguish between chemotaxis and negative orthokinetic and positive (or no) klinokinetic response.

This approach is less than ideal and cannot be used to adequately analyze the chemotactic ability of bimetallic-nanomotors in hydrogen-peroxide for two reasons. First, the diffusivity of the hydrogen-peroxide is much higher than the effective diffusivity of the bimetallic-nanomotors resulting in a transient gradient. Second, the capped capillary does not allow for the nanomotors to pass through the high concentration and move back into lower concentrations without turning around. The turnaround time results in artificially high dwell times at the higher concentrations, an effect that is difficult to distinguish from a chemotactic response. Using Brownian Dynamic simulations we showed that trapping a motor in a high or low attractant concentration region greatly increases the concentration of motors in that region even if the motors or cells do not exhibit chemotaxis or chemokinesis in response to the attractant, and the motion of the motors or cells is governed purely by diffusion. Furthermore, a cell or motor that

exhibits positive orthokinetic response to an attractant will accumulate away from the region of high concentration, but if the motor or cell is impeded or temporarily trapped in the high concentration region, the accumulation may occur in the high concentration region.

In 1962, Boyden developed an assay specifically designed to study the chemotactic response of cells that behave like leukocytes.(Boyden 1962) Such cells are initially spherical and become elongated in the direction of motion when subjected to a chemoattractant. The assay consists of a chamber (now called the Boyden chamber depicted in Figure 14) divided into two regions by a filter designed such that the pores are too narrow for the spherical shaped cells to pass through, but large enough for the cells in the elongated configuration to pass through. One region contains the chemoattractant and the other region contains the cells. The two regions behave as reservoirs such that the chemoattractant concentration is assumed to develop a linear gradient through the depth of the filter. Since then, variations of the Boyden chamber have been the primary method for studying biological chemotaxis. This method is attractive because it is relatively easy to set up multiwell plates where each well is an individual Boyden chamber for high throughput screening of chemicals that may incite either chemokinesis or chemotaxis for a particular motor or cell. Unfortunately there is no way to observe the motion of the motors or cells within the gradients. As has been pointed out on a number of occasions by Zigmond, Dunn, and Wilkinson, observing an end state accumulation of cells in the region containing the

chemoattractant does not allow for a distinction between chemotaxis and chemokinesis.(Zigmond and Hirsch 1973; Wilkinson 1998; Dunn 1981) This approach can only be done to analyze chemotaxis if the chemokinetic responses are fully characterized and used to predict the response that is due to chemokinesis. A deviation from this response would imply chemotaxis.

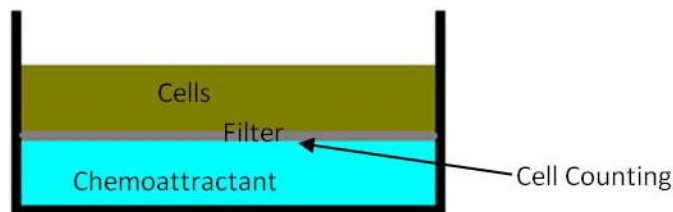


Figure 14: Boyden chamber.

In general, in a bound system, it is difficult to distinguish between a non-uniform pseudo-steady state accumulation of motors or cells due to chemokinesis and a non-uniform distribution that arises due to chemotaxis with a chemotactic potential $< 100\%$. The chemotactic potential is the percent of chemotactic motors or cells in a sample of that are functional. The most straight forward approach to distinguish between chemotaxis and chemokinesis is to visualize the motion of the motors or cells in the gradient. If the motors systematically work their way up or down the gradient, then an observed accumulation is likely chemotaxis. On the other hand, if the motors traverse high and low concentration region multiple times in the development of the accumulation, then the accumulation is the result of chemokinesis. One approach that allows for migration visualization is the use of flow cells. Flow cells are a widely used alternative approach that allows for a

steady chemoattractant gradient.(Saadi et al. 2006; Lin and Butcher 2006) The flows cells are microfluidic devices that funnel two inlets to a single channel where the cells are allowed to diffuse as shown in Figure 15.(Lin and Butcher 2006) This design results in a spatially steady concentration gradient that can be leveraged if the flow of the chemoattractant has a much higher Peclet number than the flow of the chemotactic objects or cells. Such a scenario is achieved if either the diffusivity of the chemotactic object is much higher than the diffusivity of the chemoattractant, or the downstream velocity of the chemotactic object is much lower than the downstream velocity of the chemoattractant. The latter is achieved by using cells that are adsorbed to the surface of the flow cell and have a minimal Stokes-drag profile.(Lin and Butcher 2006) This approach cannot be applied to the bimetallic nanomotors produced to date because they become completely fixed when adsorbed to channel surfaces and otherwise have a much slower diffusivity than hydrogen-peroxide and have non-negligible Stokes drag such that they advect downstream with the velocity of the flow. Either the chemotactic object needs to be faster than diffusion if it is freely swimming or if the cell is adhered to the bottom plate then it is relatively unaffected by the flow. Nanomotors are freely swimming so in that case you need their effective diffusivity to be higher than the diffusivity of the chemoattractant. Unfortunately the effective diffusivity of the motors at the highest speeds achieved to date is an order of magnitude less than the diffusivity of hydrogen peroxide.

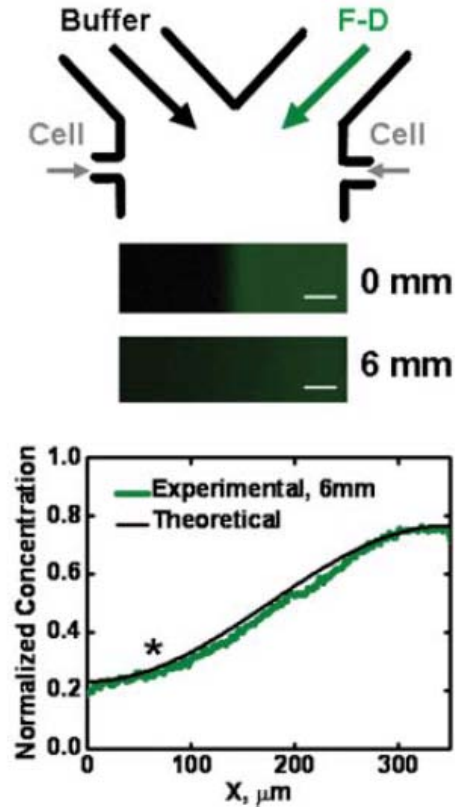


Figure 15: Flow cell design used by Lin and Butcher to measure the chemotactic response of T cells to various chemokines. Lin, F., and E. C. Butcher. "T Cell Chemotaxis in a Simple Microfluidic Device." *Lab on a Chip* 6.11 (2006): 1462-69. – Reproduced by permission of The Royal Society of Chemistry <http://dx.doi.org/10.1039/b607071j>

In 2008, Seymour et al. used a three stream flow cell in which the center channel introduced a relatively slow diffusing chemoattractant, and the outer two channels introduced a salt water solution containing fast swimming oceanic planktic bacteria. In this case, the migration of the bacteria up the chemoattractant concentration gradient is much faster than the diffusion of the chemoattractant. This is necessary for the survival of the bacteria that forage for nutrients in diffusing patches often caused by cells lysing. If the motors or cells steer or align

along chemoattractant gradients the typical nanomotor velocity might be sufficient to observe chemotaxis using this assay. In 10 seconds, H_2O_2 will diffuse approximately 140 μm . In this case, a motor would have to travel faster than 14 $\mu m/s$ up the gradient to observe appreciable chemotaxis.

Ahmed and Stocker developed a chemotactic assay based on a valved channel containing a high concentration chemoattractant reservoir at one end and an opening to a perpendicular flow channel containing extremely high concentrations of the E-coli bacteria.(Ahmed and Stocker 2008) With the valve closed, the side channel experiences no advective flow, only diffusion of the attractant into and the bacteria out of the perpendicular flow channel. While this approach can have a more steady fuel concentration gradient than the capillary assay, it still suffers from the higher dwell time effect of the single capped end. This assay is effective for chemotaxis because the accumulation can be distinguished from a chemokinetic accumulation. However, if one is interested in study the chemokinesis of an object, the single capped end and the sink/source flow end do not allow for an observed accumulation to be attributed to chemokinesis because the higher dwell times at the capped end will result in an accumulation independent of a chemokinesis.

In 2008, Palacci et al. successfully generated steady concentration gradients in a microfluidic channel structure for the purpose of studying diffusiophoresis.(Palacci et al. 2010) Palacci et al. generated the steady gradient

using a method first introduced by Diao et al. in 2006.(Diao et al. 2006) Diao et al.'s design incorporates three parallel channels in a porous membrane. The membrane allows for solution diffusion but resists pressure driven flow. By flowing an aqueous solution containing a solute species in one of the outer two channels and an aqueous solution without the solute species in the other outer channel while the solution in the center channel remains stationary, the outer two channels act as a source-sink pair. This configuration results in a steady linear gradient of solute concentration in the center channel. This approach is ideal for both chemotaxis and chemokinesis assays as it allows visualization of the objects throughout the assay, and there are no restraints on the response time of the objects relative to the diffusivity of the chemoattractants.

2.10 Chemotactic Measures

The primary measure of chemokinesis or chemotaxis used in the literature is the chemotactic index (CI). The chemotactic index is typically given as the ratio of the number chemotactic objects or cells in a region containing the maximum concentration of the chemoattractant to the number of objects or cells in a region of equal size that contains minimum (typically zero) chemoattractant concentration. The problem with this definition is that if there is a complete depletion of motors in the low concentration region, then the CI approaches infinite. Also if there is a very small number of motors in the low concentration region then the CI becomes very sensitive to motors entering and leaving the low

accumulation region, resulting a very noisy measure of chemotactic index. Alternatively, the CI has been defined as the ratio of chemoactive objects in the high concentration region divided by the normalized average number of objects. Others have observed individual cell behavior and have used more advanced calculations to determine a chemotactic sensitivity χ , a parameter that measures a populations attraction to a specific chemical intrinsically.(Ahmed and Stocker 2008) In this case, a model developed by Rivero et al. for the flux of chemotaxiing bacteria results in the following equation:

$$\chi = \frac{\tanh^{-1}\left(\frac{3\pi V_c}{8v}\right)}{\frac{\pi}{8v} \frac{K_D}{(K_D+C)^2} \frac{dC}{dx}},$$

where K_D is the dissociation constant for the bacteria receptors and the specific chemoattractant, which is previously know from reaction kinetics experiments.(Rivero et al. 1989) V_c is the net speed of the population up the gradient, v is the translational speed of the individual cells, and C is the local chemoattractant concentration. Each of these values, and the gradient in chemical concentration, are measured for several different concentrations in order to determine χ . This equation is only valid for a specific type of chemotactic behavior, particularly the klinokinesis exhibited by E-coli. The advantage is that the chemotactic sensitivity is a measure of chemotactic response to an attractant that is independent of the actual local attractant concentration gradient.

2.11 Bimetallic Nanomotors

A bimetallic nanomotor in an aqueous solution containing hydrogen peroxide results in hydrogen peroxide oxidation at the anodic end generating oxygen molecules, protons, and electrons. The electrons generated conduct through the nanomotor and combine with protons, hydrogen peroxide, and oxygen to complete the reduction reaction at the cathodic end. This process is depicted in Figure 16 for a nanorod composed of gold (cathode) and platinum (anode). The reactions result in a local excess in protons at the anodic end and a local depletion of protons at the cathodic end. The gradient in proton concentration within the surrounding electrolyte leads to an asymmetric charge density and ultimately an electric field directed from the anodic end to the cathodic end, as shown in Figure 16. The electric field coupled with the charge density produces an electrical body force driving the surrounding fluid from the anode to the cathode. In a reference frame where the fluid is stationary, this fluid motion translates to the locomotion of the nanomotor with the anode forward. The fundamental mechanism of motion resembles electrophoresis; however in this case, the electric field and the charge density distribution are generated by particle. The underlying physics of bimetallic motors has been studied extensively by Moran et al. (Moran and Posner 2011; Moran, Wheat and Posner "Locomotion of Electrocatalytic Nanomotors Due to Reaction Induced Charge Autoelectrophoresis" 2010)

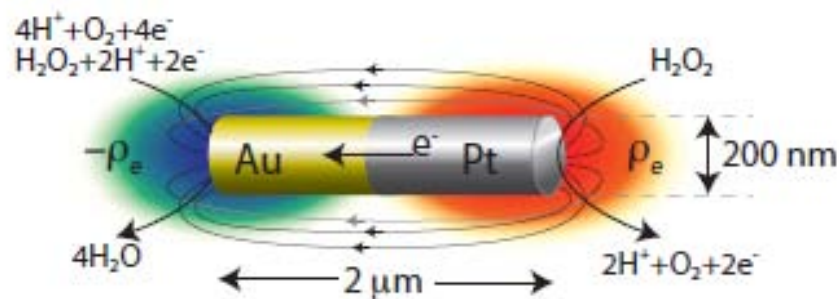


Figure 16: Schematic of a gold/platinum nanomotor of typical dimensions depicting the electrochemical reactions that occur at each end, as well as the resulting charge density and the resulting electric field lines. The red region denotes high charge density due to the local excess of protons generated at the anodic surface and the blue region denotes the low charge density due to the depletion of protons at the cathodic surface.(Moran, Wheat and Posner "Locomotion of Electrocatalytic Nanomotors Due to Reaction Induced Charge Auto-Electrophoresis" 2010) <http://pre.aps.org/abstract/PRE/v81/i6/e065302>

2.12 Bimetallic Nanomotor Efficiency

The efficiency of bimetallic motors can be calculated from the theoretical Stokes drag, the measured velocity, current density measurements, and the average Gibbs free energy of the electrochemical reactions. The efficiency η is the ratio of the mechanical power output to the chemical power input. The mechanical power output can be calculated as a product of the force exerted and the speed attained. Because the speed remains relatively constant, the nanomotor is assumed to be in equilibrium with the force exerted in equilibrium with the Stokes drag on the motor. The magnitude of Stokes drag for a cylinder can be approximated analytically by treating the cylinder as an ellipsoid, in this case the Stokes drag is given by

$$F = \frac{4\pi\mu cu}{\ln\left(\frac{2c}{b}\right) - \frac{1}{2}}$$

where μ is the viscosity, c is half the length of the cylinder, b is the radius, and u is the speed.(K. A. Rose et al. 2007) For $b = 0.11 \mu\text{m}$, $c = 1 \mu\text{m}$, $\mu = 1 \times 10^{-3} \text{ N s/m}^2$, and $u = 25 \mu\text{m/s}$ (for 6wt% H_2O_2), (Wheat et al. 2010) $F = 0.17 \text{ pN}$.

Therefore the mechanical power output is $uF = 4.25 \times 10^{-18} \text{ W}$.

The chemical power input can be calculated as product of the reaction flux j , the surface area A of the motor, and the total Gibbs free energy ΔG of the reactions.

The reaction flux is calculated from the published current density for electrochemical decomposition of 6wt% H_2O_2 at a gold platinum interface, which is $i = 0.684 \text{ C/s m}^2$.(Paxton, Kline et al. 2006) The reaction flux is given by

$$j = \frac{i}{nF},$$

where $n = 2$ is the number of electrons transferred in the reaction and $F = 96485 \text{ C/mol}$ is the Faraday constant. The surface area of a 220 nm radius, 2mm long nanomotor is $1.3823 \mu\text{m}^2$. The total Gibbs free energy for the reaction is determined using tables.(Moore 2010)The primary reactions are depicted in Figure 16. Oxidation of the H_2O_2 occurs at the platinum end resulting in the products 2H^+ , O_2 , and 2e^- . Reduction occurs at the gold end with $\text{H}_2\text{O}_2 + 2\text{H}^+ + 2\text{e}^-$ resulting in $4\text{H}_2\text{O}$. The only species involved in the reaction with non-zero standard energies of formation (ΔG_f^0) are H_2O ($\Delta G_{f,\text{H}_2\text{O}}^0 = -237.2 \text{ KJ/mol}$) and H_2O_2 ($\Delta G_{f,\text{H}_2\text{O}_2}^0 = -114.0 \text{ KJ/mol}$). (Moore 2010) Assuming reduction and

oxidation occur at the same rate, the total Gibbs free energy of the reactions is $\Delta G = -720.8 \text{ KJ/mol}$, or the energy available from the reactions is 720.8 KJ/mol .

Therefore the chemical power input is $jA\Delta G = 3.5 \times 10^{-12} \text{ W}$. Finally, the efficiency is

$$\eta = \frac{P_{mech}}{P_{chem}} = \frac{4.25 \times 10^{-18} \text{ W}}{3.5 \times 10^{-12} \text{ W}} = 1.2 \times 10^{-6}.$$

CHAPTER 3

THEORETICAL FRAMEWORK

3.1 Analytical Approach

In order to predict the ability of synthetic nanomotors to exhibit global behavior analogous to biological chemokinesis, we model chemokinesis as a purely diffusive response. To do this, it is necessary to represent a random walk behavior with an effective diffusivity. Such a representation is used by Howse et al. to model the behavior of a self-motile Janus sphere, using the following equation:

$$D_{eff} = D + \frac{1}{4} \frac{U_{adv}^2}{D_{rot}},$$

where D_{eff} is the effective diffusivity, U_{adv} is the translational velocity, D_{rot} is the rotational diffusivity, and D is the diffusivity due to Brownian motion, or the diffusivity in the absence of a chemical promoting a chemokinetic response (Howse et al. 2007). Chemokinetic responses imply that the advective velocity and/or rotational diffusivity are functions of a chemical concentration, i.e. $U_{adv} = f_1(C_{fuel/nutrients})$ for orthokinesis and/or $D_{rot} = f_2(C_{fuel/nutrients})$ for klinokinesis. From the above equation for effective diffusivity, it is expected that a chemokinetic response can be expressed in terms of the effective diffusivity as a function of chemical concentration, i.e. $D_{eff} = f(C_{fuel/nutrients})$. From there, spatial variations in concentration will translate directly to spatial variations in effective diffusivity. As a result, the flux of chemokinetic objects in a spatial gradient of fuel/nutrient concentration can be expressed using the generalization of Fick's law that deals with significant spatial variations in diffusivity for a Brownian walker.

Consider a one-dimensional Brownian walker or particle that has a direction speed component u and a turning frequency f . The rotation of the particle is random such that half way through turning around, an individual particle is equally likely to complete the direction change as it is to return to the original direction. In this case the average frequency of a direction change is $f/2$. Let R be the number density of particles moving right along the one-dimensional (x) axis, and L be the number density of particles moving left. Conservation of the particles can be written as:

$$\frac{\partial R}{\partial t} = -\frac{\partial uR}{\partial x} + \frac{f}{2}L - \frac{f}{2}R,$$

and

$$\frac{\partial L}{\partial t} = \frac{\partial uL}{\partial x} - \frac{f}{2}L + \frac{f}{2}R.$$

The total number density of particles (ρ) is $R+L$, and the particle flux (J) is $u(R-L)$. Adding the conservation equations yields:

$$\frac{\partial R}{\partial t} + \frac{\partial L}{\partial t} = -\frac{\partial uR}{\partial x} + \frac{\partial uL}{\partial x} \Rightarrow \frac{\partial(R+L)}{\partial t} = -\frac{\partial u(R-L)}{\partial x} \Rightarrow \frac{\partial \rho}{\partial t} = -\frac{\partial J}{\partial x},$$

and subtracting the two equations yields

$$\frac{\partial R}{\partial t} - \frac{\partial L}{\partial t} = -\frac{\partial uR}{\partial x} - \frac{\partial uL}{\partial x} + fL - fR \Rightarrow \frac{\partial(R-L)}{\partial t} = -\frac{\partial u(R+L)}{\partial x} - f(R-L),$$

$$\Rightarrow \frac{\partial}{\partial t} \left(\frac{J}{u} \right) = -\frac{\partial u\rho}{\partial x} - f \frac{J}{u}.$$

Multiplying by velocity and differentiating w.r.t. x yields:

$$\frac{\partial}{\partial x} \left(u \frac{\partial}{\partial t} \left(\frac{J}{u} \right) \right) = -\frac{\partial}{\partial x} \left(u \frac{\partial u\rho}{\partial x} \right) - \frac{\partial}{\partial x} (fJ).$$

Let u be a function of x and not a function of time, such that

$$\frac{\partial}{\partial x} \left(\frac{\partial}{\partial t} (J) \right) = - \frac{\partial}{\partial x} \left(u \frac{\partial u \rho}{\partial x} \right) - \frac{\partial}{\partial x} (fJ).$$

For the L.H.S, the order of differentiation is interchangeable.

$$\frac{\partial}{\partial t} \left(\frac{\partial J}{\partial x} \right) = - \frac{\partial}{\partial x} \left(u \frac{\partial u \rho}{\partial x} \right) - \frac{\partial}{\partial x} (fJ).$$

Recall,

$$\frac{\partial J}{\partial x} = - \frac{\partial \rho}{\partial t}, \text{ such that the conservation equation becomes:}$$

$$\frac{\partial^2 \rho}{\partial t^2} = + \frac{\partial}{\partial x} \left(u \frac{\partial u \rho}{\partial x} \right) + \frac{\partial}{\partial x} (fJ).$$

For diffusive processes for which short time behavior is of little interest, the second derivative in time can be considered negligible. The resulting equation,

$$\frac{\partial}{\partial x} \left(u \frac{\partial u \rho}{\partial x} \right) + \frac{\partial}{\partial x} (fJ) = 0 \Rightarrow \partial(fJ) = -\partial \left(u \frac{\partial u \rho}{\partial x} \right),$$

is integrated to yield:

$$\int \partial(fJ) = - \int \partial \left(u \frac{\partial u \rho}{\partial x} \right) \Rightarrow fJ = -u \frac{\partial u \rho}{\partial x},$$

$$\Rightarrow J = - \frac{u}{f} \frac{\partial u \rho}{\partial x}.$$

There are 5 variations of this equation worth discussing.

Case 1: u is a constant and f is a constant. In this case the flux equation becomes:

$$J = - \frac{u^2}{f} \frac{\partial \rho}{\partial x}.$$

Let u^2/f be defined as the effective diffusivity D_{eff} of the particles. Here the flux equation becomes the traditional Fick's law of diffusion:

$$J = -D_{eff} \frac{\partial \rho}{\partial x},$$

where D_{eff} is a constant.

Case 2: u is a constant and f varies in space. In this case the flux equation becomes:

$$J = -\frac{u^2}{f(x)} \frac{\partial \rho}{\partial x} = -D_{eff}(x) \frac{\partial \rho}{\partial x}.$$

In this case, the effective diffusivity varies with space, such that the flux equation is Fick's law of diffusion for variable diffusivity. It is clear that the steady state equilibrium particle distribution is a uniform distribution.

Case 3: The ratio $u(x)/f(x)$ is a constant. In this case, the flux equation can be expanded using the product rule:

$$J = -\frac{uu(x)}{f} \frac{\partial \rho}{\partial x} - \rho \frac{\partial}{\partial x} \left(\frac{uu(x)}{f} \right) = -D_{eff} \frac{\partial \rho}{\partial x} - \rho \frac{\partial D_{eff}}{\partial x} = \frac{\partial}{\partial x} (\rho D_{eff}).$$

Here the flux equation is the Fokker-Plank law of diffusive flux.

Case 4: u varies with x , while f is a constant. In this case, the flux equation can be written as:

$$J = -\frac{u^2(x)}{f} \frac{\partial \rho}{\partial x} - u(x) \rho \frac{\partial}{\partial x} \left(\frac{u(x)}{f} \right).$$

From the product rule:

$$u(x) \rho \frac{\partial}{\partial x} \left(\frac{u(x)}{f} \right) + u(x) \rho \frac{\partial}{\partial x} \left(\frac{u(x)}{f} \right) = \rho \frac{\partial}{\partial x} \left(\frac{u^2(x)}{f} \right)$$

$$\Rightarrow u(x) \rho \frac{\partial}{\partial x} \left(\frac{u(x)}{f} \right) = \frac{\rho}{2} \frac{\partial}{\partial x} (D_{eff}).$$

$$\Rightarrow J = -D_{eff} \frac{\partial \rho}{\partial x} - \frac{\rho}{2} \frac{\partial}{\partial x} (D_{eff}).$$

The previous cases are described in detail by Schnitzer. The following cases are my work.

Case 5: u and f vary independently with x . In the most general case, both speed and turning frequency will vary with position. In this case, the flux equation is:

$$J = -\frac{u^2(x)}{f(x)} \frac{\partial \rho}{\partial x} - \frac{u(x)}{f(x)} \rho \frac{\partial u(x)}{\partial x}.$$

Again from the product rule:

$$\rho \frac{\partial}{\partial x} \left(\frac{u^2}{f} \right) = \rho u^2 \frac{\partial}{\partial x} \left(\frac{1}{f} \right) + \frac{\rho}{f} \frac{\partial}{\partial x} (u^2) = \rho u^2 \frac{\partial}{\partial x} \left(\frac{1}{f} \right) + \frac{2\rho u}{f} \frac{\partial u}{\partial x},$$

such that

$$\frac{\rho u}{f} \frac{\partial u}{\partial x} = \frac{\rho}{2} \frac{\partial}{\partial x} \left(\frac{u^2}{f} \right) - \frac{\rho u^2}{2} \frac{\partial}{\partial x} \left(\frac{1}{f} \right).$$

As a result, the flux equation becomes:

$$J = -D_{eff} \frac{\partial \rho}{\partial x} - \frac{\rho}{2} \frac{\partial D_{eff}}{\partial x} + \frac{\rho u^2}{2} \frac{\partial}{\partial x} \left(\frac{1}{f} \right).$$

In this case, the flux equation does not reduce to a form of the Fokker-Planck law, and information about turning frequency is necessary to determine the flux. Note that the diffusive flux equations in cases 2, 3 and 4 can be generalized as follows:

$$J = -D_{eff} \frac{\partial \rho}{\partial x} - \alpha \rho \frac{\partial D_{eff}}{\partial x}.$$

This flux equation is referred to as the modified Fokker-Planck law of diffusive flux, where α is the Ito-Stratonovich coefficient. In cases 2, 3, and 4, $\alpha = 0, 1,$ and 0.5 respectively. For the more general case 5, the flux equation can only be reduced to this form if

$$\frac{\rho}{2} \frac{\partial D_{eff}}{\partial x} - \frac{\rho u^2}{2} \frac{\partial}{\partial x} \left(\frac{1}{f} \right) = \alpha \rho \frac{\partial D_{eff}}{\partial x},$$

which requires

$$\frac{\partial}{\partial x} \left(\frac{1}{f} \right) = - \left(\frac{2\alpha - 1}{u^2} \right) \frac{\partial D_{eff}}{\partial x}.$$

This requirement can be written in a more insightful way. Recall from the product rule expansion above,

$$\frac{\rho u^2}{2} \frac{\partial}{\partial x} \left(\frac{1}{f} \right) = \frac{\rho}{2} \frac{\partial}{\partial x} \left(\frac{u^2}{f} \right) - \frac{\rho u}{f} \frac{\partial u}{\partial x} = \frac{\rho}{2} \frac{\partial D_{eff}}{\partial x} - \frac{\rho u}{f} \frac{\partial u}{\partial x},$$

which reduces to:

$$\frac{\partial}{\partial x} \left(\frac{1}{f} \right) = \frac{1}{u^2} \frac{\partial D_{eff}}{\partial x} - \frac{2u}{u^2 f} \frac{\partial u}{\partial x}.$$

Therefore the following equation must be satisfied to reduce the flux equation to the Ito-Stratonovich convention:

$$\begin{aligned} \frac{1}{u^2} \frac{\partial D_{eff}}{\partial x} - \frac{2u}{u^2 f} \frac{\partial u}{\partial x} &= - \left(\frac{2\alpha - 1}{u^2} \right) \frac{\partial D_{eff}}{\partial x}, \\ \Rightarrow \frac{\partial D_{eff}}{\partial x} - \frac{2u}{f} \frac{\partial u}{\partial x} &= -(2\alpha - 1) \frac{\partial D_{eff}}{\partial x}, \\ \Rightarrow \frac{u}{f} \frac{\partial u}{\partial x} &= \alpha \frac{\partial D_{eff}}{\partial x}. \end{aligned}$$

Case 5a: Any value of alpha can be obtained if the above equation is true.

Solving for alpha this equation becomes:

$$\alpha = \frac{\frac{u \partial u}{f \partial x}}{\frac{\partial D_{eff}}{\partial x}}.$$

Otherwise the flux equation remains in the following general form:

$$J = -D_{eff} \frac{\partial \rho}{\partial x} - \frac{\rho}{2} \frac{\partial D_{eff}}{\partial x} + \frac{\rho u^2}{2} \frac{\partial}{\partial x} \left(\frac{1}{f} \right),$$

which requires knowledge of the turning frequency and the axial velocity to determine the flux.

Case 5b: Now consider a less general case with a constant α , and a constant $\frac{\partial u}{\partial x}$,

$$\frac{u}{f} \propto \frac{\partial D_{eff}}{\partial x}.$$

Recall that if the left hand side is a constant, then $\alpha = 1$. If the left hand side is not constant, an alternative value of α is obtained.

Case 5c: Alternatively, consider a linear gradient in D_{eff} . In this case,

$$\frac{u}{f} \frac{\partial u}{\partial x} = constant.$$

For the PDE analysis in this work, the modified Fokker-Planck law of diffusive flux is used:

$$J = -D_{eff} \frac{\partial \rho}{\partial x} - \alpha \rho \frac{\partial D_{eff}}{\partial x},$$

where the turning frequency f is analogous to a rotational diffusivity. In order to use this equation, a value must be determined for α . This value was selected by considering the underlying physics of the motors, and by comparison with the Brownian Dynamics simulations, discussed in section 3.2. In previous work, I have observed a linear relationship between nanomotor speed and fuel concentration (Figure 24).(Wheat et al. 2010) Furthermore, our research team has not yet had success in measuring a klinokinetic response for the nanomotors. Therefore I program the Brownian Dynamics simulation to account for a linear relationship between speed and fuel concentration, and no variation in rotational diffusivity. Recall from the above discussion, that this situation corresponds to case 4, where $\alpha = 0.5$. To compare the PDE model to the BD simulation, the BD

simulation was first run with a linear spatial gradient in speed (simulating a linear gradient in H_2O_2 and a linear relationship between the motor speed and the H_2O_2 concentration). The effective diffusivity of the simulated motors was calculated as a function of position; the results are shown as red circles in Figure 17. The input into the PDE model is the blue fit curve shown in Figure 17. The simulation and model results are compared in Figure 18. The red line shows the BD. The blue line shows the PDE ($\alpha=0.5$) with the gradient in diffusivity determined from the BD as shown in blue in figure 24. It is clear from Figure 18, that the PDE model under these conditions is not capturing all of the behavior in the BD simulation. Specifically there is some variation in rotational diffusivity that is imposed by the reflective wall boundary condition which results in a reduction in the effective diffusivity near $x=0$. This solution is not appropriate because when α is 0.5 then f should be constant, but we don't impose this. If we did, the effective diffusivity would appear quadratic and increase sharply at $x=0$. Alternatively, if we impose a linear gradient in effective diffusivity as the input into the PDE model, which in general allows the u and f to vary spatially arbitrarily as long it satisfies the linear diffusivity gradient, then 5c and a constant arbitrary value of α is not always applicable. To use the modified FP equation and a constant α (case 5c) then u and f must vary to satisfy $(u/f)(du/dx) = \text{constant}$. In this case, the value of α is unknown, but depends on the specific relationship between to u and f that results in the linear diffusivity gradient. In our case, we do not satisfy $(u/f)(du/dx) = \text{constant}$ and thus the FP equation is not strictly applicable, and we should include the additional term $u^2 \rho(d/df)$. To use

this additional term we need $f(x)$, which could theoretically be determined from experiments or from analysis of the BD simulations. Instead, for simplicity, we use the FP equation, a linear diffusivity gradient, and vary α until the results agree with the BD simulation results. A value of $\alpha = 2/3$ was determined to result in the best agreement, as shown by the black line in Figure 18. Throughout the remainder of this research, a linear approximation of the effective diffusivity is used with $\alpha = 2/3$ for all of the PDE models.

$$D_{eff}$$

$$(\mu_2$$

$$m$$

$$/s)$$

$$x/w$$

Figure 17: Effective diffusivity as a function of position across the width of the channel measured from a BD simulation (red circles), fit as the input for the PDE model (blue), and a linear gradient in effective diffusivity going from the maximum to the minimum values obtained in the BD simulation (black).

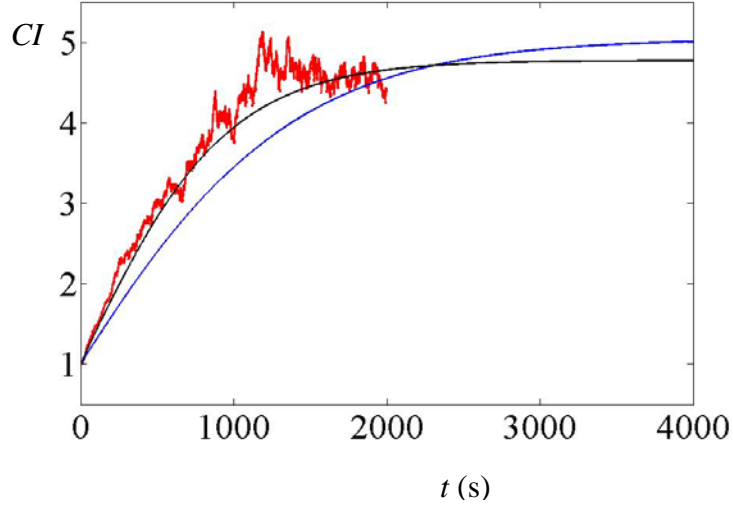


Figure 18: Chemotactic index as a function of time determined using a BD simulation with a maximum axial speed of $6 \mu\text{m/s}$ and a minimum axial speed of $0.5 \mu\text{m/s}$ (red), using the PDE model with $\alpha = 0.5$ and the effective diffusivity fit shown in Figure 17 (blue), and using the PDE with $\alpha = 2/3$ and the black linear approximation of D_{ef} shown in Figure 17 (black).

To complete the governing equation for concentration as a function of time and space, according to Fick's second law, the time rate of change of the concentration is equal to the spatial gradient in flux. In this case, in the absence of advection,

$$\frac{\partial \rho}{\partial t} = \nabla \cdot (D \nabla \rho + \alpha \rho \nabla D).$$

Expanding and applying the product rule,

$$\frac{\partial \rho}{\partial t} = +D \nabla^2 \rho + (1 + \alpha) \nabla D \cdot \nabla \rho + \alpha \rho \nabla^2 D.$$

I use this equation for modeling the chemokinetic response of nanomotors that lack a directional sensing component. This requires knowledge of the kinetic response of the nanomotors as a function of chemoattractant concentration, which is easily obtained experimentally, and knowledge of the concentration as a

function of position. Furthermore, this is valid for biological or synthetic nanomotors that undergo pure chemokinesis (under the conditions prescribed above, where the modified Fokker-Plank law of diffusive flux is valid).

To solve this equation I use a 2nd order center difference method in space and a first order backward Euler method in time. This method is inherently stable and does not require any CFL type step size condition to be met. This approach requires both an initial condition and boundary conditions. The equation is solved in 1D because the chemical concentration gradient exists only in 1 dimension (x) in the experiments (across the width of the channel). For the initial condition I use a uniform distribution of the nanomotors across the width of the channel. For the boundary conditions I establish a no flux condition. Recall the modified Fokker-

Planck law of diffusive flux: $J = -D_{eff} \frac{\partial \rho}{\partial x} - \alpha \rho \frac{\partial D_{eff}}{\partial x}$.

Enforcing the no flux boundary condition requires:

$$D_{eff} \frac{\partial \rho}{\partial x} = -\alpha \rho \frac{\partial D_{eff}}{\partial x}.$$

In 1D, the governing equation becomes:

$$\frac{\partial \rho}{\partial t} = +D \frac{\partial^2 \rho}{\partial x^2} + (1 + \alpha) \frac{\partial D}{\partial x} \cdot \frac{\partial \rho}{\partial x} + \alpha \rho \frac{\partial^2 D}{\partial x^2}.$$

The experiments used in this research involve static chemical concentration gradients. As a result, the effective diffusivity of the motors, which is dependent on the local chemical concentration gradient, does not vary with time. Therefore, the values of the 1st and 2nd spatial derivatives of the effective diffusivity at each position can be determined from the values of the effective diffusivity at each location. The effective diffusivity as a function of position across the channel

width is provided as an input in the code and for comparisons it is obtained from the experiments. To make clear the constant nature of the effective diffusivities with respect to time, I rewrite the governing equation as follows:

$$\frac{\partial \rho}{\partial t} = +D \frac{\partial^2 \rho}{\partial x^2} + (1 + \alpha) D_x \cdot \frac{\partial \rho}{\partial x} + \alpha D_{xx} \rho.$$

The discretized form of this equation, using the methods prescribed above is:

$$\frac{\rho_{i,j} - \rho_{i,j-1}}{\Delta t} = +D_i \frac{\rho_{i+1,j} - 2\rho_{i,j} + \rho_{i-1,j}}{\Delta x^2} + (1 + \alpha) D_{x,i} \cdot \frac{\rho_{i+1,j} - \rho_{i-1,j}}{2\Delta x} + \alpha D_{xx,i} \rho_{i,j}.$$

Where D_i is an input into the code, D_{xi} and D_{xxi} are determined at the beginning of the code using 2nd order center difference methods and the input D_i .

$$D_{xi} = \frac{D_{i+1} - D_{i-1}}{2\Delta x},$$

and

$$D_{xxi} = \frac{D_{i+1} - 2D_i + D_{i-1}}{\Delta x^2}.$$

At the boundaries, the $D_{x,1} = D_{x,2}$, $D_{x,N} = D_{x,N-1}$, and $D_{xx,1} = D_{xx,2}$, $D_{xx,N} = D_{xx,N-1}$.

At each time step, the number density ρ is determined using the above discretization and the Thomas algorithm.

3.2 Computational Approach

I wrote a Brownian dynamics code to simulate the behavior of the nanomotors with varying chemokinetic responses subjected to various fuel concentration gradients. The code is based on a standard Langevin model that neglects inertial effects (justified by the extremely low Reynolds number associated with the motion of nano and micromotors) reducing to the Einstein diffusion equation with

a deterministic axial velocity as follows:

$$\Delta x = \dot{x}\Delta t + S_x, \text{ and}$$

$$\Delta\theta = S_\theta.$$

where \dot{x} is a superimposed deterministic axial velocity that represents the motor axial velocity, and S is a stochastic displacement term coded to have the following characteristics to represent thermal motion consistent with theoretical Stokes-Einstein diffusion:

$$\langle S_x \rangle = \langle S_\theta \rangle = 0,$$

$$\langle S_x^2 \rangle = 2D\Delta t, \text{ and}$$

$$\langle S_\theta^2 \rangle = 2D_{rot}\Delta t.$$

The code was written in Matlab. The code incorporates several options, as shown in Table A.1, that determine the general nature of the simulation, such as whether or not the simulation space is bound by walls, or whether or not the fuel concentration is actively diffusing or if it is stationary. There is also a set of parameters, listed in Table A.2, that determine size and number of nanomotors being simulated, the duration of the simulation, and the diffusivity of the fuel. The code tracks each nanomotor individually. At each time step, for each nanomotor, a translational velocity and rotational diffusivity are determined by the fuel concentration at the location of the nanomotors based on the input relationships (with a random component built in for Brownian motion). A rotational velocity is assigned that corresponds to the rotational diffusivity for that concentration. The velocities are multiplied by the time to determine the next location and orientation of each of the nanomotors. I typically simulate 10 000 motors for 2 000 s with

$\Delta t=0.1$ s. The time step was selected to maintain physical consistency and allow for long simulation times. The simulation results were self-consistent for time steps up 0.1 s, above 0.1 s the results were no longer consistent with the results obtained by the same code with a shorter time step. The simulations incorporate an enclosed region for comparison with experiments. The region is a rectangle; the size of the rectangle corresponds to the field of view in the experiments. The boundaries are reflective in both position and orientation, such that the each behave like a mirror. Appendix B contains a section that describes the code in detail. The code used is also shown in Appendix B.

CHAPTER 4

EXPERIMENTAL METHODS

In order to observe the global behavior of bimetallic motors, I have developed a novel synthetic nanomotor fabrication technique, I have fabricated two different types of nanomotors, each with varying dimensions and metallic compositions, and I have experimentally characterized kinetic responses to hydrogen peroxide concentration. The first type of nanomotor I worked with is the bimetallic rod that has been utilized for a vast majority of the synthetic nanomotor work done to date. For these I used the same fabrication technique found in the literature.(Paxton et al. 2004) I varied both the overall length of the nanorods as well as the lengths of the segments. I have also varied the composition of the segments using several combinations of gold, platinum, and nickel. The second type of nanomotor I worked with is a spherical bimetallic nanomotor. In order to perform experiments with larger bimetallic motors without concern for the motors settling and adsorbing to the surface, I developed a new technique for fabricating spherical bimetallic motors that have a lower density. I varied the diameter of the spherical motors, and I used nickel, gold, palladium, and platinum for the segment compositions.

4.1 Fabrication of Rod-Shaped Nanomotors

The rod-shaped nanomotors are fabricated using an electrodeposition based template synthesis technique that requires a three electrode potentiostat, cyanide-based chemistry, and porous membranes. The porous membranes are placed on

top of a metal working electrode such that the opening of the pores on one side are flush against the metal surface. A plating solution containing dissolved metal salts, such that the metals are in the form of cations, is contained above the membrane. The plating solution permeates the pores of the membrane and is in contact with the working electrode. The solution above the membrane also contains a reference electrode and a counter electrode. The three electrode potentiostat (Princeton Applied Research, Versastat4; Oak Ridge, TN) varies the current between the counter electrode and the working electrode to establish the desired applied potential difference between the working electrode and the reference electrode. Negative applied potentials cause the cations to electromigrate towards the working electrode where they gain an electron upon contact with the electrode surface and reduce to form a solid metal. Over time, the metal accumulates within the pores. The plating solution is replaced by a plating solution for another metal to form the bimetallic rods. Once the rods are complete, the disk is removed from the working electrode and dissolved yielding only the solid, bimetallic cylinders that had filled the membrane pores. This process is depicted in Figure 19.

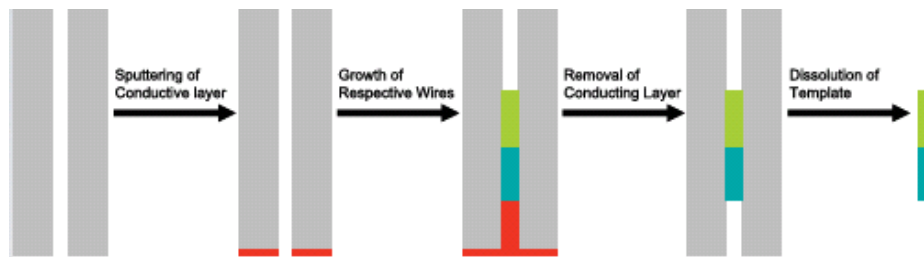


Figure 19: Bimetallic nanorod fabrication process.

The porous membranes are commercially available alumina anodiscs that are 60 μm thick with a diameter of 25mm and a pore diameter of 220 nm (Whatman, Cat. No. 6809-6022; Maidstone, UK). On one side of the membrane, the anodiscs have a polycarbonate ring fused to the outer edge. First, I coat the side of the anodisc with the polycarbonate ring with 200 nm of gold using a sputter coater (Cressington 108 auto, Cressington Scientific Instruments, Watford WD19 4BX, England, UK). The anodisc is then placed in an electrochemical cell as shown in Figure 20 with the gold coated side facedown to make electrical contact with a sheet of copper. The copper sheet is lying on an anodized aluminum block and protrudes laterally beyond the dimensions of the electrochemical cell on one side to provide a connection point for the working electrode lead of the three electrode potentiostat. A hollowed out 75 mm long Teflon cylinder with an inner diameter of 20 mm is then placed on top of the anodisc and screwed tightly to the aluminum support block. To reduce the likelihood of membrane cracking, the membranes are wetted with 18 M Ω resistance de-ionized (DI) water (Millipore, Milli-Q, Billerica, MA) prior to assembling the cell. Next, the plating solution is poured into the Teflon cylinder. Then a piece of 100 μm diameter platinum wire is wrapped around a silver/silver chloride (Ag/AgCl) reference electrode (BASi, MF-2052 RE-5B, West Lafayette, IN) and both are inserted into the solution without making contact with the anodisc. The platinum wire and the reference electrode are connected to the counter and reference electrode leads of the potentiostat respectively to complete the electrochemical cell.

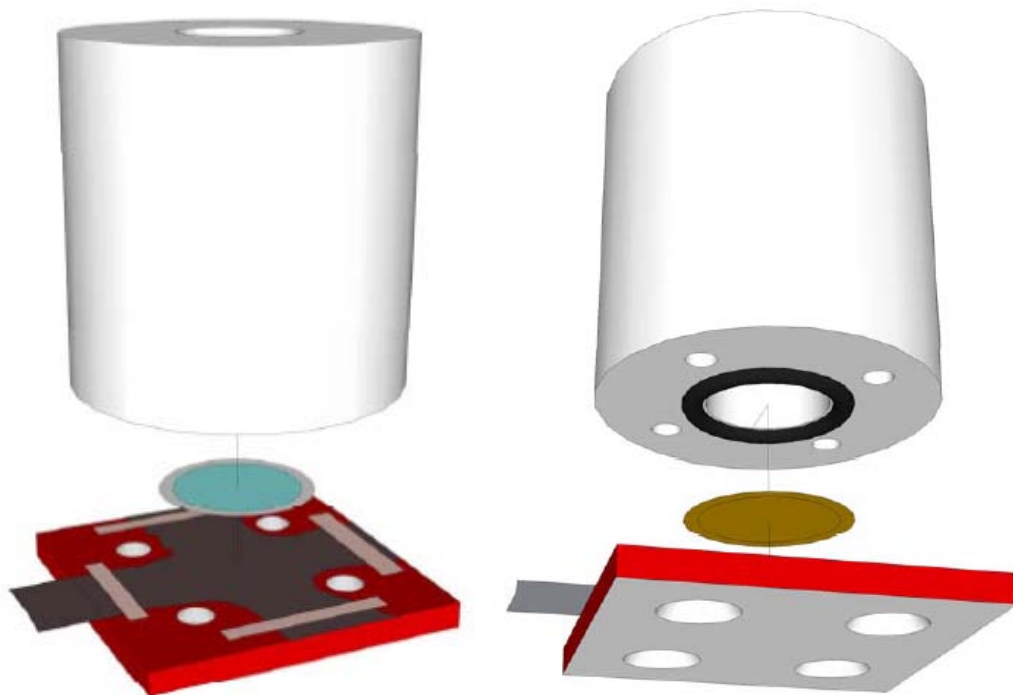


Figure 20: Exploded view of the electrochemical cell used to fabricate bimetallic nanorods.

The manufacturing process of the anodiscs results in regular pores of with high uniformity in diameter and shape, except within one micron of the side on which the polycarbonate ring is fused where the pores are highly irregular. To prevent these irregularities in pore shape from translating to irregularities in the shape of the nanomotors, a sacrificial layer of silver is the first metal to be plated. Silver plating solution (1025 RTU@4.5 Troy/Gallon; Technic Inc., Anaheim, CA) is poured into the electrochemical cell at stock concentration until the cell is nearly full (fill such that the reference electrode, when placed, does not cause the solution to overflow onto the top of the cell), and -0.9 V is applied until 3 C is plated. The silver plating solution is then poured out of the cell and back into the

container with the stock silver plating solution for reuse. The cell is rinsed three times with DI water and then the gold plating solution (Orotemp 24 RTU RACK; Technic Inc., Anaheim, CA) is added at stock concentration until the cell is nearly full. Apply -0.9 V to plate 1.5 C of gold. Again, the plating solution is poured back into the stock solution for reuse, and the cell is rinsed three times. Finally, the platinum plating solution (Platinum RTP; Technic Inc., Anaheim, CA) is added at stock concentration, in this case a current of -2 mA is applied for 50 minutes. This results in the typical gold platinum nanomotor used in most of our experiments. In some cases I added a nickel segment to allow for magnetic manipulation of the nanomotors. In these cases, the nickel segment is placed between two gold segments, because the nickel does not form as strong of a connection with the platinum and usually results in the nanomotors breaking at the nickel platinum interface. I applied -1.0 V to plate 2 C of nickel to result in a nickel segment approximately 0.5 μm long. The nickel plating solution is composed of 20g/L $\text{NiCl}_2(6\text{H}_2\text{O})$ with 515 g/L $\text{Ni}(\text{H}_2\text{NSO}_3)_2(4\text{H}_2\text{O})$.

After completing the plating processes, the electrochemical cell is disassembled. First, the gold coating is removed by carefully polishing the membrane with cotton q-tips and aluminum oxide (Inframat Advanced Materials, 26R-0803UP, Farmington, CT). (NOTE: to avoid cracking the membrane, keep it wet while transporting. Dip a clean q-tip into the AlO_2 powder to cover the cotton end liberally. Be extremely careful while polishing, because the q-tip will soak up the water and dry the membrane. Drying the membrane is fine at this point, just

polish lightly in small circles. Do not allow wrinkles to form in the membrane, and if they do, rewet the membrane.) Second, the silver sacrificial layer is removed using 500 μ L of 30% nitric acid (6901-05, J.T. Baker, Phillipsburg, NJ) and gently polishing with cotton q-tips. Third, the membrane is broken out of the polycarbonate ring and the pieces are placed in a 1.5 mL centrifuge tube (Fisher Scientific, 05-408-129, Pittsburgh, PA) and mixed with 3 mM NaOH (Mallinckrodt Baker, 7708-06, Phillipsburg, NJ) for 30 minutes, dissolving the membrane. Finally, the solution is sonicated for 1 minute (Branson Ultrasonic Corporation, 2510, Danbury, CT) and then centrifuge at 200 g for 2 minutes (Eppendorf, 5415D, Hamburg, Germany), and the supernatant is replaced with 18 M Ω DI water. This rinse step is repeated 10 times, such that the remaining solution consists only of DI water and nanorods. For a majority of the chemokinesis assays, the gold platinum nanorods were made shorter using -0.9 V to plate 1.125 C of gold and -2 mA for 37.5 minutes when plating the platinum. The shorter nanorods were used to reduce gravitational settling.

4.2 Fabrication of Spherical Motors

This section is reproduced in part with permission from [Wheat, P. M., Marine, N. A., Moran, J. L. & Posner, J. D. Rapid Fabrication of Bimetallic Spherical Motors. *Langmuir* 26, 13052-13055.] Copyright [2010] American Chemical Society. I have introduced a facile method for fabricating bimetallic motors. These motors can be produced with a wide range of core materials, including

those with relatively low density. The buoyancy of the particles could be made more neutral or positive by adding solute to the hydrogen peroxide solutions; however, some solute molecules could interfere with the surface reactions or alter the properties of the electric double layer, which plays an important role in the particle locomotion. The spherical nanomotors have velocities comparable to cylindrical ones with equivalent half-lengths. Low density motors have lower settling velocities enabling studies over a larger range of motors sizes. I observe a linear increase in motor velocity with concentration, consistent with previous work. The nanomotor velocity decreases with the sphere radius.

The spherical bimetallic motors are fabricated by sputter coating the entire surface of spherical particles with one metal and then half-coating the metal coated sphere with a second metal. In this work, I use fluorescent polystyrene spheres ($\rho = 1.05 \text{ g/cm}^3$, Duke Scientific Inc., Fremont, CA, USA). The particle fluorescence aids in the interpretation of the coating process. I choose polystyrene spheres because it yields motors with small density differences from the bulk solution and minimizes settling velocities. I use gold and platinum metals so that our results can be compared to the Au-Pt cylindrical nanomotors results (Paxton, Sen and Mallouk 2005; Laocharoensuk, Burdick and Wang 2008) but the same process can be used with nearly any metal that can be deposited on spheres.

First, a 1% volume fraction aqueous dispersion of spheres is deposited onto a $2.5 \times 2.5 \text{ cm}^2$ square glass substrate. The solvent evaporates at room temperature,

forming a monolayer of spheres. The upper hemispheres are coated with 20 nm of gold using a sputter coater (Cressington 108 auto, Cressington Scientific Instruments, Watford WD19 4BX, England, UK). The sputter coater only coats the upper hemisphere due to the directionality of the sputter coater.(Takei and Shimizu 1997; Tien and Cunningt.Gr 1972; Paunov and Cayre 2004) The half-coated spheres are resuspended in an aqueous solution and then deposited into a monolayer on a clean glass slide. The second deposition results in a monolayer of spheres that have random orientations relative to their coated hemispheres. Each time the spheres are redeposited, they are randomly oriented allowing for previously unexposed portions of the spheres to be coated. This process is illustrated in Figure 21a-c. I repeat this process 7 or 8 times to ensure the entire surface is coated with the first metal. I inspect the coating of the spheres after each deposition with epifluorescence microscopy using an inverted microscope (Nikon TE2000, Japan), a 40x objective with a 1.5x multiplier, NA = 0.6, and metal halide illumination (EXFO X-Cite 120, Ontario, Canada). The fluorescence micrographs are shown in Figure 21e-h. I consider the spheres fully coated once I no longer observe any fluorescence from the spheres. The fully Au coated spheres are redeposited on a clean substrate and finally coated with 20 nm platinum resulting in a Janus sphere that is half coated with gold and half platinum as shown in Figure 21d. The completed Janus spheres are then re-suspended and are ready for use as spherical nanomotors. This method can be used with any material that can be sputtered or evaporated onto spheres.

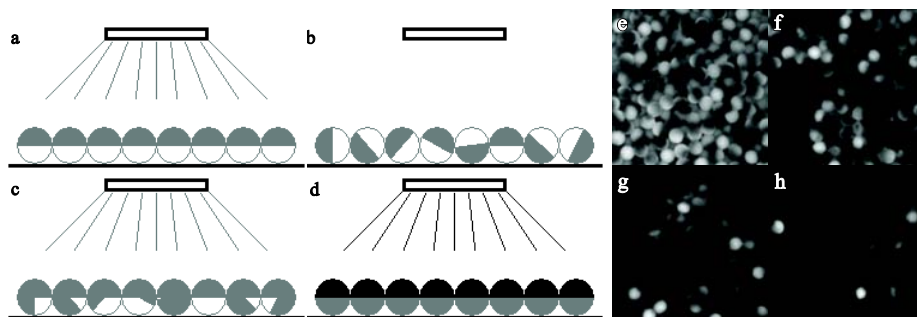


Figure 21: Schematic of the fabrication method. Fluorescent polystyrene microspheres are deposited on a glass substrate and then (a) half-coated with one metal. The spheres are then re-suspended in water and then (b) deposited again with random orientation. (c) The exposed upper-surfaces coated again. This process is repeated until the sphere is completely coated with the first metal, and then the spheres are half-coated with a second metal. The fluorescent micrographs show the progressive coverage of 5 μm fluorescent spheres after (e) 1, (f) 2, (g) 3, and (h) 4 cycles.

I use scanning electron microscopy (SEM) (NOVA 200 Nanolab, FEI Hillsboro, OR, USA) and energy-dispersive x-ray spectroscopy (EDS) (NSS212E, Thermo Fisher Scientific Inc., Waltham, MA, USA) to respectively image the shape and compositions of 5 micron Au/Ni spheres. The SEM and EDS images are shown in Figure 22a and b. Here, I use nickel in place of the platinum because it provides more highly resolved compositional analysis using EDS. In this case, the nickel is first evaporated onto the deposited spheres (Cressington 308R Evaporator, Cressington Scientific Instruments, England, UK). The SEM image in Figure 22a shows a smooth, upper nickel surface and a lower, rough gold surface. Analysis of several spheres shows that they are nearly spherical (with some small defects) and have a hemi-spherical coating of the second metal.

Transmission optical microscopy is used to observe the swimming nanomotors. I use an inverted microscope (Nikon TE2000, Japan) with a 40x objective (NA = 0.6) and 100 W halogen illumination (Nikon TE2 PS 100W, Japan). The images were captured using a CCD camera (Coolsnap HQ, Photometrics, Tucson, AZ, USA). Experiments were performed in chambered glass wells with an area of 0.8 cm^2 (Cat. No. 12-565-18, Thermo Fisher Scientific Inc., Waltham, MA, USA). During the experiments the chambers are sealed to prevent evaporation-induced convection. Each particle was tracked for 100 frames and the time averaged velocity was calculated from the sphere path. The sphere centers were calculated in MATLAB from the intensity weighted centers of the spheres in each frame. Particle centers at each time were paired using an optical flow algorithm.

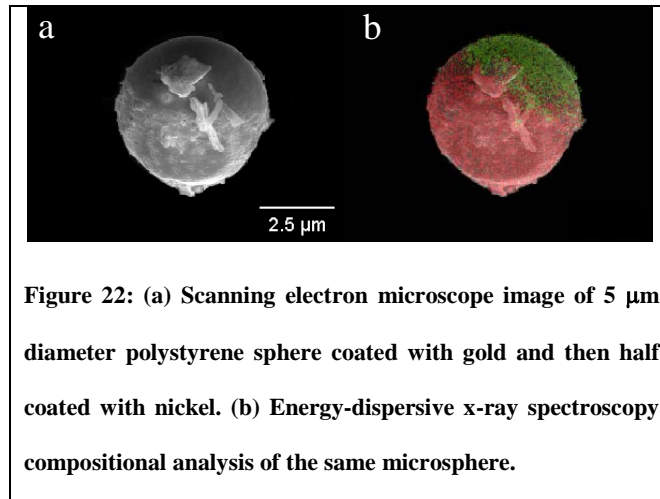


Figure 23 depicts the paths of a representative $3 \mu\text{m}$ -diameter nanomotor at hydrogen peroxide concentrations of 1%, 2%, 3%, and 4%. Each path represents an elapsed time of 11.7 seconds. These nanomotors clearly exhibit an advective velocity in excess of the migration that would be observed for a Brownian sphere.

As I increase the peroxide concentration (from a to d) the path length increases (over a fixed time) suggesting an increase in swimming velocity. In Figure 24 I show measurements of the motor swimming velocity as a function of H₂O₂ concentration for spheres of 2, 3, and 5 micron diameters. The velocities achieved by the spherical nanomotors are comparable to previously published results for rod-shaped Au/Pt nanomotors in H₂O₂. Typical maximum speeds for rod-shaped Au/Pt nanomotors 2 μm long and 220 nm in diameter have been reported between 7 and 8 μm/s. (Laoharoensuk, Burdick and Wang 2008; Paxton et al. 2004) Figure 24 shows velocities of about 15 μm/s attained by the 2 μm spheres.

Figure 23 shows that the spherical motors exhibit directed motion is relatively straight. The rotational diffusivities of spheres are less than rods with equivalent lengths. The rotational diffusivity of a rod (approximated as a spheroidal particle) is given by

$$D_{\theta,rod} = \frac{3kT}{8\pi\eta a^3} [\ln(2a/b) - 1/2],$$

where a and b are the half-length and radius of the rod, respectively. (Klint A. Rose et al. 2007); (Doi and Edwards 1988) The diffusivity of a sphere of radius a is

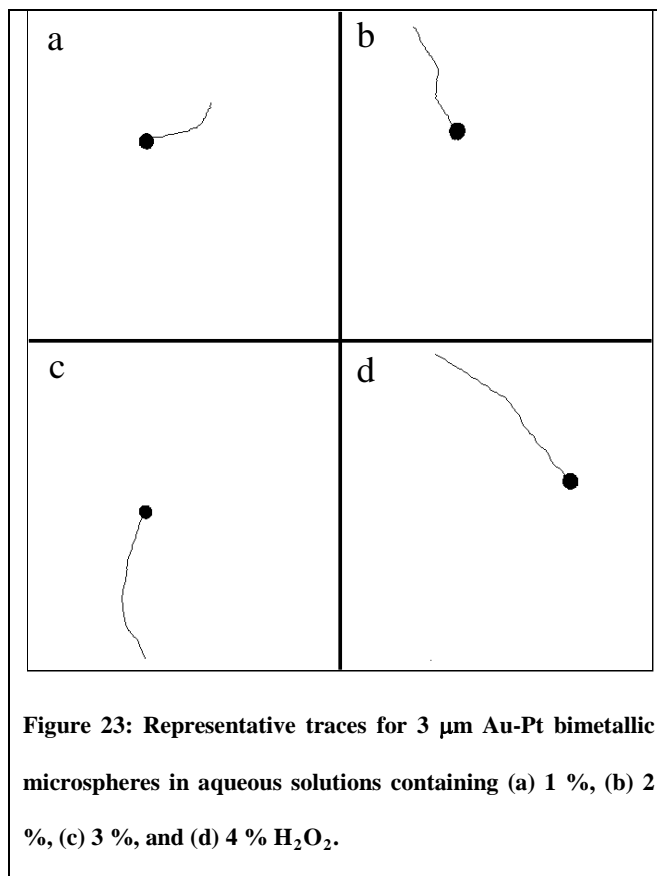
$$D_{\theta,sphere} = \frac{kT}{8\pi\eta a^3}. \quad (\text{Sourjik and Berg 2002})$$

Evaluating these for a rod with radius $b = 150$ nm and half-length $a = 1$ μm

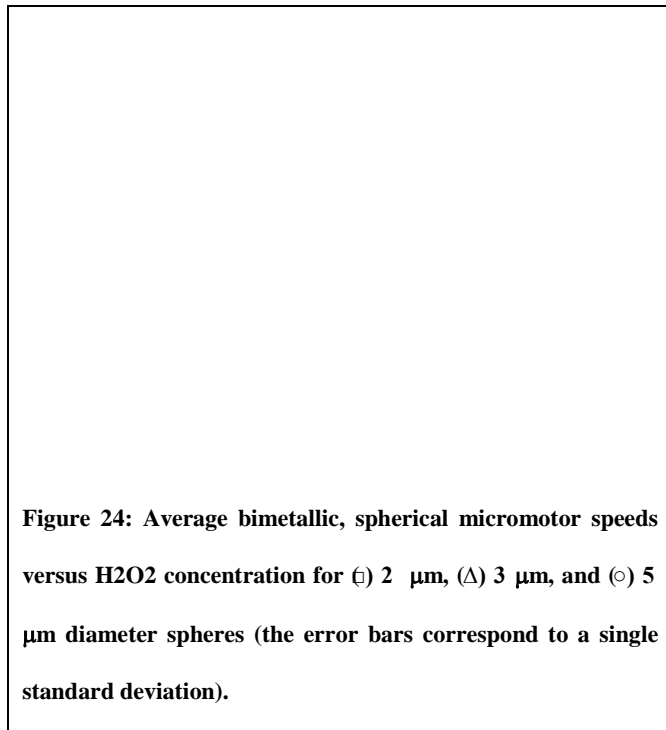
(typical dimensions for a bimetallic nanorod motor), I obtain $D_{\theta,rod} = 1.0271$ rad²/s while for a sphere with radius $a = 1 \mu\text{m}$ (the smallest sphere radius in this work), I obtain $D_{\theta,sphere} = 0.1638$ rad²/s, an order of magnitude less. The rotational diffusivity decreases further for larger spheres due to the inverse proportionality between diffusivity and radius cubed, so it is still smaller than that of the bimetallic rods. In general, as confirmed by a parametric study of rotational diffusivity as a function of both a and b for rods or spheres performed by us, the rotational diffusivity of a sphere is always less than that of a rod if the diameter of the sphere is equal to the length of the rod. Therefore, I should expect the spheres to perform more directed motion than the rods.

As predicted using a simple scaling analysis (Moran, Wheat and Posner "Locomotion of Electrocatalytic Nanomotors Due to Reaction Induced Charge Auto-Electrophoresis" 2010; Prevo and Veleev 2004) and demonstrated experimentally, (Ibele, Mallouk and Sen 2009; Laocharoensuk, Burdick and Wang 2008) there is a linear relationship between velocity and H₂O₂ concentration. The slope of this relationship can be described by an effective mobility of the motors, given as the ratio of a motor's velocity to the concentration of peroxide in which it is immersed. Defined in this way, the mobility is approximately constant for a given sphere diameter and exhibits a roughly linear decrease with increasing diameter. The Butler-Volmer equation, which governs the reaction flux at the catalyst surface, predicts that the flux for both the rods and spheres should be

equivalent when used in the same solution. From our simple scaling analysis I expect an increase in the characteristic velocity with length at fixed hydrogen peroxide concentrations.(Moran, Wheat and Posner "Locomotion of Electrocatalytic Nanomotors Due to Reaction Induced Charge Auto-Electrophoresis" 2010) This can be inferred from quadratic dependence of surface area and linear dependence of the Stokes drag on particle size. I see the converse experimental result suggesting that the viscous interactions with the solid substrate they swim along may be important.



This fabrication technique may be improved by using a more uniform particle monolayer. This would reduce the number of coating steps and prevent poor half coatings of the second metal by reduction in the number of occluded spheres by neighboring spheres. For example, a flow coating deposition process could be used to deposit the monolayers before each coating step.(Prevo and Velev 2004) Spin coating has also been used extensively to produce highly regular colloidal monolayers,(Jiang and McFarland 2004) however, a considerable fraction of the spheres may be lost on each pass of this process.



4.3 Synthetic Chemokinesis Assays

It is extremely difficult to experimentally establish a static gradient without moving fluid in chemoattractant concentration for the purpose of studying chemokinesis or chemotaxis. Such a gradient may occur in biological systems as a result of either the development of a combination of effective sources and sinks such as the site of a wound and nearby blood stream, adsorbed cells in the presence of spatially steady gradients within a flow generated by chemoattractants diffusing into the blood stream effectively creating a flow cell type situation, (Lin and Butcher 2006) or through surface adsorption of chemoattractants that prevent further diffusion. (Wilkinson 1998) For the bimetallic motors, a source and sink type scenario could conceivably be developed by interfacing a reservoir

containing hydrogen peroxide to a microfluidic channel system containing no hydrogen-peroxide. In the absence of a pressure gradient, the hydrogen peroxide would diffuse into the channels with the reservoir acting as a source. A sink could be effectively developed by focused ultraviolet photo-decomposition of the hydrogen peroxide in another region of the channel structure. Unfortunately, even with incredibly high intensities of uv-light, the uv-decomposition is very slow compared to the diffusion of hydrogen peroxide such that the resulting hydrogen peroxide concentration quickly becomes uniform everywhere, and uniformly decreases in concentration as the hydrogen-peroxide is decomposed (this is analogous to a lumped system analysis in heat transfer, where the internal heat conduction is very fast compared to the heat transfer at the surface, or at an isolated region within the body, resulting in a very low Biot number).

Alternatively, there are other chemicals that have been shown to initiate a chemokinetic response in bimetallic motors that are self-propelled in the presence of hydrogen-peroxide fuel. For example, bimetallic nanomotors that are propelled by the autocatalytic decomposition of hydrogen-peroxide have been shown to speed up significantly when either 0.15 wt % hydrazine or 100 μM silver-nitrate (AgNO_3) are added to the aqueous hydrogen-peroxide solution.(Laocharoensuk, Burdick and Wang 2008; Kagan et al. 2009) Furthermore, speeds have been shown to decrease with an increase in the solution conductivity brought about by the addition of various different salts.(Paxton, Baker et al. 2006)

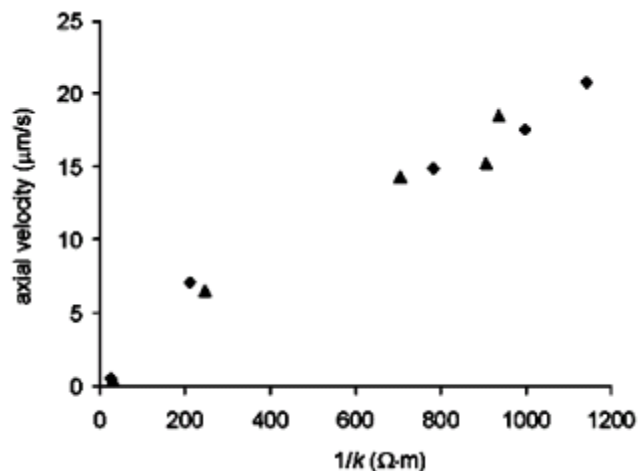


Figure 25: Nanomotor speed as a function of the electrical resistance of the solution published by Paxton et al. for two different salts: NaNO₃ (diamonds) and LiNO₃ (triangles). Adapted with permission from Paxton, W. F., et al. "Catalytically Induced Electrokinetics for Motors and Micropumps." *Journal of the American Chemical Society* 128.46 : 14881-88. Copyright 2006 American Chemical Society. <http://dx.doi.org/10.1021/ja0643164>

Alternatively, the saturated oxygen level has been shown to affect the speed of bimetallic motors in aqueous hydrogen-peroxide solutions.(Calvo-Marzal et al. 2009) In 2009, Calvo-Marzal et al. demonstrated a peak velocity associated with reduction of dissolved oxygen at -0.4 V (vs. Ag/AgCl in 100 MM KCl), with the speed decreasing to a minimum with an increase in potential up to 1.0 V (vs. Ag/AgCl).

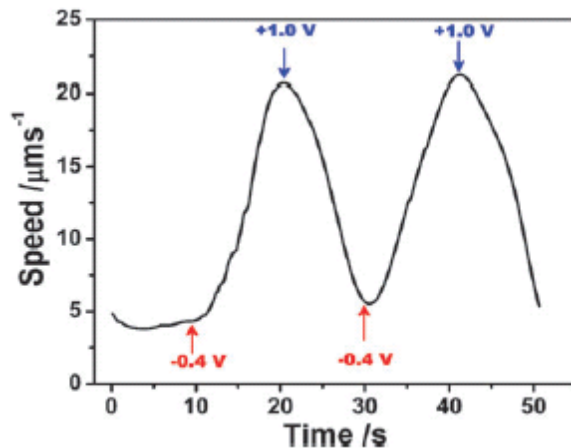


Figure 26: Electrochemical modulation of bimetallic nanomotor speed. *Calvo-Marzal, P., et al. "Electrochemically-Triggered Motion of Catalytic Nanomotors." Chemical Communications,30 (2009): 4509-11. – Reproduced by permission of The Royal Society of Chemistry*

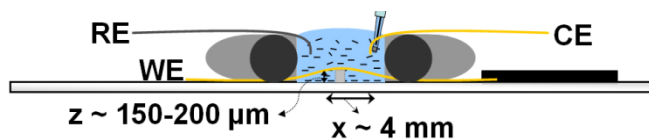


Figure 27: Experimental apparatus used by Calvo-Marzal et al. to electrochemically modulate the speed of bimetallic nanomotors. *Calvo-Marzal, P., et al. "Electrochemically-Triggered Motion of Catalytic Nanomotors." Chemical Communications,30 (2009): 4509-11. – Reproduced by permission of The Royal Society of Chemistry*

In this case, the dissolved oxygen concentration determines the orthokinetic response of the bimetallic motors. Based on these results, I attempted to develop an experimental apparatus designed to evaluate the global response of the

bimetallic motors to a steady gradient in the dissolved oxygen concentration. The apparatus is composed of interdigitated electrodes (see Figure 28) that will alternatively oxidize and reduce dissolved oxygen resulting in localized orthokinetic peaks and valleys. The electrodes are elevated by perpendicularly running capillaries suspending the wires approximately 100 μm above the glass slide substrate on which the motors will be travelling. The elevated electrodes prevent trapping or blocking resulting in artificially high dwell times. This approach requires ions from the solution to shield the electrodes such that there is no potential gradient in the fluid between the electrodes. Such a potential gradient would result in electrophoresis. Complete electrode shielding is possible if the potentials are relatively low and the electrodes are relatively far apart. Unfortunately the electrodes must be brought close together in order observe chemokinesis experimentally on a reasonable time scale. Consequentially the approach had to be abandoned as any chemokinesis that may have occurred was dominated by electrophoresis.

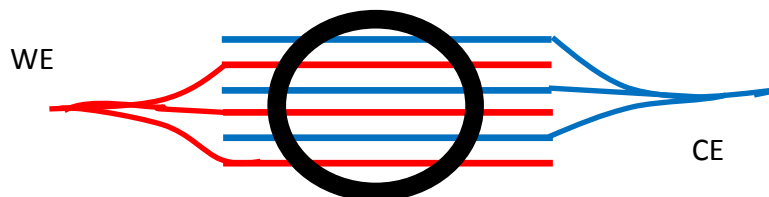


Figure 28: Interdigitated working and counter electrode modification of the design used by Calvo-Marzal. This apparatus will be used to spatially vary the speed of bimetallic motors.

In 2008, Palacci et al. successfully generated steady concentration gradients in a microfluidic channel structure, for the purpose of studying diffusiophoresis.(Palacci et al. 2010) Palacci et al. generated the steady gradient using a method first introduced by Diao et al. in 2006.(Diao et al. 2006) Diao et al.'s design incorporates three parallel channels in a porous membrane. The membrane allows for solution diffusion but resists pressure driven flow. By flowing an aqueous solution containing a solute species in one of the outer two channels and an aqueous solution without the solute species in the other outer channel while the solution in the center channel remains stationary, the outer two channels act as a source-sink pair. This configuration results in a steady linear gradient of solute concentration in the center channel. This is the approach that is used to generate a steady chemical concentration gradient for the chemokinesis assays in this work.

4.4 Experimental Apparatus

4.4.1 Overview

For the purpose of studying the synthetic chemokinesis of bimetallic nanomotors I fabricated a steady-linear-concentration gradient generator of the design first introduced by Diao et al. in 2006.(Palacci et al. 2010; Haessler et al. 2009) Figure 30 shows a schematic of the structure used. The red in the left channel depicts an aqueous solution containing H_2O_2 and the yellow in the right channel depicts an aqueous salt solution. A dual syringe pump is used to flow the solutions through the left and right channels. The H_2O_2 solution is advected into the left channel then diffuses from left to right through the nitrocellulose membrane wall into the center channel and then across the center channel, through the right wall and into the right channel where the flow advects it away. The salt solution follows a similar path in the opposite direction. The result is a linearly decreasing concentration of H_2O_2 from left to right in the center channel and a linearly increasing concentration of salt from left to right. The change in concentration across the center channel is a very small fraction of the total change in concentration from the left channel to the right channel; this is discussed in detail in section 4.4.3. In short, a large portion of the gradient develops in the porous membrane such that the gradient across center channel is $1/11^{\text{th}}$ the total change in concentration.

Figure 29 depicts the normalized H_2O_2 concentration as a function of position in

the center channel. The yellow line is experimentally obtained and corresponds to fluorescence intensity of a fluorescein salt concentration measured in the center channel. For the chemokinesis assays, nanomotors are dispersed throughout the center channel where the chemical concentration gradients correspond to a spatial gradient in nanomotor speed decreasing from left to right. The concentrations are normalized as $C^* = (C - C_{min}) / (C_{max} - C_{min})$, where C_{max} is the highest concentration within the center channel, C_{min} is the lowest concentration across the center channel, and C is the concentration as a function of position across the channel.

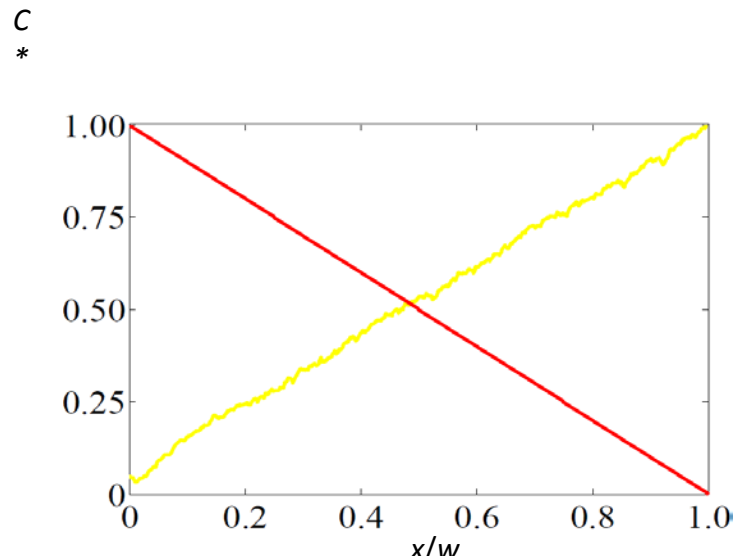


Figure 29: Concentration profiles of salt (experimental) and H_2O_2 (predicted) in the center channel.

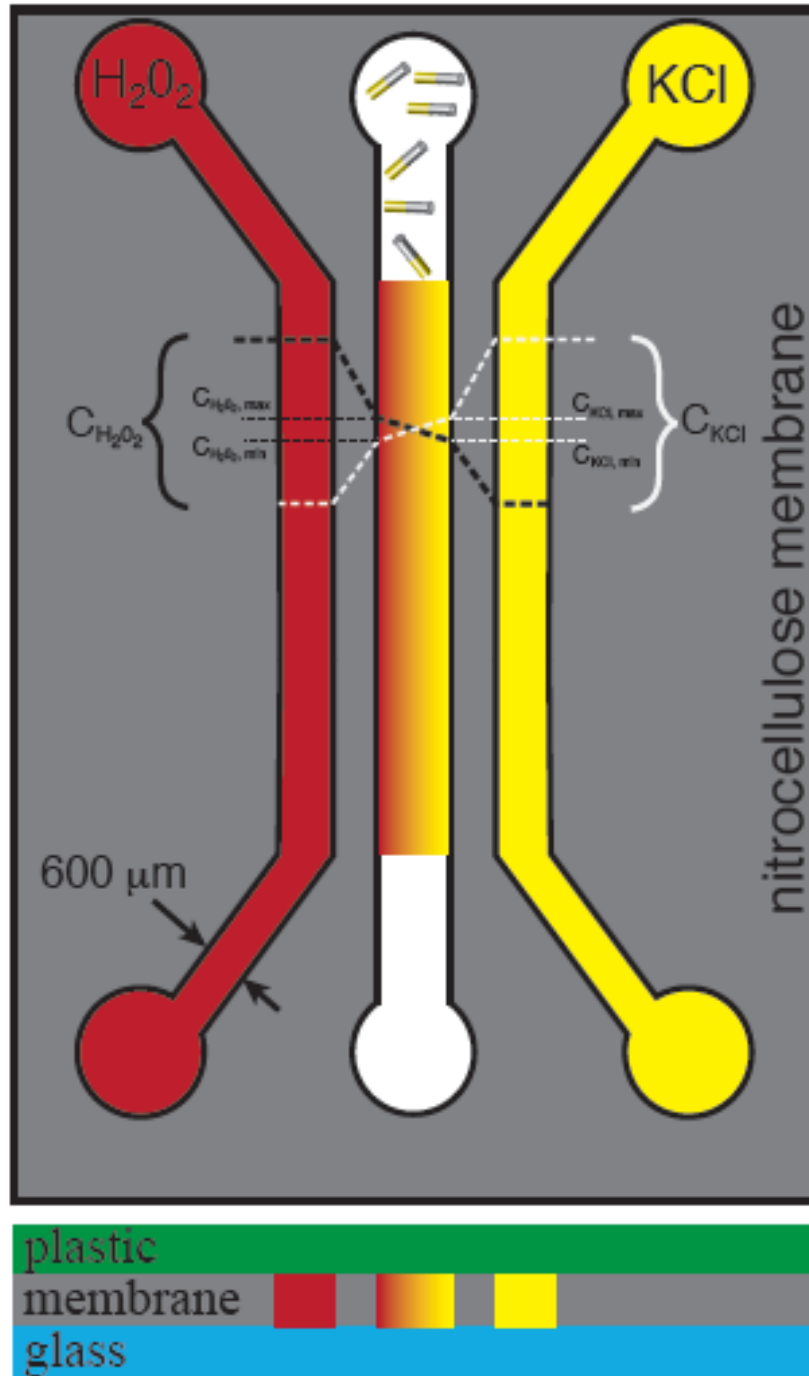


Figure 30: Schematic of the structure used to generate steady-linear chemical concentration gradients for the chemokinesis assays. Red depicts an aqueous solution containing H_2O_2 and the yellow depicts an aqueous salt solution. The solutions diffuse through the membrane and form linear gradients in the center channel.

4.4.2 Structure Fabrication

The structures incorporate a 1/8th inch thick 25x25mm acrylic lower plate with six screw holes and a viewing port cut out using a CO₂ laser ablator (M-360, Universal Laser Systems Inc., Scottsdale, AZ). A similarly cut 150 μm thick sheet of double stick Mylar (3M, St. Paul, MN) is placed on top of the lower plate aligned using six screws. Four more sheets of double stick Mylar are cut 1cm x 1.5 cm with the same viewing port. The 4 sheets are adhered to a 1mm thick, 1cm x 1.5 cm piece of a glass slide to match the thickness of a 1/8th inch piece of acrylic. Another piece of 1/8th inch acrylic is cut with the six screw holes and a 1cm x 1.5cm square removed from the center to accommodate the glass piece. A Mylar sheet is then ablated to the dimensions of the channel and placed on the glass/acrylic layer. Next a 120 μm thick nitrocellulose membrane (0.4 μm pore size) (Whatman, Cat. No. F3120-6; Maidstone, UK) sheet is similarly cut with the channel widths reduced by 100 μm to account deformation of the Mylar sheets when the structure is assembled. The membrane sheet is placed on the double stick Mylar sheet topping the structure assembled thus far, aligned with the screws and pressed down using a piece of acrylic. Another Mylar sheet similarly cut is placed on top of the nitrocellulose sheet. Finally an upper acrylic plate is cut with the six screw holes, 2mm diameter holes as ports for the center channel and 0.4mm diameter holes as ports to the two outer channels. Stainless steel tubes (NE-1300-01, New England Small Tube Corp., Litchfield NH) are inserted into the ports for the outer channels and the edges are sealed with epoxy to prevent leaks. Tygon tubing (1/16'' ID, McMaster-Carr, Santa Fe Springs CA) is used to

interface between the syringes and the stainless steel tubes at one end of the structure and between the stainless steel tubes and a waste beaker at the other end of the structure. Each channel is cut 400 μm wide and the nitrocellulose sidewalls are 1mm thick. Nuts and washers are used to screw the structure tight carefully. A sufficient seal typically occurs just prior to the nitrocellulose cracking from the stress. Sidewalls narrower than 1mm typically result in the sidewalls collapsing when the structure is tightened.

The glass lower surface of the channel is used for experimental considerations. High concentrations of nanomotors in H_2O_2 solutions result in excessive O_2 bubble formation. In microchannels these bubbles cannot escape and they plague imaging when in the vicinity of motors, provide an energy well at the interface that traps motors that happen to interact with the interface, and ultimately impose flows that prevent any meaningful analysis. Typically the issue of O_2 formation is addressed by using very low concentrations of nanomotors. For this statistical analysis of the global behavior of nanomotors it is necessary to use a relatively high concentration of motors. Using a hydrophilic glass surface for the bottom of the channel and a hydrophobic acrylic surface for the top of the channel causes the O_2 bubbles to form on the upper surface of the channel. On the upper surface of the channel the bubbles reside above the working plane, which is just above the glass surface. A vast majority of the nanomotors settle quickly to the lower surface and move around along that surface with insignificant out of plane motion.

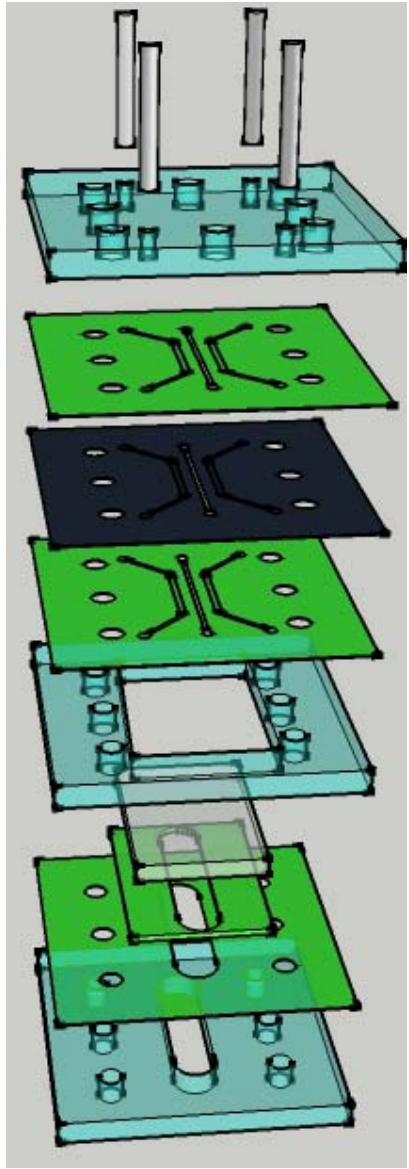


Figure 31: Exploded view of the steady-linear concentration gradient generator used for the chemokinesis assays.

The evolution of the microchannel structure is shown in Figure 32 through Figure 37. In the initial design (Figure 32), a nitrocellulose membrane, cut to the dimensions of the channel is placed on a glass microslide. The glass slide and the membrane layer are pressed tightly between two acrylic plates (one serving as the channel's upper surface, the other cut with a view port for imaging). This design most closely matches Diao's static gradient generator.(Diao et al. 2006) The nanomotors swam effectively in this structure, but pressure driven flow worked its way above and below the channel walls. The leak implied a poor sealing, to remedy the poor sealing I placed the entire structure in an oven at temperatures above the glass transition temperature for the acrylic. This mild sintering step did not improve the sealing issue. Instead, a new design (Figure 33) was considered that would allow the bolts to be positioned closer to the channel to increase the pressure used to sandwich the structure. Our inability to repeatably make precision glass cuts, the lower surface was changed to acrylic. The generation 2 (Figure 33) design still allowed pressure driven flow to affect the flow of the objects in the center channel, which implied insufficient sealing. The flow in the center channel was visualized using 500 nm diameter red fluorescent polystyrene spheres (Duke Scientific Inc., Fremont, CA, USA). To improve sealing, the 3rd generation design (Figure 34) incorporated 2 more bolts (with the previous bolts brought closer to the channels) and double sticky Mylar was added on both sides of the nitrocellulose membrane to serve as a gasket. The generation 3 structure provided a sufficient seal. The design was improved upon (generation 4, Figure 35) by using stainless steel tubes permanently affixed to the structure, to interface

with the tubes coming from the syringes. The 4th generation structures also proved a sufficient seal, permitting a static linear gradient to form. Unfortunately the nanomotors did not swim when distributed in the center channel of the generation 3 and generation 4 structures. The next design (Figure 36) incorporated a small piece of a glass slide as the lower surface; in this case the motors swam well. However, this 5th generation design resulted in the membrane cracking as the structure was tightened, this case, glass cover slip fragments were used to comprise the lower surface. The nitrocellulose membrane underwent significant deflection as the structure was tiered down and the membrane deformed around the glass coverslip fragment. The membrane was then cut to the dimensions of the slide fragment (Figure 36) and the seal was again insufficient. Finally a glass slide fragment was used for the lower surface and the structure depicted in Figure 31 was created. An image of this structure is shown in Figure 37. The final structure resulted in motors swimming within the center channel, and a linear static concentration gradient in the center channel.



Figure 32: Initial channel structure design. Lower surface is a glass microslide. The structure is sandwiched between two acrylic plates.

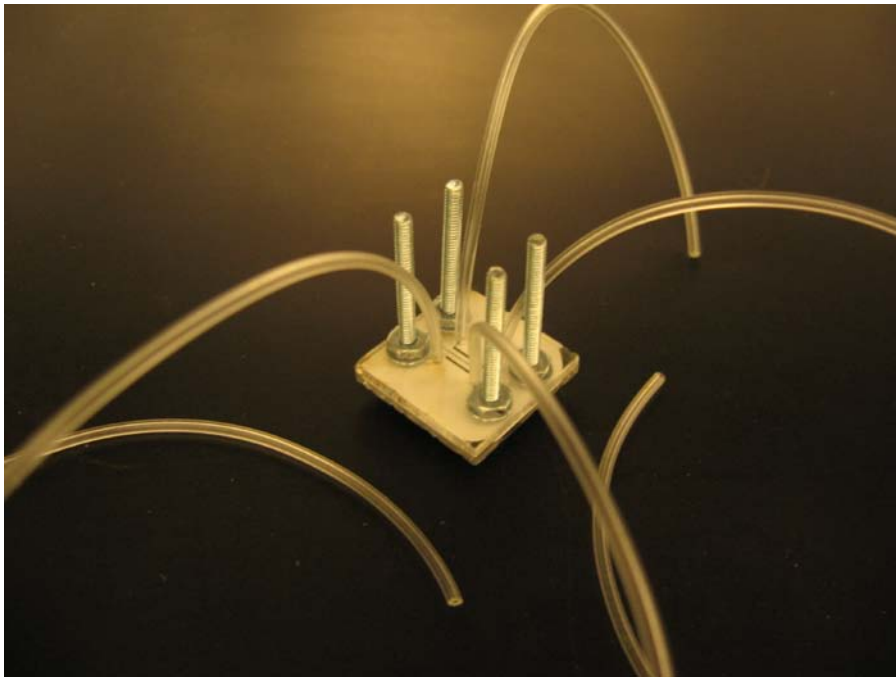


Figure 33: Generation 2 channel design. Upper and lower channel surfaces are acrylic.

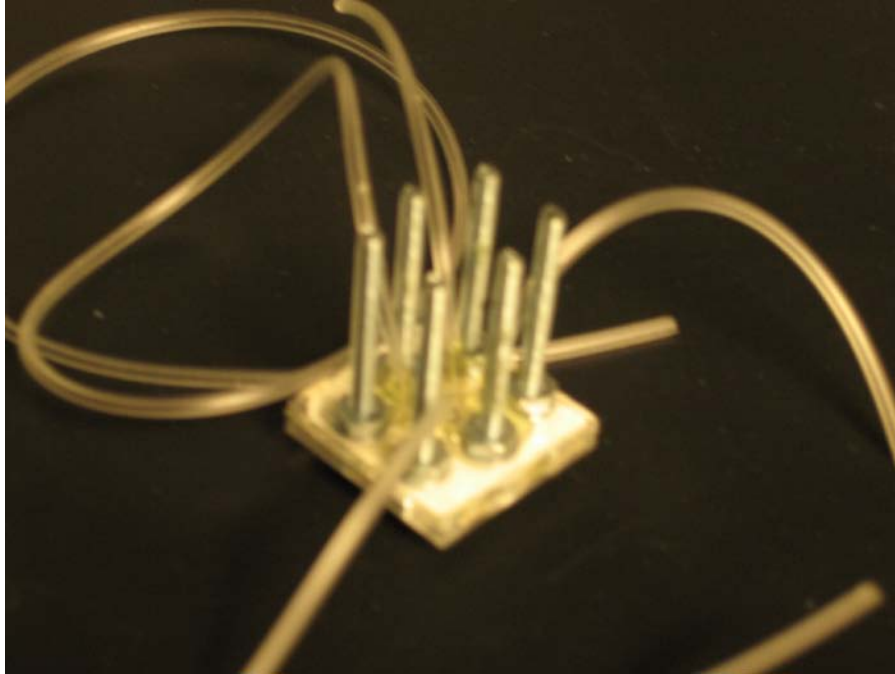


Figure 34: Generation 3 channel design. Upper and lower surfaces are acrylic. 6 screws and Mylar layers are introduced for sealing.

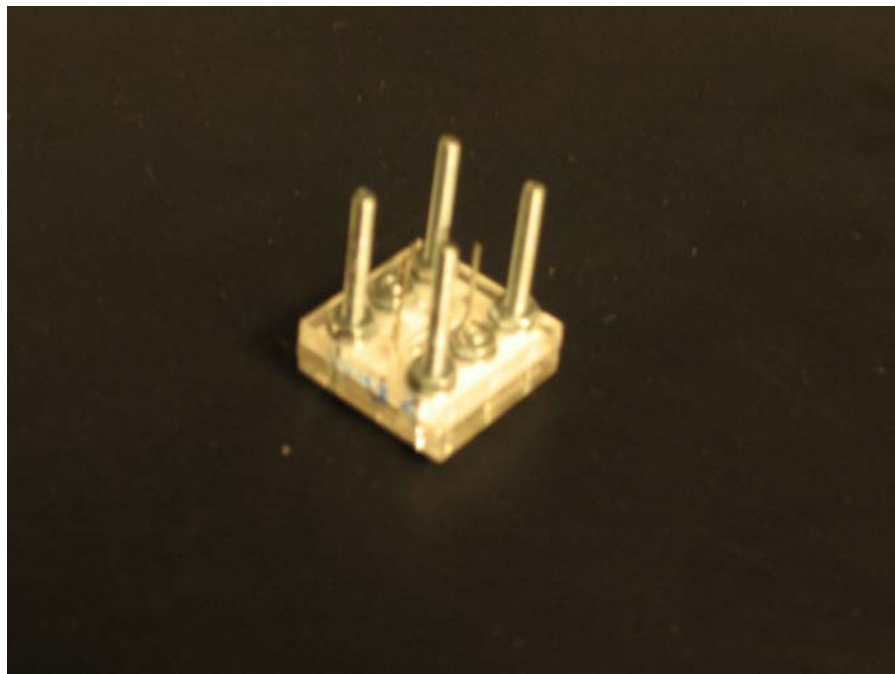


Figure 35: Generation 4 channel design. Upper and lower surface are acrylic, and stainless steel tubes are used to interface with tubing.

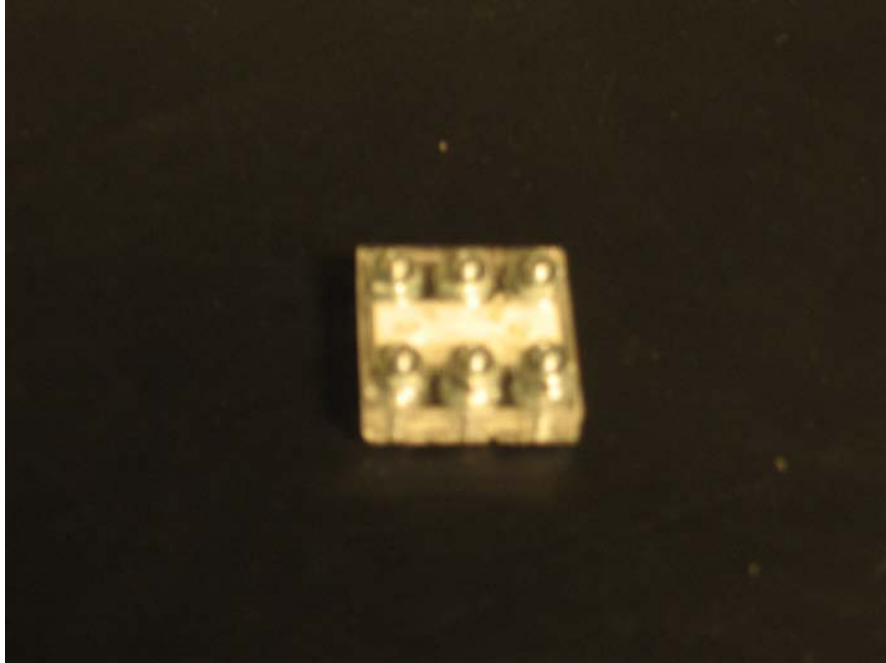


Figure 36: Generation 5 channel design. Lower surface is glass, upper surface is acrylic.



Figure 37: Final channel design.

4.4.3 Chemical Concentrations

At sufficiently high Peclet number flow in the concentrations can be assumed to be uniform everywhere in the outer channels. For diffusivities on the order of $D = O(10^{-9} \text{ m}^2/\text{s})$, with a channel cross-sectional area of $400 \text{ } \mu\text{m} \times 420 \text{ } \mu\text{m}$ ($2.5 \times 10^{-7} \text{ m}^2$) and a flow rate $5 \text{ } \mu\text{L}/\text{min}$ ($8.333 \times 10^{-11} \text{ m}^3/\text{s}$), the Peclet number becomes 200. This can be interpreted as the flow would have to travel 200 channel widths before the concentration diffused across one channel width and in this case the channel lengths (15 mm) are only 25 channel widths. Therefore, the concentration profile can be assumed to be uniform along the axis of the channels. The concentration profile can be approximated using Fick's second law, where the time rate of change of the concentration is equal to the spatial gradient in flux. At steady state, the spatial gradient in flux is zero and therefore the flux must be constant. At steady state,

$$\text{Total Flux} = -AD \frac{dC}{dx} = \text{constant},$$

$$\Rightarrow A_1 D_1 \frac{dC}{dx_1} = A_2 D_2 \frac{dC}{dx_2}.$$

In this case, the diffusivities of both the salt and the H_2O_2 can be assumed to be uniform throughout the pores and the channels. (Pores of diameter $0.4 \text{ } \mu\text{m}$ are sufficiently large to not be concerned with ion exclusion.) Therefore,

$$A_1 \left(\frac{dC}{dx} \right)_1 = A_2 \left(\frac{dC}{dx} \right)_2.$$

With a membrane porosity of 50%, $A_1 = A_2/2$, where A_1 is the cross-sectional area of the membrane and A_2 is the cross-sectional area perpendicular to the direction of diffusion in the channel. Therefore,

$$\left(\frac{dC}{dx}\right)_{\text{membrane}} = 2 \left(\frac{dC}{dx}\right)_{\text{center channel}}.$$

Because the gradients are linear and there are two membrane walls and one center channel, this can be rewritten as:

$$\left(\frac{\Delta C}{\Delta x}\right)_{\text{membrane}} = 2 \left(\frac{\Delta C}{\Delta x}\right)_{\text{center channel}},$$

$$\Rightarrow \frac{\Delta C_{\text{membrane}}}{2w_{\text{membrane}}} = 2 \frac{\Delta C_{\text{center channel}}}{w_{\text{center channel}}}.$$

Where,

$$\Delta C_{\text{membrane}} + \Delta C_{\text{center channel}} = \Delta C_{\text{total}}.$$

The membrane wall thicknesses are 1 mm, and the center channel width is 0.4 mm. Therefore,

$$\Delta C_{\text{membrane}} = 10\Delta C_{\text{center channel}},$$

$$\Delta C_{\text{center channel}} = \frac{\Delta C_{\text{total}}}{11}.$$

As a result, the change in concentration across the center channel is 1/11 the total concentration in the outer channels. In other words, if 5% H₂O₂ were introduced to the left channel, the maximum concentration of H₂O₂ the motors would see on the left side of the channel would be 2.72% while the minimum concentration would be 2.27% on the right side, a total change of 0.45%. This is insufficient for measuring meaningful orthokinesis. To amplify this as much as possible, I introduce 30% H₂O₂ into the left channel, resulting in a change of 2.7% H₂O₂. Specifically $C_{\text{min,H2O2}} = 13.6\%$, and $C_{\text{max,H2O2}} = 16.3\%$. To further amplify the orthokinetic response I introduce salt into the right channel. KCl was selected for the salt solution because the diffusivities of potassium and chloride ions are very

similar, minimizing the development of a diffusion potential that would amplify a diffusiophoretic response to the gradient in salt concentration.

100 μM KCl + 1 μM Fluorescein was used as the salt solution. $C_{min,KCl} = 45.5$ μM , and $C_{max,KCl} = 54.5$ μM . $C_{min,Fl} = 455$ nM, and $C_{max,Fl} = 545$ nM.

CHAPTER 5

RESULTS AND DISCUSSION

5.1 Brownian Dynamics Simulation Results:

The relationship between motor speeds and hydrogen peroxide concentrations has been shown in the literature to be roughly linear for a variety of different types and shapes of motors. I have shown this relationship for 2, 3 and 5 micron diameter polystyrene spheres half coated with one side coated in platinum and the other side coated in gold (Figure 38). Howse et al. have shown this with 1.62 μm diameter polystyrene-platinum Janus spheres as shown in Figure 39. Similarly, Laocharoennsuk et al. showed a linear relationship between the speeds of gold-platinum nanorods and hydrogen peroxide concentration. Finally, Kagan et al. showed a similar linear relationship between gold-platinum nanorods and silver-nitrate salt concentrations (Figure 40). In each of these cases, the relationships are linear, but the slopes are different. A slight relationship between H_2O_2 concentration and rotational speeds has also been shown by Howse et al. (Figure 41).

Figure 38: Average bimetallic, spherical micromotor speeds versus H₂O₂ concentration for □) 2 μm, (Δ) 3 μm, and (○) 5 μm diameter spheres (the error bars correspond to a single standard deviation).

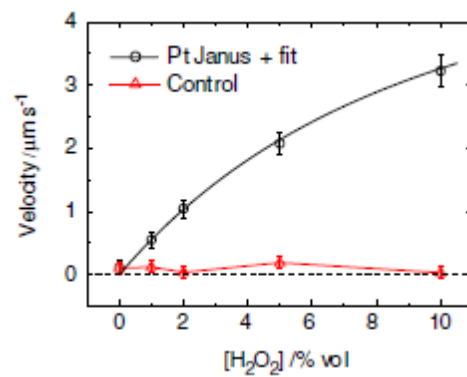


Figure 39: Average speed versus H₂O₂ concentration for 1.62 μm half platinum-coated polystyrene spheres. Adapted with permission from Howse, J. R., et al. "Self-Motile Colloidal Particles: From Directed Propulsion to Random Walk." *Physical Review Letters* 99.4., Copyright 2007, American Physical Society. <http://dx.doi.org/10.1103/PhysRevLett.99.048102>

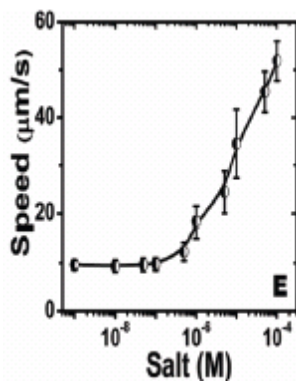


Figure 40: Average speed versus silver salt concentration with 5 wt % aqueous H_2O_2 for bimetallic Au-Pt (red) and Au-Pt (with carbon nanotubes, blue) nanorods $2\mu\text{m}$ in length and 360 nm in diameter. Adapted with permission from Kagan, D., et al. "Chemical Sensing Based on Catalytic Nanomotors: Motion-Based Detection of Trace Silver." *Journal of the American Chemical Society* 131.34 : 12082-+, Copyright 2009, American Chemical Society. <http://dx.doi.org/10.1021/ja905142q>

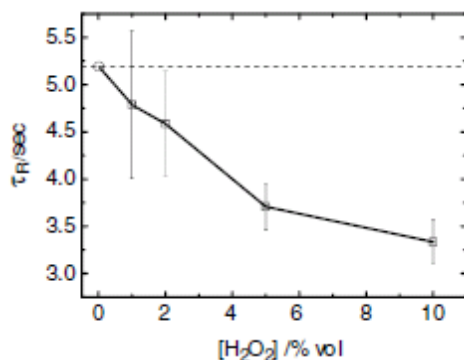


Figure 41: The inverse of the average rotational diffusivity versus H_2O_2 concentration for $1.62\mu\text{m}$ half platinum-coated polystyrene spheres. Adapted with permission from Howse, J. R., et al. "Self-Motile Colloidal Particles: From Directed Propulsion to Random Walk." *Physical Review Letters* 99.4., Copyright 2007, American Physical Society. <http://dx.doi.org/10.1103/PhysRevLett.99.048102>

To assess the global behavior of nanomotors when subject to a gradient in hydrogen peroxide concentration, several different combinations of slopes for

both linear relationships between fuel concentration and nanomotor axial speeds and linear relationships between fuel concentration and nanomotor rotational diffusivity were simulated. For each run, the nanomotors were assigned a distinct relationship between the fuel concentration and both the axial velocity of the nanomotors due to the presence of the fuel (orthokinetic relationship) and the rotational diffusivity (klinokinetic relationship). In the simulations, the fuel concentration is normalized such that the maximum concentration is 1. At a concentration of zero, there is no chemokinetic effect on the nanomotors. Furthermore, in these first simulations there is no base axial velocity as would be the case if the fuel were silver being added to a solution already containing uniformly distributed hydrogen-peroxide (to be simulated in the future). As a result, the relationships used to determine chemokinetic velocity and chemokinetic rotational diffusivity with respect to fuel concentration are determined simply by specifying the chemokinetic velocity and rotational diffusivity associated with the maximum concentration. Finally, the chemokinetic velocities and rotational diffusivities are normalized by characteristic velocities and rotational diffusivities for nanomotors undergoing only Brownian motion. In these two-dimensional simulations, 10,000 nanomotors started out uniformly distributed throughout a square region 100 microns in both the x- and y-directions (Figure 42). The fuel concentration was defined spatially by a stationary gradient prescribed by the equation:

$$\frac{c}{c_0} = e^{\frac{-x^2}{2\sigma^2}}.$$

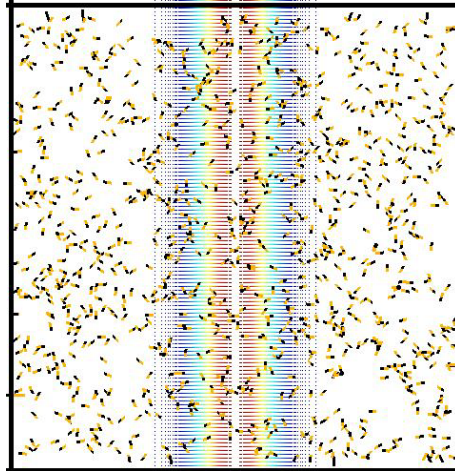


Figure 42: Initial distribution of nanomotors simulated by the Brownian dynamics model.

The simulations were run for 500 time steps, with a Δt of 0.1, resulting in a duration of 50 seconds. In nearly all of the cases run, the nanomotors would reach a relatively steady statistical distribution. Depending on the rotational and translational relationships between the nanomotor and the fuel, the distribution would favor the region of high fuel concentration, the regions of low fuel concentration, or not respond to the fuel concentration. A chemotactic index is used to measure the response. Here the chemotactic index is defined as the number nanomotors within two standard deviations of the fuel gradient on either side maximum in fuel concentration divided by the number of nanomotors within two standard deviations of either of the side walls where the concentration is the lowest. Figure 43 shows a case in which the nanomotors' global behavior resembles strong positive chemotaxis after a simulated run time of 19.9 seconds. For the simulation represented in Figure 43, the maximum chemotactic velocity was set to $20 \mu\text{m/s}$ at the low concentrations and 0 at the high concentrations.

After normalizing by the translational velocity associated with Brownian motion (approximately 5 $\mu\text{m/s}$ (Calvo-Marzal et al. 2009)), this relationship results in $\frac{\partial u^*}{\partial c^*} = -4$. Similarly, the maximum angular velocity was set to 100 times the maximum angular velocity used to simulate Brownian diffusion and corresponded to the highest concentration, resulting in $\frac{\partial \dot{\theta}^*}{\partial c^*} = 100$. The chemotactic index increases and then levels off just above 10 at about 20 seconds for this case. The chemotactic index continues to oscillate around a value representing an equilibrium distribution for the simulation. These oscillations dampen with increases in the number of nanomotors being simulated. Similar equilibrium chemotactic indices are plotted in Figure 44 for several different rotational and translational velocity–fuel concentration relationships. Figure 44 clearly depicts a maximum in positive chemotaxis occurring when the velocity decreases as fuel increases and when rotational velocity increases as fuel concentration increases. There is a maximum in chemotactic repulsion when the nanomotors move faster and the rotational velocity decreases at higher concentrations.

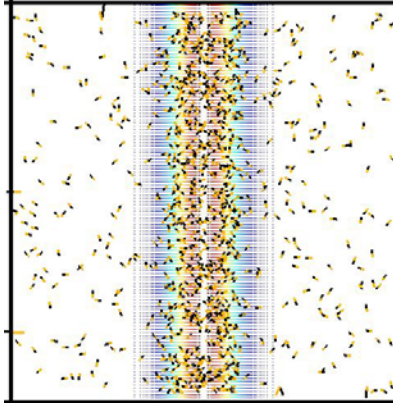


Figure 43: Final steady-state distribution of nanomotors simulated by the Brownian dynamics model showing positive chemokinesis.

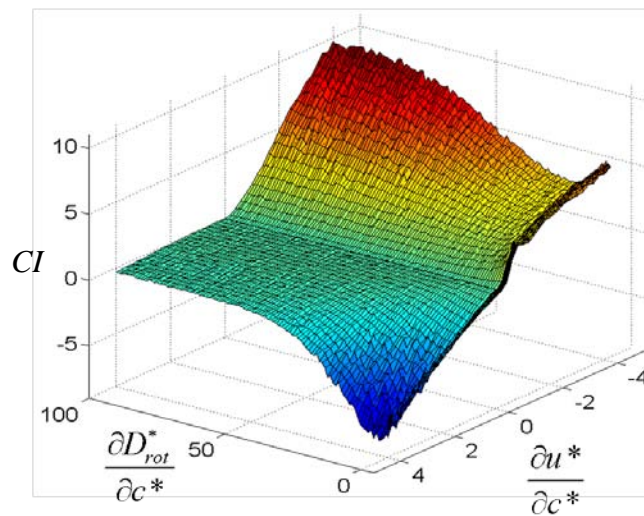


Figure 44: Chemotactic index phase diagram.

Typically chemotaxis involves a diffusing fuel distribution. As a result, in addition to simulating the chemotactic index, it is important to consider the chemotactic response time τ . Figure 45 shows the chemotactic index as function

of time for three different cases. The red curve corresponds to a case in which the nanomotor velocity (directionally specific) decreases linearly with an increase in fuel concentration from $100 \mu\text{m/s}$ where $c^*=0$, to $0 \mu\text{m/s}$ where $c^*=1$, and the rotational diffusivity is unchanged with fuel concentration. In this case, the chemotactic index is high, but the response time is relatively low. The final chemotactic index of approximately 10 indicates that when the system reaches steady state, the number of nanomotors in the higher fuel concentrations is about ten times the number of nanomotors in the lower fuel concentration. The black curve represents a case with the reverse behavior but a comparable response. In this case, the nanomotor velocities increase linearly with the fuel concentration from $0 \mu\text{m/s}$ where $c^*=0$, to $20 \mu\text{m/s}$ where $c^*=1$, and the rotational diffusivity increases from about $0.064 \text{ rad}^2/\text{s}$ to $0.26 \text{ rad}^2/\text{s}$. Finally, the blue curve depicts high chemotactic index case with a significantly shorter response time. In this case, the nanomotor velocities decrease linearly with an increase in fuel concentration from $20 \mu\text{m/s}$ where $c^*=0$, to $0 \mu\text{m/s}$ where $c^*=1$, and the rotational diffusivity increases from about $0.064 \text{ rad}^2/\text{s}$ to $160 \text{ rad}^2/\text{s}$.

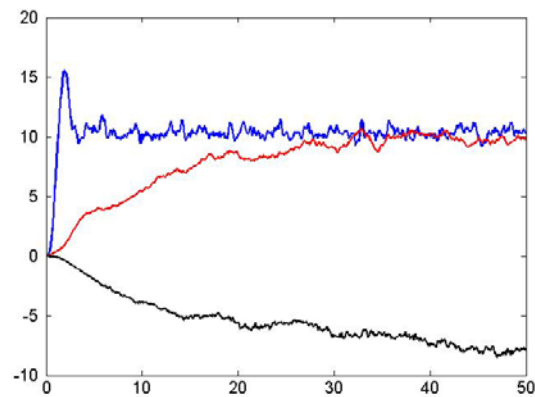


Figure 45: Chemotactic index versus time.

For simplicity, each case is treated as a first order transient response, and the response time is defined as the time the system takes to achieve 63.2% of the steady state value.(Figliola and Beasley 2006) While Figure 45 clearly illustrates a case with a second order transient response, the time it takes the system to initially reach the 63.2% value is still taken, because in the case of a diffusing a fuel concentration gradient predicting the ability to observe a chemotactic response is of greater concern than accurately predicting details of the steady state behavior. Figure 46 shows a representative plot of the response time versus the chemotactic velocity at $c^*=1$ for specific relationship between rotational diffusion and fuel concentration. For the positive velocities, the velocity corresponding to $c^*=0$ is $0 \mu\text{m/s}$, and for the negative velocities, the velocity corresponding to $c^*=0$ is $100 \mu\text{m/s}$. In either case, the velocity is linearly related to the fuel concentration between $c^*=0$ and $c^*=1$.

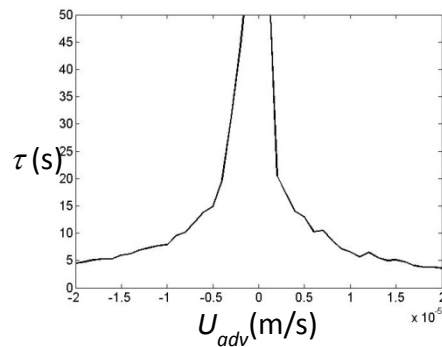


Figure 46: Response time vs. chemotactic velocity at maximum fuel concentration.

Consider the comparison between τ and the characteristic time scale of diffusion for the fuel $\tau_{\text{fuel}}=L^2/D_{\text{fuel}}$. Here L is the width of the nanomotor distribution across which one expects to see chemotaxis, and it corresponds to the width of the distribution used to determine τ , in this case $L=100 \mu\text{m}$. For hydrogen peroxide, $D_{\text{H}_2\text{O}_2} = 1.3 \times 10^{-9} \text{ m}^2/\text{s}$, resulting in $\tau_{\text{H}_2\text{O}_2}=7.69 \text{ s}$. Therefore, the response time for the nanomotors in hydrogen peroxide must be less than 7.69 seconds in order to observe chemotactic behavior in a diffusing gradient in hydrogen peroxide concentration.

Thus far, I have looked at chemokinetic behavior of nanomotors as a function of two independent characteristics of the nanomotors, the relationship between directional velocity and fuel concentration, and the relationship between rotational diffusivity and the fuel concentration. Specifically I have looked at cases where these relationships are linear. However, for a specific rotational diffusivity and a specific directional velocity, a batch of motors will have a corresponding effective diffusivity. Returning the equation for effective diffusivity presented by Howse et al.:

$$D_{\text{eff}} = D + \frac{1}{4} \frac{U_{\text{adv}}^2}{D_{\text{rot}}},$$

one can see that there are multiple combinations of U_{adv} and D_{rot} that will result in the same effective diffusivity.

5.2 Variable Diffusion PDE Model:

Recall the generalized diffusion equation for variable diffusivity discussed in section 3,

$$\frac{\partial C}{\partial t} = +D\nabla^2 C + (1 + \alpha)\nabla D \cdot \nabla C + \alpha C \nabla^2 D.$$

The need to choose a value of α that corresponds to the physics of the problem prevents a quantitative analysis of chemokinetic behavior simply from solving the PDE. However, this approach can be used for a rapid qualitative analysis even when the value of α is unknown. It has been seen from the Brownian dynamics simulations, that there is a non-uniform motor concentration at equilibrium, when the motor has a chemokinetic response to a chemical that is non-uniformly distributed. This implies the motor distribution has a non-zero value for α in a spatial gradient of a chemokinetically active chemical. The above equation can be solved numerically using a simple first-order-accurate forward Euler in time and second-order-accurate center difference in space method. In a one-dimensional analysis, this results in a tri-diagonal matrix problem that I solve using the Thomas algorithm. The one-dimensional discretized equation is as follows:

$$C_{j-1,i} \frac{\Delta x^2}{\Delta t} = \left[D_i + \frac{1+\alpha}{4} (D_{i+1} - D_{i-1}) \right] C_{j,i+1} + \left[\alpha (D_{i+1} - 2D_i + D_{i-1}) - 2D_i - \frac{\Delta x^2}{\Delta t} \right] C_{j,i} + \left[D_i - \frac{1+\alpha}{4} (D_{i+1} - D_{i-1}) \right] C_{j,i-1}.$$

A no flux condition is enforced at the boundaries, such that $D\nabla C = -\alpha C\nabla D$.

Figure 47 depicts the solution to this equation at various times, including the final steady state solution for a non-zero α . In this case, there is a Gaussian concentration profile for which there is an inverse relationship between the

concentration and the advective velocity of the chemokinetic object. In these figures, the concentrations and effective diffusivities are normalized by their maximum corresponding values. In this simulation, the motor exhibits a purely orthokinetic response with the chemokinetic velocity varying linearly with concentration as follows:

$$\mathbf{U}_{adv} = 20 \frac{\mu\text{m}}{\text{s}} \left(1 - \frac{c}{c_{\max}}\right).$$

The relationship between effective diffusivity and advective velocity was determined using the Brownian dynamics simulation and follows the equation from Howse et al.:

$$D_{eff} = D + \frac{1}{4} \frac{U_{adv}^2}{D_{rot}},$$

with $D=1.09\text{e-}12\text{m}^2/\text{s}$, and $D_{rot} = 3 \text{ rad}^2/\text{s}$. In this case, there is no directional sensing ability being modeled, yet there is an accumulation of motors at the region of high concentration. This resembles a chemotactic response, but instead is pure chemokinesis.

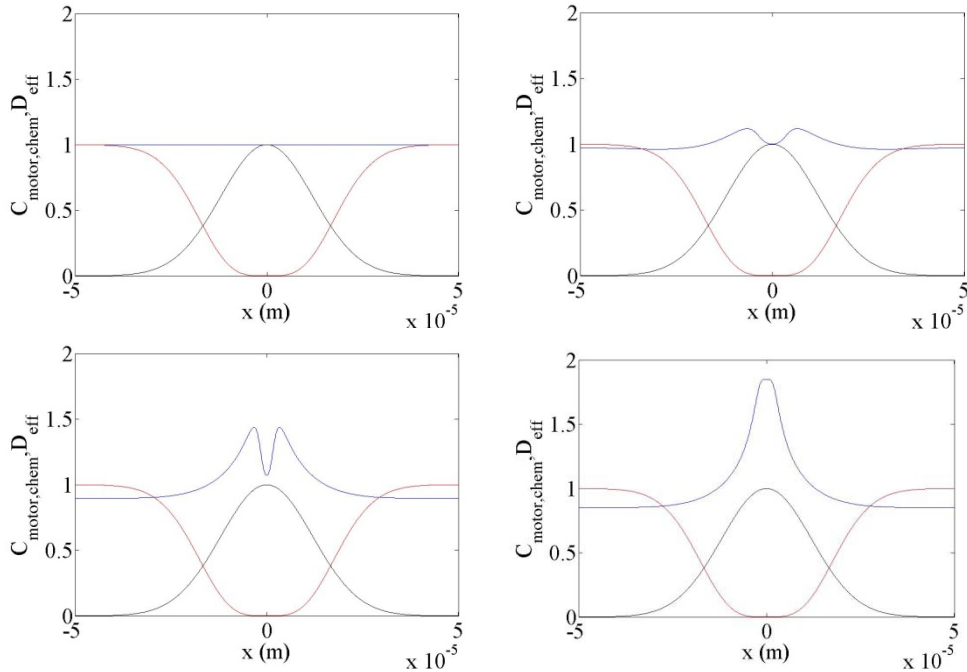


Figure 47: Normalized motor concentration (blue), chemical concentration (black), effective diffusivity (red) for an object that decreases axial velocity with increases in chemical concentration at $t = 0, 0.1, 1,$ and 10 seconds in a region bound by reflective walls on the left and right.

To illustrate the distinction between a purely diffusive chemokinetic response, and a chemotactic response, the bounding reflective walls are removed and the simulation is run again and the results are depicted in Figure 48. As time increases, a local maximum in motor concentration develops at the peak in chemical concentration. However the overall motor concentration diffuses away from the peak in chemical concentration, with the motor concentration continually decreasing after a brief initial increase at the maximum in chemical concentration. This behavior is distinctly different from chemotaxis. Chemotaxis would result in a net migration of the motors towards or away from the maximum in chemical

concentration regardless of the presence of or proximity to bounding walls. In this case, there is a net migration of the motors towards the maximum in chemical concentration when they are confined by reflective walls (Figure 47) and a net migration away from the maximum in chemical concentration when the walls are removed (Figure 48).

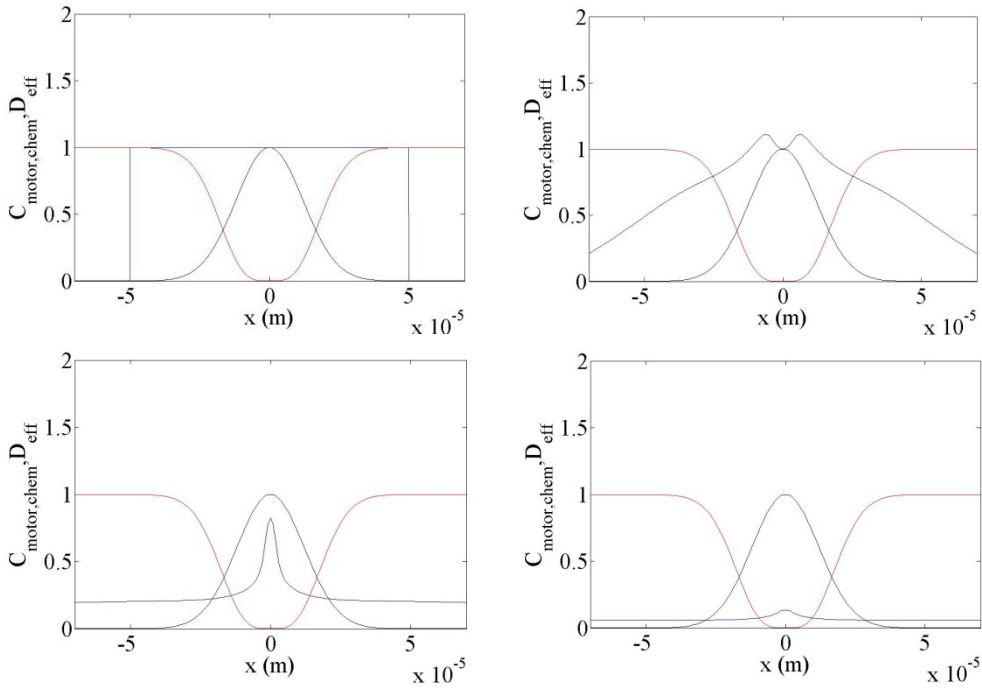


Figure 48: Normalized motor concentration (blue), chemical concentration (black), effective diffusivity (red) for an object that decreases axial velocity with increases in chemical concentration at $t = 0, 0.1, 5,$ and 60 seconds, in an unbounded region.

For the experiments the gradient in chemical concentration was linear, with the maximum effective diffusivity on the left side of the channel (rather than the center) and the minimum diffusivity on the right side of the channel. For these cases, the chemotactic index was measured as the number of motors on the low

effective diffusivity side divided by the number of motors on the high effective diffusivity side. The resulting chemotactic index as a function of time for this configuration from both the Brownian dynamics simulations and the PDE analysis were compared, and a value of $\alpha = 2/3$ (an approximation fit as discussed in section 3.1) was necessary to match both the temporal response and the steady state chemotactic index of the two models. Figure 49 shows the chemotactic index as a function of time for three sets of matching chemokinetic responses for both the Brownian dynamics model and the PDE model when $\alpha = 2/3$.

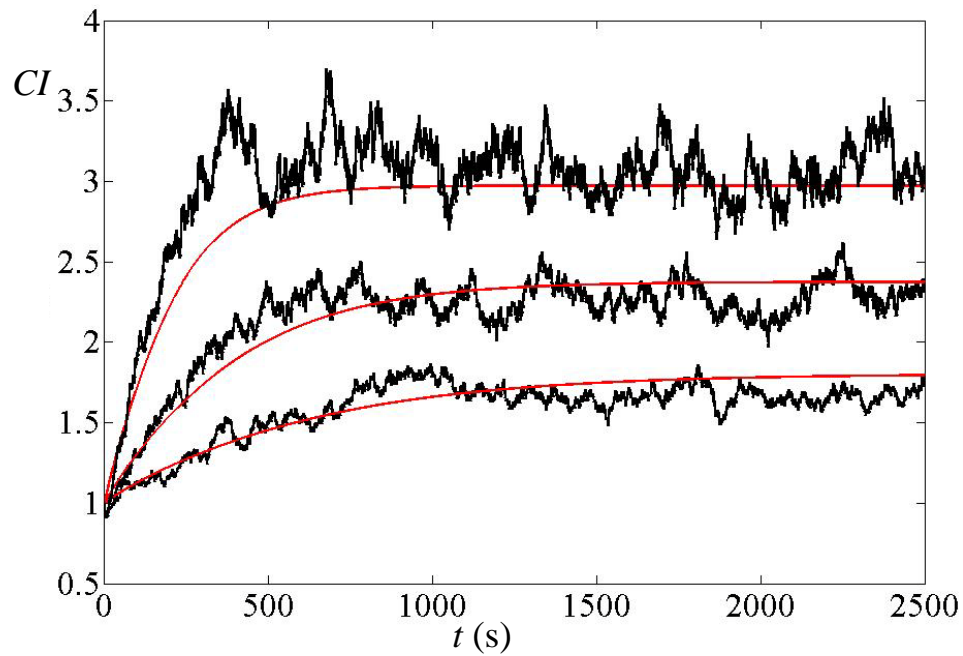


Figure 49: Comparison between PDE (red) and Brownian dynamics (black) models for $\alpha = 2/3$.

5.3 Experimental Results

5.3.1 Imaging

Epifluorescence microscopy is used to image the salt concentration gradient. Transmission microscopy is to image the nanomotors. The experimental set-up is shown in Figure 50. In both cases I use an inverted microscope (Nikon TE2000, Japan) with a 20x objective, NA = 0.45. For the fluorescence imaging I used metal halide illumination (EXFO X-Cite 120, Ontario, Canada) and an epifluorescence filter cube (Excitation 460-490 nm and emission 520-560 nm from Omega Optical, Brattleboro, VT) to image the gradient. For the transmission imaging I used Halogen illumination (Nikon Te2-PS100W, Japan). The images were captured using a CCD camera (Coolsnap HQ , Photometric, Tucson, AZ). In all cases, the exposure time was 100 ms.

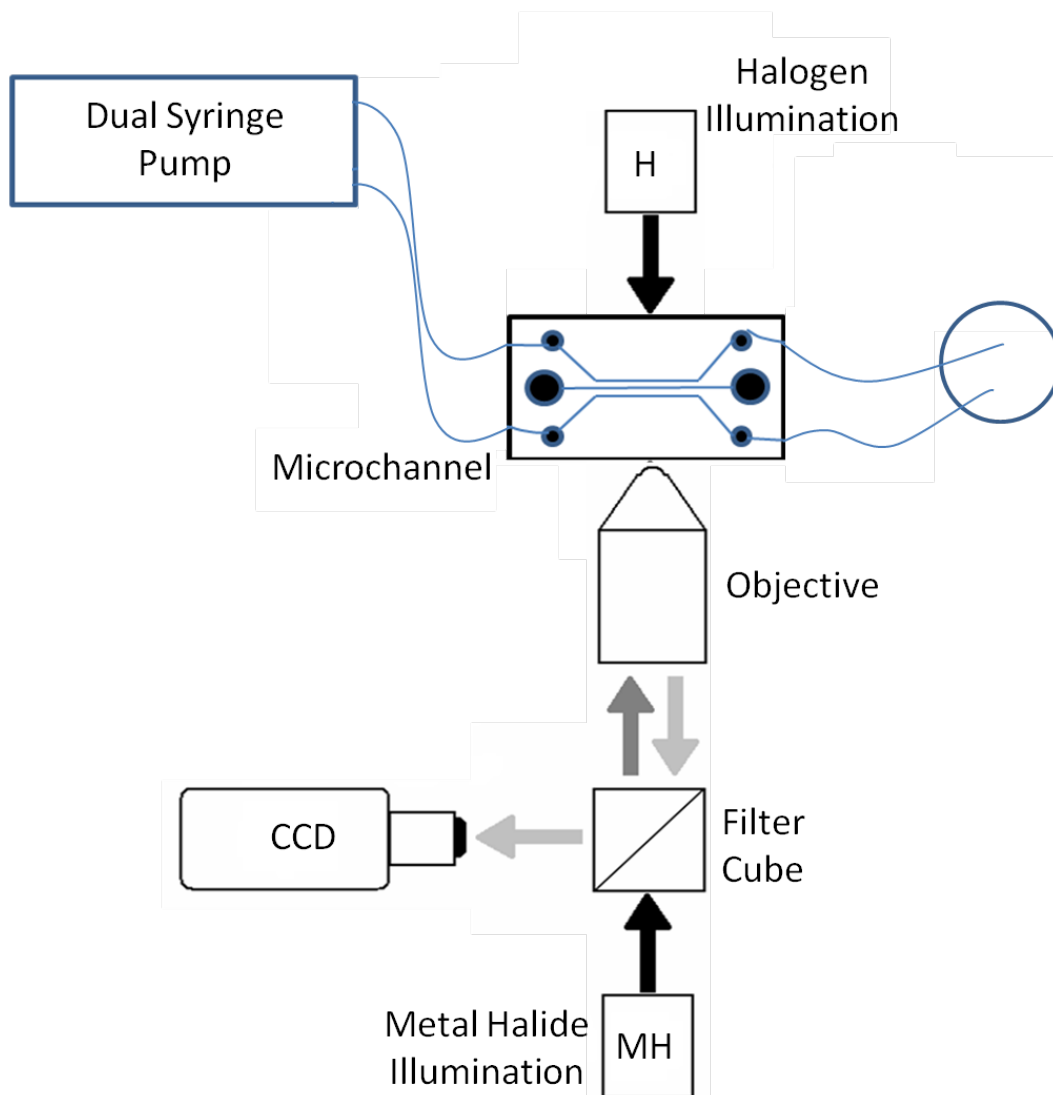


Figure 50: Experimental set-up of epifluorescence and transmission microscopy for imaging fluorescent dye concentration and nanomotor behavior. System components include a nitrocellulose microchannel, a dual syringe pump delivery system, a microscope with an epifluorescent filter cube and an objective, a metal halide bulb, a halogen bulb, and a CCD camera.

5.3.2 Speed

The nanomotors were tracked using an in-house particle tracking code written by Nathan Marine using MATLAB. The centroid of each nanomotor is used to define the position of the nanomotor at each time step. The centroid is calculated from the intensity weighted centers of the nanomotors in each frame. Particle centers at each time were paired using an optical flow algorithm. For each time step and each nanomotor, the distance between the previous position and current position was averaged with the distance between the current position and the next position to approximate an instantaneous displacement. The calculated displacements were multiplied by the frame capture rate to determine the instantaneous velocities. The net orthokinetic response was determined by measuring the average nanomotor velocity as function of position across the width of the channel as shown in Figure 51. For results depicted in Figure 51, there were more than 300 in the field of view that were tracked from 50 to 100 frames. The width of the channel is divided into twenty regions. The velocity represented for each region is the average of all the instantaneous velocities measured within that region. The error bars in Figure 51 correspond to one standard deviation from the mean.

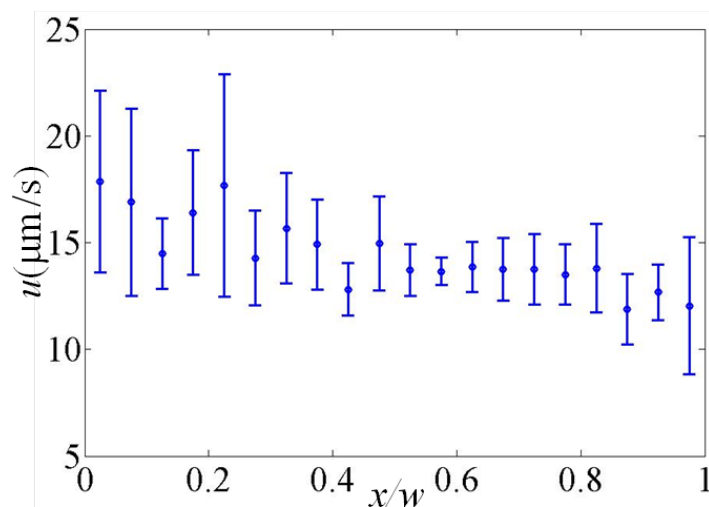


Figure 51: Average nanomotor velocity as a function of position across the width of the channel as a result of decreasing H_2O_2 and increasing KCl concentrations. The error bars represent 1 standard deviation.

Effective Diffusivity

The tracking code that is used to determine instantaneous velocities does so by dividing the displacement of the motor from one frame to the next by the time between successive frames. The code is not able to distinguish between the displacement associated with the axial velocity of the nanomotors due to the reaction induced charge auto-electrophoresis mechanism that drives the nanomotors and the displacement associated with random thermal motion. As a result, the measured instantaneous velocities are elevated well above the chemokinetic axial velocity of interest. The effects of thermal motion can be removed by analyzing the nanomotor behavior in terms of effective diffusivity (rather than speed) as a function of position.

The effective diffusivity of an individual motor is determined by analyzing the

entire path of the motor. The path of the motor is discretized at regular time intervals (as regulated by the frame capture rate) as shown in Figure 52. The displacement of motor from its original position at each time step is squared and is referred to as the squared total-displacement, given by:

$$(\Delta r_i(t))^2 = (r_i(t) - r_i(0))^2.$$

This squared total-displacement is typically averaged for several motors to determine a mean squared displacement as a function of time. The random nature of the orientation of the nanomotors from one frame to the next comes from random angular displacement due to thermal or Brownian motion. This random reorientation causes each successive position of the nanomotor to have random behavior even if the axial velocity is constant. The random successive step behavior is defined as random-walk behavior. The mean squared displacement as a function of time for random-walk type motion is given by the equation:

$$\langle \Delta r(t)^2 \rangle = 2D_{trans}\Delta t + \frac{V^2\Delta t}{2D_{rot}}(2D_{rot}\Delta t + e^{-2D_{rot}\Delta t} - 1). \text{(Howse et al. 2007)}$$

At short times this equation reduces to:

$$\langle \Delta r(t)^2 \rangle = 2D_{trans}\Delta t + V^2\Delta t^2 \quad \text{for} \quad \Delta t \ll \frac{1}{D_{rot}},$$

and at long times:

$$\langle \Delta r(t)^2 \rangle = \left(2D_{trans} + \frac{V^2}{D_{rot}}\right)\Delta t \quad \text{for} \quad \Delta t \gg \frac{1}{D_{rot}}.$$

From these limits, it is clear that the mean squared displacement of random walkers exhibit quadratic behavior for small values of Δt and transition to a linear relationship for large Δt , as depicted in Figure 54. The slope of this linear region is used to determine the effective diffusivity of a random walker. For pure

Brownian motion the relationship between diffusivity and mean squared displacement is:

$$\langle \Delta r(t)^2 \rangle = 2D_{trans}\Delta t.$$

From the previous two equations it is clear that an effective diffusivity for random walkers can be written as:

$$D_{eff} = D_{trans} + \frac{v^2}{2D_{rot}}.$$

In order to get the effective diffusivity of the nanomotors as a function of the position across the channel, the channel is divided into 20 equal segments. The squared displacement for each motor is determined as a function of time for the duration of the motors time within the field of view. The squared displacement for all the motors who's initial position is in the first segment are averaged and plotted as a function of time and a linear fit is used to determine the effective diffusivity for the motors in that region. The rotational diffusivity of the nanomotors is approximately $1.8 \text{ rad}^2/\text{s}$, therefore $1/D_{rot} = 0.556 \text{ seconds}$. The temporal regime much greater than $1/D_{rot}$ is taken as the time that is at least one order of magnitude greater than $1/D_{rot}$ and is therefore $t > 5.56 \text{ seconds}$. The frame capture rate is 2 frames per second, as a result, the linear regime is expected to start around frame 11. However, if there are not enough motors starting in a given region to perform the statistical analysis breaks down and erroneous effective diffusivities are obtained. Unfortunately the non-electrochemical decomposition H_2O_2 on the platinum surface of the nanomotors as well as the reduction and oxidation of H_2O_2 at the cathode and anode, respectively, result in $\text{O}_2(\text{g})$

formation. If the concentration of motors is too high, the oxygen will saturate the aqueous solution and will form bubbles that prevent the observation of the global behavior of the nanomotors in response to the chemical concentration gradients. The issue of oxygen bubble formation limits the number of nanomotors in the field of view to around 500 that are tracked for 100 frames. If these are uniformly distributed (which is only the case at the beginning of the experiments) this results in 25 motors per section. To allow for the statistical determination of the effective diffusivity, the path of each motor can be oversampled. The oversampling considers each consecutive point as the starting point of a new motor. When oversampling a single motor that is tracked for 100 frames effectively becomes 1 motor tracked for 100 frames, 1 virtual motor tracked for 99 frames, 2 virtual motors tracked for 98 frames etc., resulting in 81 motors tracked for at least 20 frames. The effective diffusivity for each region is then calculated using only the second 10 time steps for each nanomotor and virtual nanomotor. The starting point for each motor and virtual motor determines the section the motor's squared displacement contributes to. This amplifies 500 motors total to of 40500 motors. Figure 55 depicts the average nanomotor effective diffusivity measured using this approach. The results in Figure 55 correspond to the same experiment as the velocity data shown in Figure 51. The errorbars correspond to one standard-deviation.

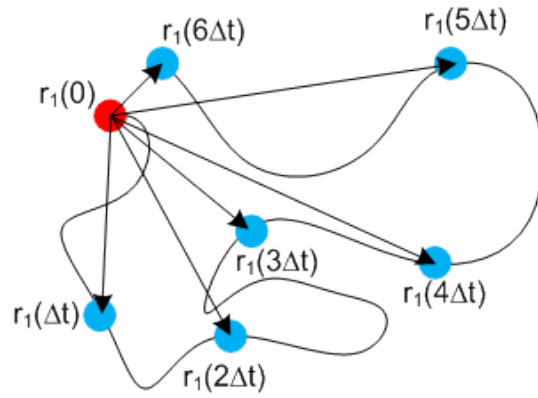


Figure 52: Example of a discretized nanomotor path. Red dot corresponds to the initial position.

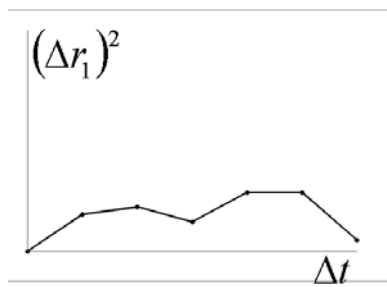


Figure 53: Total displacement squared as a function of the length of the time interval for a single motor.

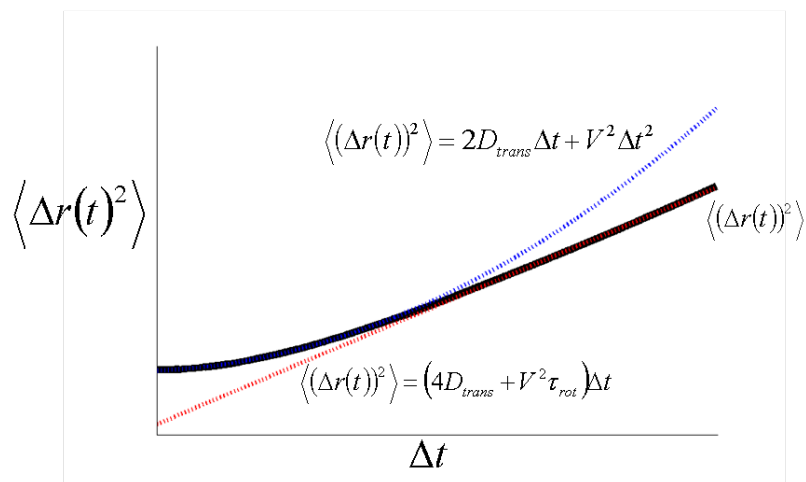


Figure 54: Mean squared displacement as a function of time for statistically random behavior (black), with a quadratic fit (blue) for short times, and a linear fit (red) for long times.

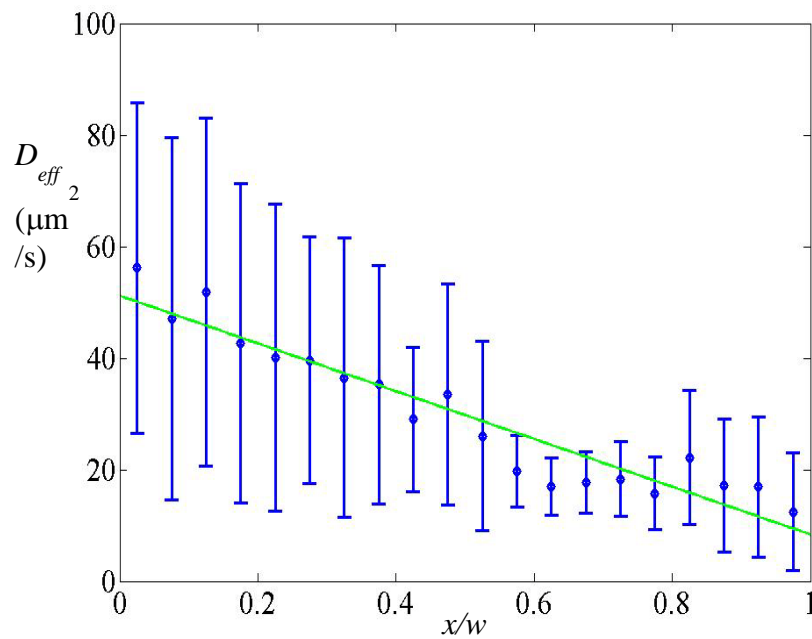


Figure 55: Average nanomotor effective diffusivity as a function of position across the width of the channel as a result of decreasing H_2O_2 and increasing KCl concentrations. The error bars represent 1 standard deviation.

5.3.3 Chemotactic Index

In each frame, the chemotactic index was measured as the number of nanomotors in the highest effective diffusivity region divided by the number of nanomotors in the lowest effective diffusivity region in that frame. Both regions were $1/10^{\text{th}}$ the channel width. Figure 56 depicts the channel regions used to measure chemotactic index. The minimum nanomotor effective diffusivity is on the right side of the channel (green region), and the maximum effective diffusivity is on the left side (red region).

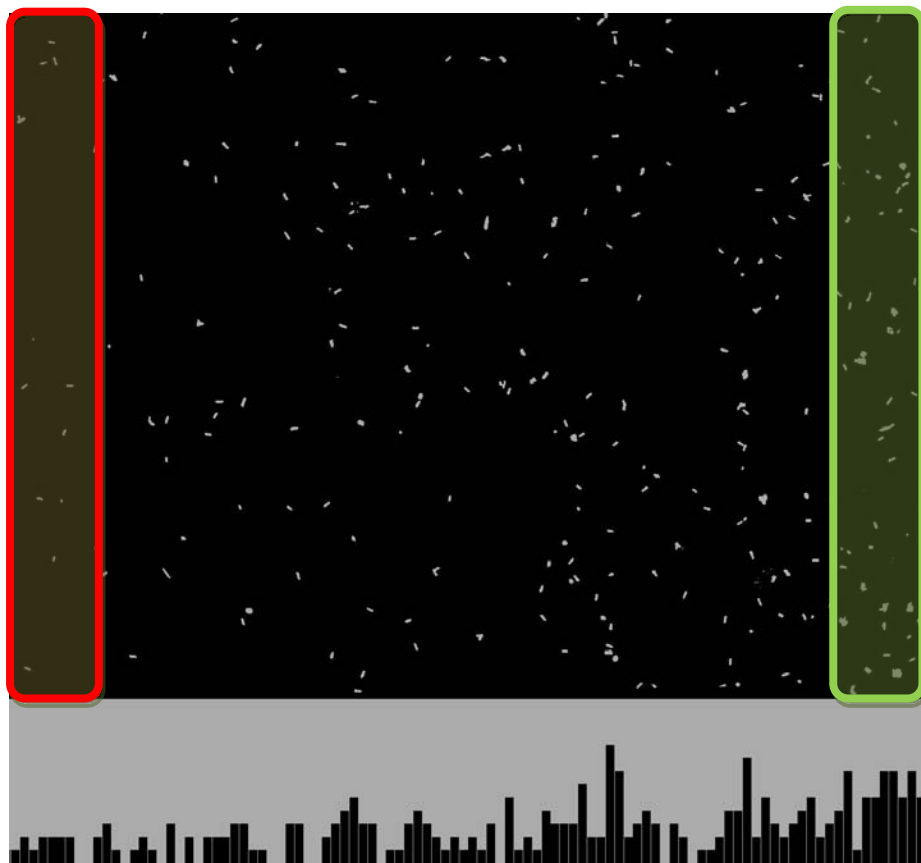


Figure 56: Channel regions used to measure chemotactic index. The minimum nanomotor effective diffusivity is on the right side of the channel (green region), and the maximum effective diffusivity is on the left side (red region).

5.3.4 Response Time

In many cases the experimental data is represented as the measured chemotactic index as a function of time as depicted in Figure 57. The response closely resembles a first-order transient response. Therefore, the data can be analyzed to determine temporal response by determining how long it takes the chemotactic index to reach 0.632 times the steady state chemotactic index. The steady state chemotaxis is measured as the average of the experimental chemotactic index for long times.

CI

t (s)

Figure 57: Chemotactic index measured as a function of time for simple bimetallic nanomotors subject to a gradient in chemical concentration that leads to a gradient in the motor's effective diffusivity.

5.3.5 Controls

When performing the experiments, a linear gradient is first established and verified using low concentration fluorescent dye (10 μ M Fluorescein). The

solution in the center channel is then flushed out with an aqueous solution containing the nanomotors. Once the nanomotor solution is added, the linear gradient must be reestablished. The simulations assume an established linear gradient in effective diffusivity throughout the experiment. For a valid comparison between the simulations and the experimental results, the time to reestablish the steady chemical concentration gradient must be very short relative to the response time of the nanomotors. This is verified pumping a very high concentration of fluorescein through the right channel (1mM), DI water through the left channel, waiting until the gradient in the center channel is established, then flushing the center channel with water and then waiting for the gradient to reestablish. Figure 58 shows the fluorescence intensity averaged along the axis of the center channel as a function of position across the width of the channel for several different times after the channel is flushed. The gradient recovery time is on the order of 60 seconds as shown in Figure 59. As shown in Figure 57, the time for the motors to reach a steady state response is about 500 seconds. Because the fluorescent dye has a lower diffusivity than both the hydrogen peroxide and the KCl salts used in the experiments, the time to reestablish the steady gradient in concentration after flushing the channel is expected to be even shorter than the 60 second observed for the Fluorescein. Therefore, the effects of an initially transient concentration gradient are considered negligible.

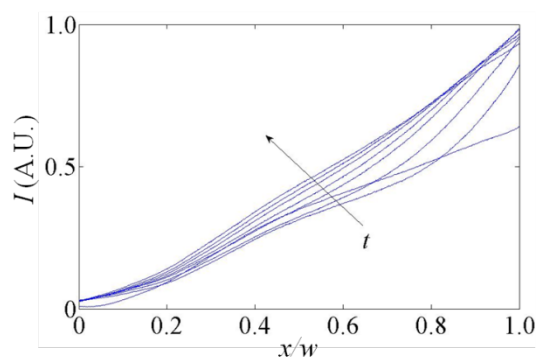


Figure 58: Vertically-averaged fluorescence intensity as function of horizontal position in the center channel.

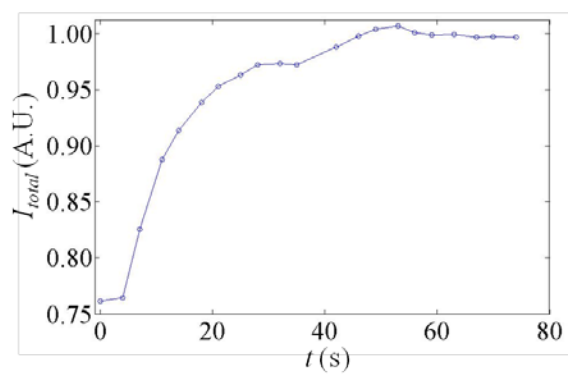


Figure 59: Vertically-averaged fluorescence intensity integrated horizontally across the width of the channel as a function of time.

Other considerations that must be made are the other possible causes of the accumulation observed in these experiments. These causes include either pressure driven flow due to an insufficient seal above or below the nitrocellulose membrane walls or a diffusiophoretic response to the chemical concentration gradient. Each structure used is initially tested to verify there are no leaks resulting in pressure driven flows, this is done by seeding the center channel with 500 nm red fluorescent polystyrene spheres (Duke Scientific Inc, Fremont, CA, USA). These fluorescent tracers are used to verify the absence of a drift velocity in any direction.

To address the possibility of diffusiophoresis due to the gradient in KCl concentration, the KCl salt gradient is established in the absence of H_2O_2 . The nanomotors are uniformly dispersed in the center channel subject to a KCl gradient. The initial distribution of motors and the resulting distribution after 33 minutes are shown in Figure 60 and Figure 61. In this case the distribution remains uniform; therefore the accumulation observed in the experiments cannot be the result of KCl diffusiophoresis.



Figure 60: Initial distribution of nanomotors subject to a linear gradient in KCl.

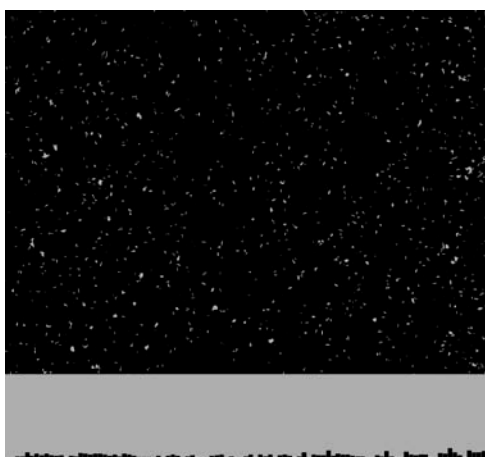


Figure 61: Distribution of nanomotors subject to a linear gradient in KCl for 33 minutes.

It is also necessary to verify the observed accumulation is not due to H_2O_2 diffusiophoresis. To verify this, nanorods composed of entirely gold and entirely platinum are placed in a H_2O_2 gradient. The average horizontal velocity component of 217 motors tracked for at least 50 seconds was $7.5 \times 10^{-4} \mu\text{m/s}$ from left to right. This would require 148 hours for nanomotors on the left side of the channel to move via diffusiophoresis to the right side of the channel. Clearly the accumulation on the right side of the channel is not due to H_2O_2 diffusiophoresis.

5.3.6 Results

First, an experiment was performed to demonstrate the ability to develop an accumulation of nanomotors on one side and then switch to the other side by switching the chemical concentration gradient. The results of this experiment are shown in Figure 62. Initially the H_2O_2 was flowing through the right channel and the KCl was flowing through the left channel. At 800 seconds the tubes were switched such that the H_2O_2 flowed through the left channel and the KCl through the right. This was switched again at 3100 seconds and back again at 4800 seconds. Figure 62 depicts the number of nanomotors as a function of position and time for this experiment. In Figure 62, the width of the channel is divided into 100 bins. The color corresponds to the average number of nanomotors in the bin over a period of 100 seconds.

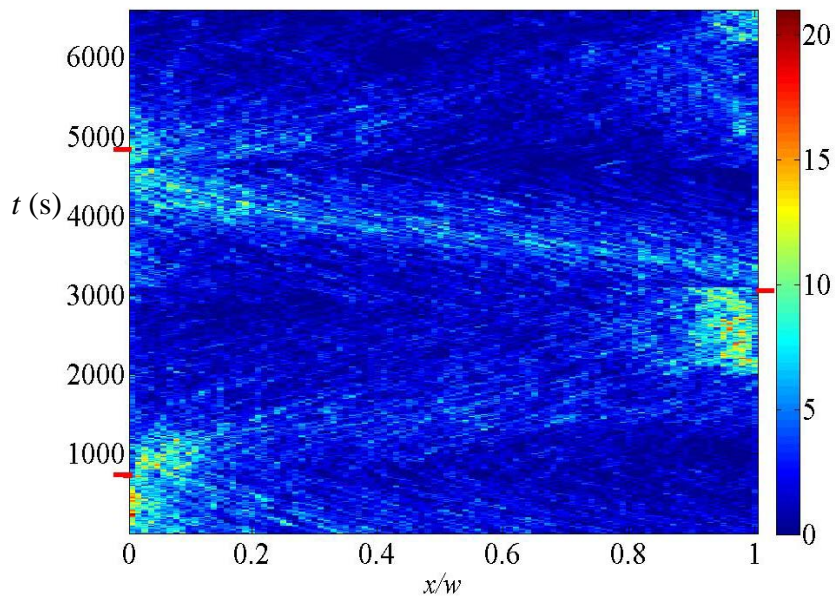


Figure 62: Histogram contour map of the number of nanomotors as a function of time and location across the width of the channel divided into 100 bins.

Next, the experimental responses of the nanomotors to several different gradients in effective diffusivity were compared to the Brownian Dynamics and computational PDE simulations (Figure 63 thru Figure 69). From day to day, there was a substantial variation in the nanomotor velocities as a function of H_2O_2 concentration. As a result it was not necessary to use different batches of nanomotors to perform a parameter variation study. In all of the following experiments, $1.5 \mu\text{m}$ long gold-platinum nanorods with equal $0.75 \mu\text{m}$ long segments were used.

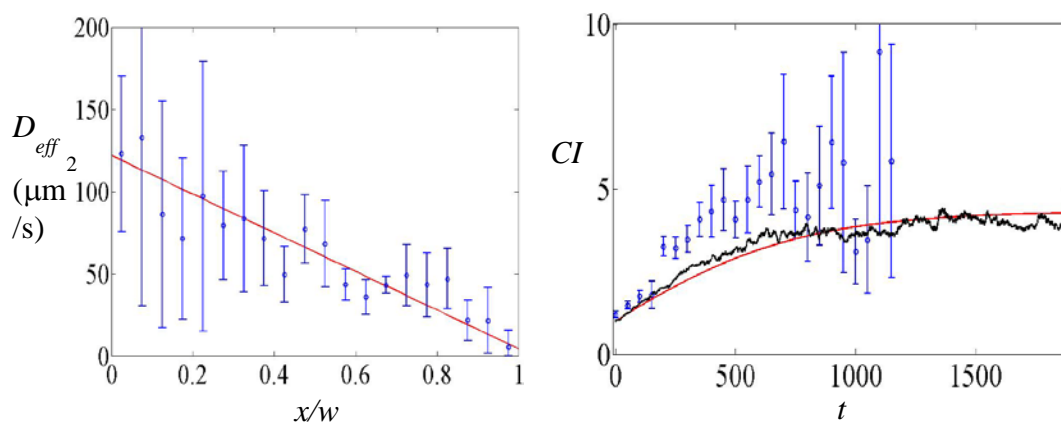


Figure 63: Case 1 results. Left: Effective diffusivity as a function of position across the width of the channel. Right: Chemotactic index as a function of time. Error bars correspond to one standard deviation of measurements. The blue corresponds to the experimental data. The red line corresponds to a least squares regression fit to the averages of the effective diffusivity data and the corresponding PDE results. The black curve is the result of the Brownian Dynamics simulation.

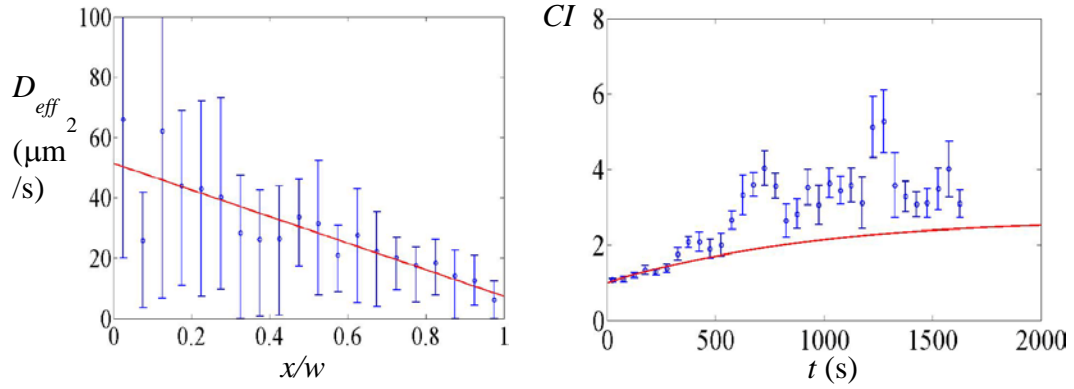


Figure 64: Case 2 results. Left: Effective diffusivity as a function of position across the width of the channel. Right: Chemotactic index as a function of time. Error bars correspond to one standard deviation of measurements. The blue corresponds to the experimental data. The red line corresponds to a least squares regression fit to the averages of the effective diffusivity data and the corresponding PDE results.

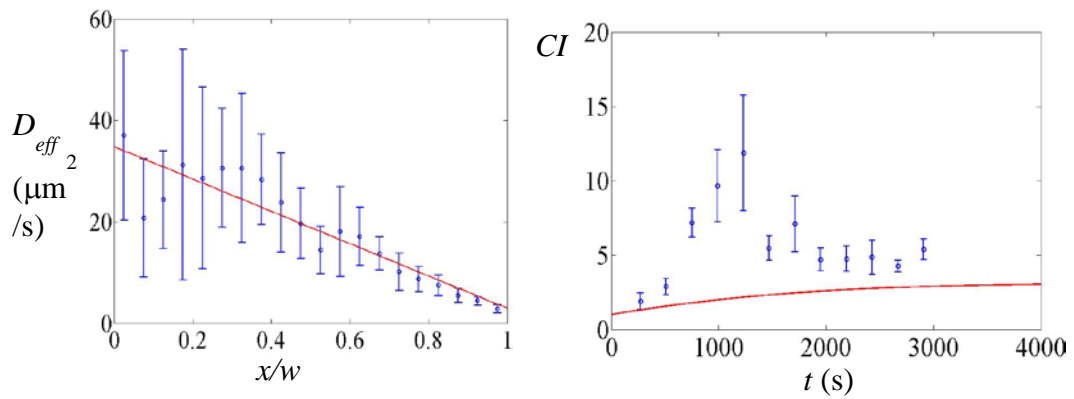


Figure 65: Case 3 results. Left: Effective diffusivity as a function of position across the width of the channel. Right: Chemotactic index as a function of time. Error bars correspond to one standard deviation of measurements. The blue corresponds to the experimental data. The red line corresponds to a least squares regression fit to the averages of the effective diffusivity data and the corresponding PDE results.

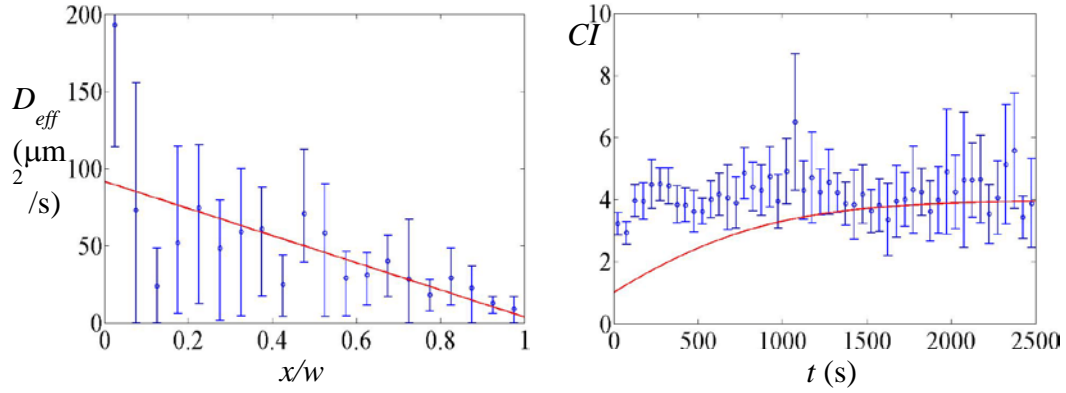


Figure 66: Case 4 results (data not available for early times). Left: Effective diffusivity as a function of position across the width of the channel. Right: Chemotactic index as a function of time. Error bars correspond to one standard deviation of measurements. The blue corresponds to the experimental data. The red line corresponds to a least squares regression fit to the averages of the effective diffusivity data and the corresponding PDE results.

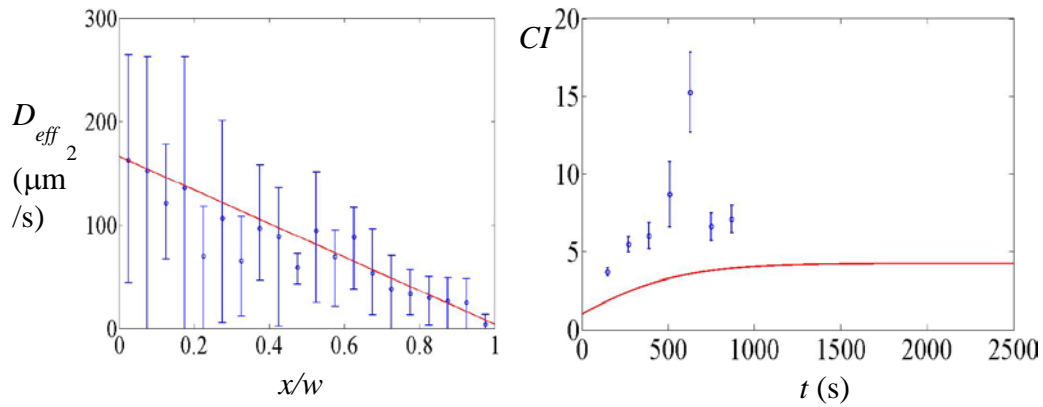


Figure 67: Case 5 results. Left: Effective diffusivity as a function of position across the width of the channel. Right: Chemotactic index as a function of time. Error bars correspond to one standard deviation of measurements. The blue corresponds to the experimental data. The red line corresponds to a least squares regression fit to the averages of the effective diffusivity data and the corresponding PDE results.

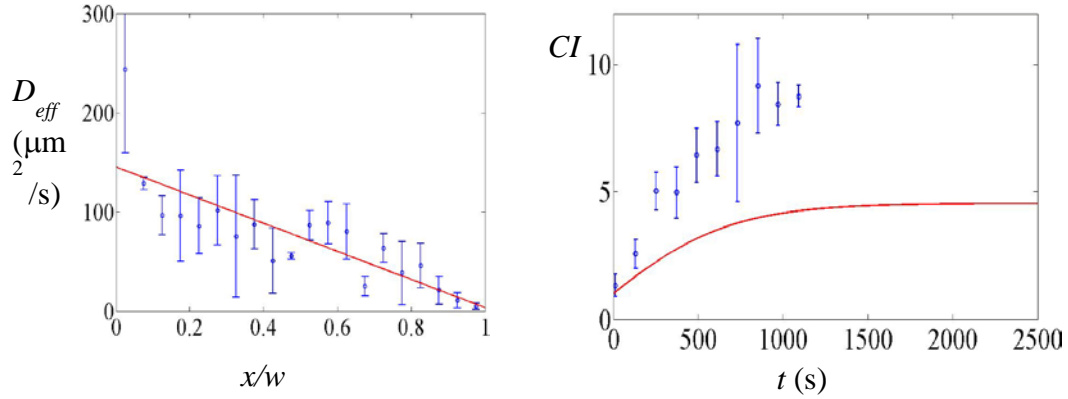


Figure 68: Case 6 results. Left: Effective diffusivity as a function of position across the width of the channel. Right: Chemotactic index as a function of time. Error bars correspond to one standard deviation of measurements. The blue corresponds to the experimental data. The red line corresponds to a least squares regression fit to the averages of the effective diffusivity data and the corresponding PDE results.

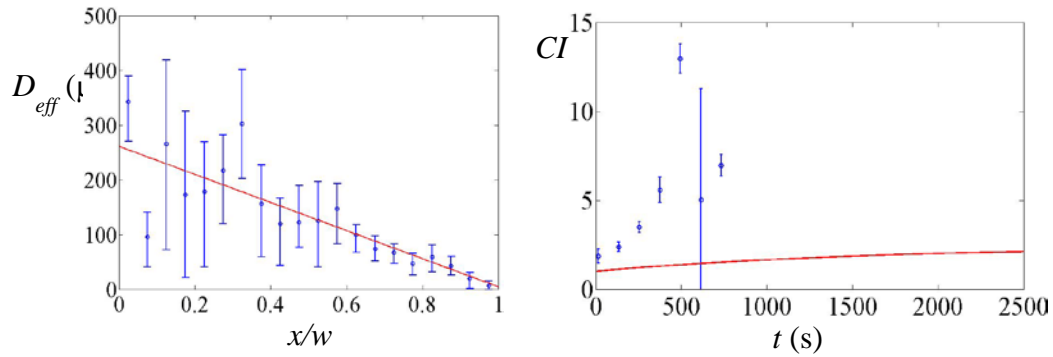


Figure 69: Case 7 results. Left: Effective diffusivity as a function of position across the width of the channel. Right: Chemotactic index as a function of time. Error bars correspond to one standard deviation of measurements. The blue corresponds to the experimental data. The red line corresponds to a least squares regression fit to the averages of the effective diffusivity data and the corresponding PDE results.

In each of these experiments, the nanomotors reach a steady-state chemotactic index higher than expected, faster than expected. The global behavior of the nanomotors is in qualitative agreement, but quantitatively amplified. The chemotactic index is arbitrarily defined as the ratio of the number of motors

within in $1/10^{\text{th}}$ of the channel width on the maximum effective side to the number of motors within $1/10^{\text{th}}$ of the channel width on the minimum effective diffusivity side. Therefore, it is important to verify that the overall profile is consistent between the experiment and the simulations, such that if the regions were increased or decreased in width, the same conclusions would be reached. Figure 70 depicts the steady state distribution predicted by the PDE model and BD simulation of the initial and steady state distributions of nanomotors along with experimental position distributions at $t = 0\text{s}$ and $t = 4000\text{s}$. The PDE model and BD simulation results in Figure 70 correspond to the red curve in Figure 65, while the experimental results correspond to the experimental data in Figure 65. Because of the limits on the concentration of nanomotors imposed by the oxygen production only around 300 nanomotors could be observed in one field of view. In order to get the clean position distribution presented in Figure 65, it was necessary to image the entire channel in segments. The distributions are composed of the positions of 2550 nanomotors.

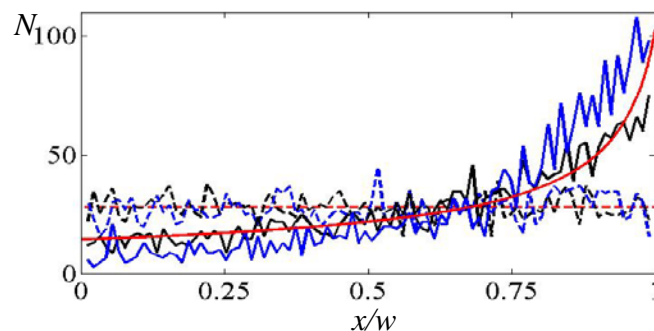


Figure 70: Experimental (blue), Brownian Dynamics simulation (black), and corresponding PDE simulation (red) steady-state nanomotor position distributions for 2550 nanomotors at $t = 0\text{ s}$ (dashed) and $t = 4000\text{ s}$ (solid).

In both the PDE and Brownian Dynamics simulations, the results are a function of the gradient in effective diffusivity and the minimum effective diffusivity. In the range of the experimental parameters, the steady state chemotactic index is more sensitive to the minimum effective diffusivity, and the temporal response is more sensitive to the gradient in effective diffusivity. Figure 71 and Figure 72 depict the steady state chemotactic index and the temporal response, respectively, both as a function of the gradient in effective diffusivity and the minimum effective diffusivity as determined using the PDE model. In both figures, the squares correspond to the least squares regression fit to the effective diffusivity as a function of position (chemokinetic response). The colors inside the squares correspond to the experimental values. These phase maps exhibit three distinct regions: (1) at low diffusivity gradients there is no chemokinesis and the motors are nearly uniform at all times; (2) when the effective diffusivity of the motors dips below the Brownian diffusivity $D_{\min} < D_b$ represents the case where physics of the problem have changed such that the particles aggregate or reach a sticky boundary; (3) the physical regime where chemokinesis occurs $D_{\min} > D_b$ and $dD/dx > 0$. The experiments are performed for a variety of effective diffusivity gradients dD/dx but all have a minimum effective diffusivity near D_b . By normalizing the effective diffusivity gradient by the minimum diffusivity the entire chemotactic index phase map onto a single line as shown in Figure 73.

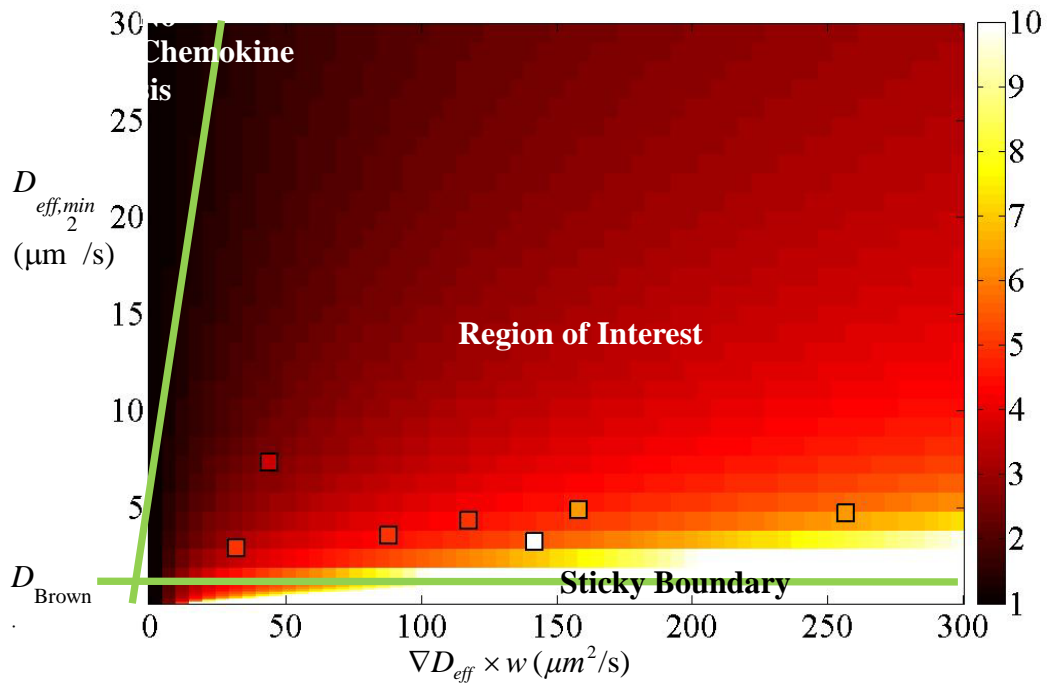


Figure 71: Steady state chemotactic index phase map. The colors correspond to the steady state chemotactic index predicted by the PDE model. The squares correspond to the least squares regression fit to the effective diffusivity as a function of position (chemokinetic response) for each experiment. The colors inside the squares correspond to the experimental steady state chemotactic indices.

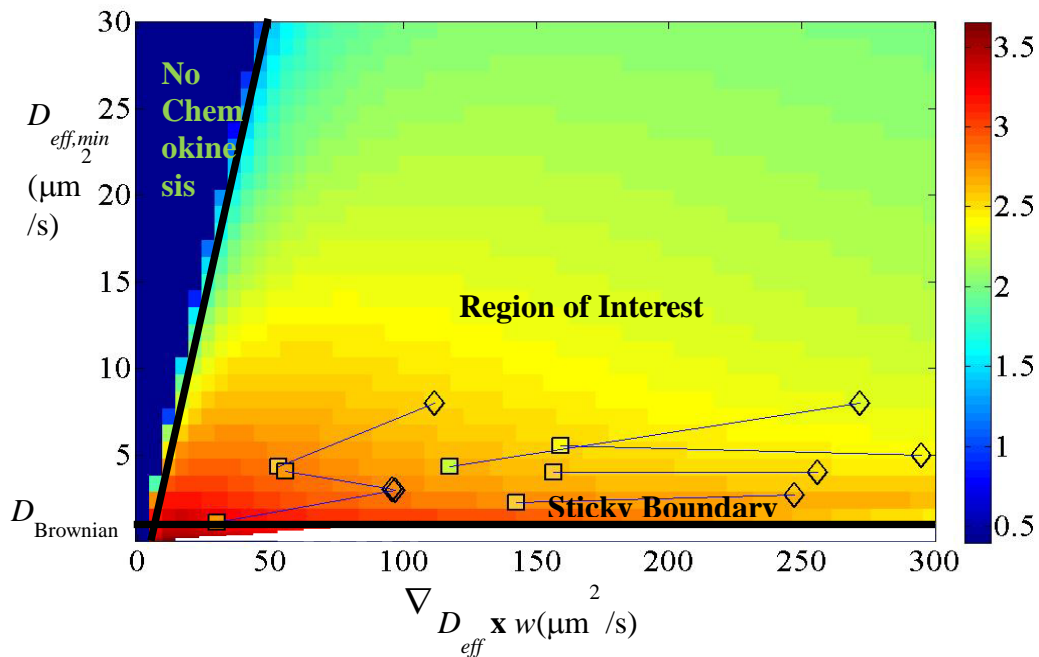


Figure 72: Response time phase map. The colors correspond to the $\text{LOG}_{10}(\text{response time})$ predicted by the PDE model. The squares correspond to the least squares regression fit to the effective diffusivity as a function of position (chemokinetic response) for each experiment. The colors inside the squares correspond to the experimental response times. The diamonds correspond to the location on the phase map that would result in the PDE model having the same response time and steady state chemotactic index as the experiment.

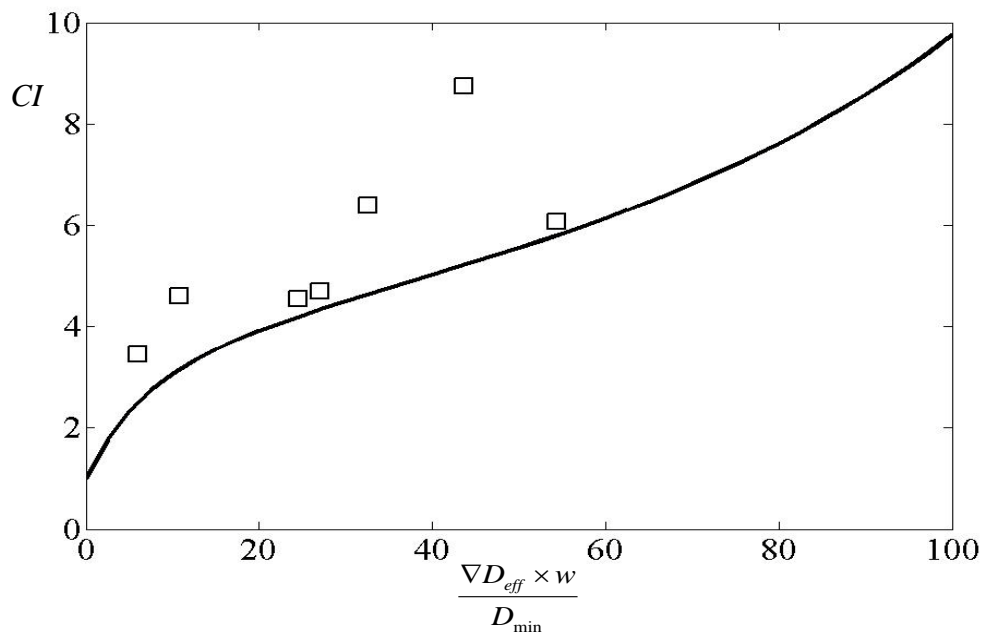


Figure 73: Steady state chemotactic index vs. $\text{grad}(D_{eff}) \times w / D_{eff,min}$. Experiments (squares) vs. PDE model (line).

From each of these experiments, it is clear the nanomotors undergo chemokinesis. The experiments and conservation model show that the CI index increases with increasing diffusivity gradient. This is expected because stronger gradients results in greater net drift of high diffusivity particles into regions with low diffusivities. However, in each case the steady-state chemotactic index measured in the experiments is higher than predicted by the models. Figure 63 thru Figure 69 suggest a higher value of α is necessary to obtain agreement between the PDE model and the experiments. A higher value of α would imply a decrease in the average rotational diffusivity of the motors moving from left to right across the width of the channel. Such a decrease would stem from either an increase in rotational diffusivity with an increase in [H₂O₂] or a decrease in rotational diffusivity with an increase in [salt], or both. As discussed in section 3.1, a value of α greater than 0.5 that is not unity is an approximation of a neglected term in the governing equation. Alternatively, the slope of the measured fit line may be lowered by a combination of broken nanomotors and nanomotor interactions. At early times, while the distribution across the width of the channel is nearly uniform, the gradient in effective diffusivity is lower than it would be at steady-state because at steady-state there is an accumulation of motors in the low effective diffusivity region increasing the frequency of motor interaction and decreasing the effective diffusivity in that region. At steady-state, the measured gradient in the average effective diffusivity is also lowered by the increase in percent of the motors that are dysfunctional in the high effective diffusivity region.

CHAPTER 6

SUMMARY

This work provides an analysis of the global behavior of bimetallic micro and nanomotors subject to gradients in chemokinetic compounds, as well a method of passively guiding these motors to a particular destination utilizing such chemical concentration gradients. A Brownian dynamics model is presented and used to quantitatively simulate the behavior of bimetallic motors subject to various concentration gradients. A governing PDE is also presented as a rapid means of predicting the global behavior of purely chemokinetic objects. It was determined that the Fokker-Planck law of diffusion modified by the Ito-Stratonovich convention with a coefficient of $2/3$ can be used to match the results of the Brownian dynamics model with a linear gradient in effective diffusivity. This work also includes the fabrication and characterization of several different micro and nanomotors with varying chemokinetic properties, and this work presents a novel technique for rapid fabrication of bimetallic micromotors that does not require the hazardous chemicals and expensive equipment necessary for bimetallic motors fabricated to date. These synthetic motors are used to confirm the chemokinesis predicted by the Brownian dynamics and PDE simulations, utilizing an ideal chemotactic assay, in which there is a steady spatial gradient in the concentration of a chemical that induces a chemokinetic response from bimetallic micro and nanomotors. This work is the first to demonstrate that synthetic nanomotors can mimic biological systems that utilize chemokinesis as a passive guidance technique for reaching their destination.

REFERENCES

- Ahmed, T., and R. Stocker. "Experimental Verification of the Behavioral Foundation of Bacterial Transport Parameters Using Microfluidics." Biophysical Journal 95.9 (2008): 4481-93.
- Balasubramanian, S., et al. "Thermal Modulation of Nanomotor Movement." Small 5.13 (2009): 1569-74.
- Bloom, George S. "Kinesin-1 Discovery". 1996. Kinesin. Eds. Liz Greene and Steve Henikoff. (6/18/2008). 11/14/2010 2010. <<http://www.cellbio.duke.edu/kinesin/Discovery.html>>.
- Boyden, Stephen. "The Chemotactic Effect of Antibody and Antigen on Polymorphonuclear Leucocytes." The Journal of Experimental Medicine 115 (1962): 453.
- Brown, Douglas A., and Howard C. Berg. "Temporal Stimulation of Chemotaxis in Escherichia Coli." Proceedings of the National Academy of Sciences of the United States of America.71 (1974): 1388-92.
- Brown, S., et al. "Chemokinesis in Rhodospirillum rubrum Is the Result of a Long-Term Increase in the Rate of Flagellar Rotation." Biochimica Et Biophysica Acta 1141.2-3 (1993): 309-12.
- Burdick, J., et al. "Synthetic Nanomotors in Microchannel Networks: Directional Microchip Motion and Controlled Manipulation of Cargo." Journal of the American Chemical Society 130.26 (2008): 8164-+.
- Calvo-Marzal, P., et al. "Electrochemically-Triggered Motion of Catalytic Nanomotors." Chemical Communications.30 (2009): 4509-11.
- Catchmark, J. M., S. Subramanian, and A. Sen. "Directed Rotational Motion of Microscale Objects Using Interfacial Tension Gradients Continually Generated Via Catalytic Reactions." Small 1.2 (2005): 202-06.
- Crank, John. The Mathematics of Diffusion. 2nd ed. Oxford: Clarendon Press, 1975.
- Diao, J. P., et al. "A Three-Channel Microfluidic Device for Generating Static Linear Gradients and Its Application to the Quantitative Analysis of Bacterial Chemotaxis." Lab on a Chip 6.3 (2006): 381-88.
- Doi, M., and S. F. Edwards. The Theory of Polymer Dynamics. Oxford University Press, USA, 1988.
- Dunn, G.A. "Chemotaxis as a Form of Directed Cell Behaviour: Some Theoretical Considerations. ." Biology of the Chemotactic Response. Eds. P. C. Wilkinson and J.M. Lackie. Cambridge: Cambridge University Press, 1981. 1-26.
- Engelmann, Theodor Wilhelm. "Neue Methoden Zur Untersuchung Der Sauerstoffausscheidung Pflanzlicher Und Tierischer Organismen." Pflüger's Archiv Gesamte Physiol 25 (1881): 285-92.
- Figliola, R. S., and Donald E. Beasley. Theory and Design for Mechanical Measurements. 4th ed. Hoboken, NJ: John Wiley, 2006.
- Fournier-Bidoz, S., et al. "Synthetic Self-Propelled Nanomotors." Chemical Communications.4 (2005): 441-43.
- Gibbons, I. R. "Proteins Associated with Movement in Cilia." Journal of Cell Biology 27.2 (1965): A33-&.
- Haessler, U., et al. "An Agarose-Based Microfluidic Platform with a Gradient Buffer for

- 3d Chemotaxis Studies." Biomedical Microdevices 11.4 (2009): 827-35.
- Hiratsuka, Y., et al. "A Microrotary Motor Powered by Bacteria." Proceedings of the National Academy of Sciences of the United States of America 103.37 (2006): 13618-23.
- Hong, Y., et al. "Chemotaxis of Nonbiological Colloidal Rods." Physical Review Letters 99.17 (2007).
- Howse, J. R., et al. "Self-Motile Colloidal Particles: From Directed Propulsion to Random Walk." Physical Review Letters 99.4 (2007).
- Ibele, M., T. E. Mallouk, and A. Sen. "Schooling Behavior of Light-Powered Autonomous Micromotors in Water." Angewandte Chemie-International Edition 48.18 (2009): 3308-12.
- Jiang, P., and M. J. McFarland. "Large-Scale Fabrication of Wafer-Size Colloidal Crystals, Macroporous Polymers and Nanocomposites by Spin-Coating." Journal of the American Chemical Society 126.42 (2004): 13778-86.
- Kagan, D., et al. "Chemical Sensing Based on Catalytic Nanomotors: Motion-Based Detection of Trace Silver." Journal of the American Chemical Society 131.34 (2009): 12082-+.
- Laocharoensuk, R., J. Burdick, and J. Wang. "Carbon-Nanotube-Induced Acceleration of Catalytic Nanomotors." Acs Nano 2.5 (2008): 1069-75.
- Leber, T. "Über Die Entstehung Der Entzündung Und Die Wirkung Der Entzündungerregenden Schädlichkeiten " Fortschritt. Med. 4 (1888): 460.
- Lin, F., and E. C. Butcher. "T Cell Chemotaxis in a Simple Microfluidic Device." Lab on a Chip 6.11 (2006): 1462-69.
- Mello, B. A., and Y. H. Tu. "Effects of Adaptation in Maintaining High Sensitivity over a Wide Range of Backgrounds for Escherichia Coli Chemotaxis." Biophysical Journal 92.7 (2007): 2329-37.
- Meyhofer, E., and J. Howard. "The Force Generated by a Single Kinesin Molecule against an Elastic Load." Proceedings of the National Academy of Sciences of the United States of America 92.2 (1995): 574-78.
- Moore, J. W. "Table of Some Standard Free Energies of Formation". Madison, 2010. Chemical Education Digital Library. Ed. J. W. Moore. UW-Madison. April 12 2011. <<http://chemed.chem.wisc.edu/chempaths/Table-of-Some-Standard-Free-Energies-of-Formation-1185.html>>.
- Moran, J. L., and J. D. Posner. "Electrokinetic Locomotion by Reaction Induced Charge Auto-Electrophoresis." Journal of Fluid Mechanics In Press (2011).
- Moran, J. L., P. M. Wheat, and J. D. Posner. "Locomotion of Electrocatalytic Nanomotors Due to Reaction Induced Charge Auto-Electrophoresis." arXiv:1001.5462v2 (2010).
- . "Locomotion of Electrocatalytic Nanomotors Due to Reaction Induced Charge Auto-Electrophoresis." Physical Review E Submitted (2010).
- . "Locomotion of Electrocatalytic Nanomotors Due to Reaction Induced Charge Autoelectrophoresis." Physical Review E 81.6 (2010).
- Palacci, J., et al. "Colloidal Motility and Pattern Formation under Rectified Diffusiophoresis." Physical Review Letters 104.13 (2010).
- Paschal, B. M., H. S. Shpetner, and R. B. Vallee. "Map 1c Is a Microtubule-Activated Atpase Which Translocates Microtubules Invitro and Has Dynein-Like

- Properties." Journal of Cell Biology 105.3 (1987): 1273-82.
- Paunov, V. N., and O. J. Cayre. "Supraparticles And "Janus" Particles Fabricated by Replication of Particle Monolayers at Liquid Surfaces Using a Gel Trapping Technique." Advanced Materials 16.9-10 (2004): 788-+.
- Paxton, W. F., et al. "Catalytically Induced Electrokinetics for Motors and Micropumps." Journal of the American Chemical Society 128.46 (2006): 14881-88.
- . "Catalytic Nanomotors: Autonomous Movement of Striped Nanorods." Journal of the American Chemical Society 126.41 (2004): 13424-31.
- . "Catalytic Motors and Pumps on the Nano- and Microscale." Abstracts of Papers of the American Chemical Society 231 (2006): 29-ANYL.
- Paxton, W. F., A. Sen, and T. E. Mallouk. "Motility of Catalytic Nanoparticles through Self-Generated Forces." Chemistry-a European Journal 11.22 (2005): 6462-70.
- Pfeffer, W. "Über Chemotaktische Bewegungen Von Bacterie, Flagellaten Und Volvocineen." Untersuch. aus d. Botan.Institut Tübingen.2 (1888): 582-661.
- Prevo, B. G., and O. D. Velev. "Controlled, Rapid Deposition of Structured Coatings from Micro- and Nanoparticle Suspensions." Langmuir 20.6 (2004): 2099-107.
- Ralt, D., et al. "Chemotaxis and Chemokinesis of Human Spermatozoa to Follicular Factors." Biology of Reproduction 50.4 (1994): 774-85.
- Richards, G. R., et al. "Quantitative Assays of Chemotaxis and Chemokinesis for Human Neural Cells." Assay and Drug Development Technologies 2.5 (2004): 465-72.
- Rivero, M. A., et al. "Transport Models for Chemotactic Cell-Populations Based on Individual Cell Behavior." Chemical Engineering Science 44.12 (1989): 2881-97.
- Rose, K. A., et al. "Rotational Electrophoresis of Striped Metallic Microrods." Physical Review E 75.1 (2007).
- Rose, Klint A., et al. "Rotational Electrophoresis of Striped Metallic Microrods." Physical Review E 75.1 (2007): 011503.
- Saadi, W., et al. "A Parallel-Gradient Microfluidic Chamber for Quantitative Analysis of Breast Cancer Cell Chemotaxis." Biomedical Microdevices 8.2 (2006): 109-18.
- Seymour, J.R. , et al. "A Microfluidic Chemotaxis Assay to Study Microbial Behavior in Diffusing Nutrient Patches." Limnology and Oceanography: Methods (2008): 477-88.
- Soong, R. K., et al. "Powering an Inorganic Nanodevice with a Biomolecular Motor." Science 290.5496 (2000): 1555-58.
- Sourjik, V., and H. C. Berg. "Receptor Sensitivity in Bacterial Chemotaxis." Proceedings of the National Academy of Sciences of the United States of America 99.1 (2002): 123-27.
- Sundararajan, S., et al. "Catalytic Motors for Transport of Colloidal Cargo." Nano Letters 8.5 (2008): 1271-76.
- Takei, H., and N. Shimizu. "Gradient Sensitive Microscopic Probes Prepared by Gold Evaporation and Chemisorption on Latex Spheres." Langmuir 13.7 (1997): 1865-68.
- Tien, C. L., and Cunnignt.Gr. "Recent Advances in High-Performance Cryogenic Thermal Insulation." Cryogenics 12.6 (1972): 419-&.
- van den Heuvel, M. G. L., and C. Dekker. "Motor Proteins at Work for Nanotechnology." Science 317.5836 (2007): 333-36.
- Wheat, P. M., et al. "Rapid Fabrication of Bimetallic Spherical Motors." Langmuir 26.16:

13052-55.

---. "Rapid Fabrication of Bimetallic Spherical Motors." Langmuir 26.16 (2010): 13052-55.

Wilkinson, P. C. "Assays of Leukocyte Locomotion and Chemotaxis." Journal of Immunological Methods 216.1-2 (1998): 139-53.

Zigmond, S. H., and J. G. Hirsch. "Leukocyte Locomotion and Chemotaxis - New Methods for Evaluation and Demonstration of a Cell-Derived Chemotactic Factor." Journal of Experimental Medicine 137.2 (1973): 387-410.

APPENDIX A
MATLAB SIMULATION OPTIONS

APPENDIX A

MATLAB SIMULATION OPTIONS

Variable Name	Values	Description
FIXED_GRADIENT	0 or 1	A value of '1' results in a constant fuel concentration profile. A value of '0' results in a diffusing concentration profile that takes into account the diffusivity of the fuel.
INHIBITOR	0 or 1	A value of '1' designates the "fuel" to be a chemotactic inhibitor such that a maximum in concentration corresponds to a minimum in nanomotor velocity, whereas a minimum in fuel concentration results in a maximum in nanomotor velocity. A value of '0' assigns the reverse relationship between fuel concentration and nanomotor velocity.
ANGULAR_INHIBIT OR	0 or 1	A value of '1' means higher fuel concentrations result in lower angular velocities, and a value of '0' assigns the reverse relationship.
Distributions	1 or 2	Versions of this code have been used to simulate the influence of two distinct fuel distributions. For the purposes of predicting

		chemotactic responses, a majority of the work utilized only one fuel 'source'.
Arrows*	0 or 1	<p>A value of '1' will cause directional arrows to be depicted in the movie created by this code. The arrows point in the direction in which the nanomotor is oriented, with a magnitude proportional to the chemotactic velocity. A value of '0' will omit the arrows allowing for shorter processing times.</p> <p>*Arrows is an option that requires the code to be able to access the function Arrow which is not in the standard Matlab toolbox.</p>
Rods	0 or 1	<p>A value of '1' depicts the nanomotors as nanorods that are half gold and half black and travel in the direction of the black end to represent the platinum end in the case of an Au-Pt nanorod. A value of '0' depicts the nanomotors as circles.</p>
Tracers	0 or 1	<p>A value of '1' results in a blue lines depicting the paths of each nanomotor during the movie. A value of '0' omits the blue trace line from the video.</p>

FREEZE_FRAMES	0 or 1	A value of '1' results in periodic frames of the movie being saved as still images. A value of '0' results in no still images being saved automatically.
right	0 or 1	A value of '1' results in a containing wall on the right side of the analysis region. The wall is infinite in the y-direction and impenetrable. A value of '0' results in no containing boundary on the right hand side of the analysis region, such that the region is semi-infinite in the positive x-direction.
left	0 or 1	A value of '1' results in a containing wall on the left side of the analysis region. The wall is infinite in the y-direction and impenetrable. A value of '0' results in no containing boundary on the left hand side of the analysis region, such that the region is semi-infinite in the negative x-direction.
top	0 or 1	A value of '1' results in a containing wall on the top of the analysis region. The wall is infinite in the x-direction and impenetrable. A value of '0' results in no containing

		boundary on the top of the analysis region, such that the region is semi-infinite in the positive y-direction.
Bottom	0 or 1	A value of '1' results in a containing wall on the bottom of the analysis region. The wall is infinite in the x-direction and impenetrable. A value of '0' results in no containing boundary on the bottom of the analysis region, such that the region is semi-infinite in the negative y-direction.
reflect_orientation	0 or 1	A value of '1' causes the nanomotors to reflect their orientation upon interacting with a containing wall. For example, if a nanomotor is facing the positive x-direction and encounters a wall during a time step, it will be facing the negative x-direction at the end of that time step. Alternatively, a value of '0' causes the nanomotor to retain its orientation during a wall interaction such that the orientation is only altered as prescribed by the angular velocity during a time step in which a wall is encountered.

stickywall	0 or 1	A value of '1' results in the existence of a left wall that is sticky, such that nanomotors that interact with the sticky wall will permanently adsorb to the wall. This is designed to simulate some of the work done in the literature, in which nanomotors became stuck to a surface upon contact. A value of '0' yields no sticky wall, all wall interactions are reflective.
left_sticywall_position	Value in meters	Enter the distance from the origin along the x-axis in meters, at which you want the left sticky wall to be placed.

Table A.1: Brownian dynamics simulation options.

Variable Name	Values	(units) Description
Temp	293.15	(K) Temperature used to calculate theoretical diffusivity values.
kB	1.381e-23	(m ² kg/s ² K) Boltzmann Constant.
viscosity	10 ⁻³	(kg/m s) Dynamic viscosity of water.
radius	2e-6	(m) Approximate radius of the nanomotors.
Vtheta	100	(°/s) This value is tweaked to get the Brownian rotational diffusivity to match the approximate analytical value determined using the Stokes-Einstein equation for rotational diffusivity, $D_{rot} = kB T / (6\pi\mu r^3)$. A value of 100 results in $D_{rot} = 0.1 \text{ rad}^2/\text{s}$ when $\Delta t = 0.1 \text{ s}$.
Vt	10e-6	(m/s) This value is tweaked to get the Brownian translational diffusivity to match the approximate analytical value determined using the Stokes-Einstein equation for translational diffusivity, $D_{trans} = kB T / (6\pi\mu r)$. A value of 10 $\mu\text{m}/\text{s}$ results in $D_{trans} = 4.1\text{e-}12 \text{ m}^2/\text{s}$ when $dt = 0.1 \text{ s}$.
Dattractant	1.3e-9	(m ² /s) This value establishes the diffusivity of the fuel. The value of 1.3e-9 m ² /s corresponds to the diffusivity of hydrogen peroxide

		(www.h2o2.com).
Umax	20e-6	(m/s) This value is the translational velocity of the nanomotor due to chemotaxis at the maximum fuel concentration. The code assumes a linear relationship between fuel concentration and chemotactic velocity with a zero chemotactic velocity associated with no fuel.
VthetaMAX	5000	(°/s) This value establishes the maximum possible chemotactic rotational velocity corresponding to the highest fuel concentration. There is a linear relationship between fuel concentration and the chemotactic rotational velocity with a zero chemotactic rotational velocity at locations where fuel is absent.
SIGMA_d	6e-6	(m) This value is the standard deviation of both the fuel distribution in a stationary gradient simulation and the standard deviation used in chemotactic index calculations.
M	10,000	() This value is the number of nanomotors accounted for in the simulation.
frameCap	50	() This value is the number of frames used to make the movie (it must be less than or equal to the number of time steps).
N	50	() This value is the number of time steps.

dt	0.1	(s) This is duration of each time step, such that the total duration of the simulation is $N \cdot dt$.
W	100e-6	(m) This value is the width of the region under consideration. This value effectively establishes the location along the x-axis of the right wall, if one is being simulated.
Wi	100e-6	(m) This value is the width of the initial nanomotor distribution.
Wip	0e-6	(m) This value establishes the distance along the x-axis from the origin to the left edge of the initial nanomotor distribution.
H	100e-6	(m) This value is the height of the region under consideration. This value effectively establishes the location along the y-axis of the top wall, if one is being simulated.
Hi	100e-6	(m) This value is the height of the initial nanomotor distribution.
Hip	0e-6	(m) This value establishes the distance along the y-axis from the origin to the bottom edge of the initial nanomotor distribution.
LcX	50e-6	(m) This value corresponds to the distance from the origin along the x-axis to the center of the fuel distribution.
h_tophat	20e-6	(m) This value is the halfwidth of the high

		concentration portion of the initial top hat fuel distribution.
baseV	0	(m/s) This value establishes a baseline axial velocity that is present regardless of fuel concentration. This value is set to zero except when simulating hypothetical situations as the axial velocity of the nanomotors not due to Brownian motion is zero in the absence of hydrogen peroxide.

Table A.2: Brownian dynamics parameters.

APPENDIX B

BROWNIAN DYNAMICS CODE

APPENDIX B

BROWNIAN DYNAMICS CODE

Initial Conditions. Randomly assign an initial orientation, position, and speed to each nanomotor. Such that the initial distribution resembles a drop of nanomotors introduced to a specified location relative to the fuel distribution.

Initial translational speeds (due to Brownian motion):

V_x is given a random value between 0 and V_T .

V_y is given a random value between 0 and $\sqrt{V_T^2 - V_x^2}$ such that the resulting velocity $V = \sqrt{V_x^2 + V_y^2}$ is between 0 and V_T .

Initial Positions and orientations:

The x-position for each nanomotor is assigned at random between the prescribed horizontal boundaries for the initial distribution (i.e. between W_p and $W_p + W_i$).

Similarly, the y-position for each nanomotor is assigned at random between the prescribed vertical boundaries for the initial distribution (i.e. between H_p and $H_p + H_i$).

The orientation of the nanomotor (as defined by the direction of the “leading” end, which is the platinum end in the case of the Au-Pt nanomotors) is assigned a random angle between 0° and 360° as measured counter-clockwise from the x-axis.

Initial angular velocity:

The angular velocity is given a maximum random component (V_θ) to account for Brownian rotation.

The fuel induced angular velocity component (chemotactic angular velocity, $V_{\theta c}$)

is determined from the concentration of the fuel at the position of the nanomotor, as determined above, for $t = 0$. Once the local concentration is obtained using the subfunction **concentration_c**, the chemotactic angular velocity is determined using either the subfunction **ROTATIONAL_FUNCTION** if the chemical gradient is fixed (no fuel diffusion) or the subfunction **chemotactic_velocity** if there is a transient fuel gradient (i.e. diffusion is accounted for).

In this case, the overall angular velocity is assigned a random value between positive ($V_{\theta} + V_{\theta c}$) and negative ($V_{\theta} - V_{\theta c}$). Effectively, this makes the rotational diffusion a function of fuel concentration.

TIME > 0. For each nanomotor, a for loop performs the following at each new time throughout the duration of the simulation:

New translational Brownian velocities (V_x and V_y) are assigned for the current time.

The new chemotactic velocity is approximated for the time interval between the previous time and the current time.

First, V_c is estimated based on the concentration of the fuel at the previous location using the subfunction(s):

concentration_c and **VELOCITY_FUNCTION** in the case of a fixed gradient.
chemotactic_velocity in the case of a diffusing gradient.

Then V_{cx} and V_{cy} are assigned an approximate value for the entire interval using the subfunction **Approx_Vc**, which uses the average of the V_c for the previous position (V_{c1}) and the chemotactic velocity (V_{c2}) calculated for the position the nanomotor would move to at a speed of V_{c1} over Δt .

The total axial velocity (V_a) over the time step is determined by adding the base directional velocity components ($V_{base,x}$ and $V_{base,y}$) to the respective chemotactic velocity components (V_{cx} and V_{cy}).

The new position of each nanomotor is determined by adding the directional velocity components to the Brownian velocity components, and multiplying them by the time interval and then adding the result to the previous position, i.e. $x_{new} = (V_x + V_{ax}) \Delta t + x_{old}$, and $y_{new} = (V_y + V_{ay}) \Delta t + y_{old}$.

Similarly, the new orientation of the nanomotor is determined by multiplying the previous rotational velocity by the time interval and adding the result to the previous angle.

The new rotational velocity is determined at the new location the same way as the initial angular velocity.

Accounting for walls.

If a nanomotor's new position is outside a containing wall, the position is reflected about the wall as if it were a mirror. For example, if a nanomotor's new x-position is 10 microns to the right of the right wall, its final position will be 10 microns to the left of that wall at the same y-position.

If the option 'reflect_orientation' is set to '1', then the orientation of the nanomotor will be mirrored about the traversed wall (right wall in the above example) as well. Otherwise, the orientation of the nanomotor will be the same as it was before the position was reflected.

At the end of the loop the new values are redefined as the old values for the next iteration.

The mean displacement is calculated by determining the difference between the new position and the original position, dividing that by the total number of time steps, and adding it to the mean displacement value from the previous iteration.

Similarly, the mean angular displacement is calculated by determining the difference between the new orientation and the original orientation, dividing that by the total number of time steps and adding the result to the mean angular displacement value from the previous iteration.

At the end of every time step, a video frame is captured and the following values are calculated:

The mean squared displacement for each time step is determined by squaring the mean displacement after the loop has accounted for the displacements of every nanomotor.

Similarly, the mean squared angular displacement is determined by squaring the mean angular displacement. NOTE: The mean angular displacement tracks successive rotations by continuing to count the degrees rotated beyond 360° . For example, if the rod continues to move clockwise and goes -370° , the angular displacement is -370° and not 10° .

The chemotactic index is then obtained using the subfunction **chemotactic_index**. An example of a video frame captured is shown in Figure 42.

Output. At the end of the code, an array containing the chemotactic index for each time step is written to a .mat file.

Subfunctions. The following codes are the subfunctions called on by this code.

The subfunction **chemotactic_index** determines the ratio of nanomotors within

two standard deviations of the center of the original fuel concentration profile to nanomotors within two standard deviations of either side of the container.

The subfunction **VthetaC** relates the maximum chemotactic rotational velocity to the local concentration.

The subfunction **VELOCITY_FUNCTION** relates the chemotactic translational velocity to the local concentration.

The subfunctions **tophat** and **tophat_master** provide the Green's function solution for a diffusing species with an initial distribution shape resembling the profile of a top hat. The fuel concentration at every location can be determined by solving the diffusion equation,

$$\frac{\partial c}{\partial t} = D\nabla^2 c,$$

where c is the concentration of species and D is the diffusion coefficient. The initial concentration profile is a top hat, such that the resulting nondimensionalized fuel concentration equation is given as,(Crank 1975)

$$c = \frac{c_0}{2} \sum_{n=0}^{\infty} \left[\operatorname{erf} \left(\frac{h - \left(x + (-1)^n \left((2n+1) \frac{w}{2} \right) \right)}{\sqrt{2}\delta} \right) + \operatorname{erf} \left(\frac{h + \left(x + (-1)^n \left((2n+1) \frac{w}{2} \right) \right)}{\sqrt{2}\delta} \right) \right],$$

where w is the transverse width of the channel, h is the width of the top hat concentration for the fuel, n is the summation index for the wall reflections, y is the transverse coordinate, c_0 is the initial fuel concentration, and \square is the characteristic diffusion length scale $\delta = \sqrt{2Dt}$ for the fuel.

The subfunction **concentration_c** uses the subfunction **tophat** to establish a fixed

concentration gradient, which is typically partially diffused.

The subfunction **Approx_Vc** uses the average of the V_c for the previous position (V_{c1}) and the chemotactic velocity (V_{c2}) calculated for the position the nanomotor would move to at a speed of V_{c1} over Δt to approximate the chemotactic velocity over the time interval.

The subfunction **chemotactic_velocity** determines the chemotactic velocity in the case of a diffusing concentration gradient. This is done using the concentration for the location of the nanomotor and the subfunctions **tophat** and **tophat_master**.

The Code

```
function [CI,NNNN,XXXX] =
Transient_chemotaxis(INHIBITOR,ANGULAR_INHIBITOR,Umax,Umin,DrotMAX,pfname)
    %%% r is a matrix with 10 columns and a row for each individual particle.
    %%% r(i,1) = TIME;
    %%% r(i,2) = PARTICLE (IDENTIFICATION NUMBER)
    %%% r(i,3) = X POSITION
    %%% r(i,4) = Y POSITION
    %%% r(i,5) = ORIENTATION IN DEGREES (measured counter clockwise from the x-axis.
    %%% r(i,6) = ROTATIONAL VELOCITY (degrees/second)
    %%% r(i,7) = TRANSLATIONAL VELOCITY IN X-DIRECTION
    %%% r(i,8) = TRANSLATIONAL VELOCITY IN Y-DIRECTION
    %%% r(i,9) = CHEMOTACTIC VELOCITY IN X-DIRECTION
    %%% r(i,10) = CHEMOTACTIC VELOCITY IN Y-DIRECTION
    %% GLOBAL VARIABLES
    global DUMP streamlined singlemotor FIXED_GRADIENT TYPE DISTRIBUTIONS ARROWS
    RODS TRACERS FREEZE_FRAMES right left
    global top bottom reflect_orientation stickywall left_stickywall_position Drot_natural Vt
    Dattractant SIGMA_d M
    global frameCap N dt W Wi Wip H Hi Hip LcX h_tophat baseV avifname LINEAR_DEFF
    global C_FINAL_INHIB C_FINAL DEFF_FINAL DROT_FINAL UADV_FINAL
    %% Initial Assignments
    outputname = ['Chemok02_sim01' pfname];
    addpath ./Parameter_Files
    tic
    parameter_function = str2func(pfname);
    parameter_function();

    if dt == 0.1
        theta_relator = 0.021; % for dt = 0.1, Drot = 0.021*Vtheta^2; Need to know this
        relationship for each different time step (determined using a lot of diffusion simulation data.
```



```

Y = zeros(GridPoints);
A = zeros(GridPoints);
if ARROWS == 1
    arrowTip = zeros(M,2);
end
if RODS == 1
    frontTip = zeros(M,2);
    backTip = zeros(M,2);
end
if TRACERS == 1
    Xtrace = zeros(M,N);
    Ytrace = zeros(M,N);
end
Movie1 = zeros(1,M);
end
%% %%% THE CODE:
for i = 1:M % Initial positions, speeds, & orientations.
    Vx = Vt*rand*sign(rand-rand);
    Vy = sqrt(Vt^2-Vx^2)*rand*sign(rand-rand); % sign(rand-rand) returns plus or minus
values at random.
    if DISTRIBUTIONS == 2
        if mod(i,2) == 1
            rold(i,:) = [0,i,Wi*rand+Wip,Hi*rand+Hip,360*rand,(Vtheta)*rand*sign(rand-
rand),Vx,Vy, 0, 0];% the r vector contains all information about the particle;
        else
            rold(i,:) = [0,i,Wi*rand+(W-Wip-Wi),Hi*rand+Hip,360*rand,(Vtheta)*rand*sign(rand-
rand),Vx,Vy, 0, 0];% the r vector contains all information about the particle;
        end
    elseif DISTRIBUTIONS == 1
        rold(i,:) = [0,i,Wi*rand+Wip,Hi*rand+Hip,360*rand,(Vtheta)*rand*sign(rand-rand),Vx,Vy,
0, 0];% the r vector contains all information about the particle;
    end
    if FIXED_GRADIENT == 1
        C = concentration_c(rold(i,3),SIGMA_d,TYPE,h_tophat,W,LcX,Umax,Umin);
        Vc = VELOCITY_FUNCTION(C,Umax,INHIBITOR);
    else
        Vc = chemotactic_velocity(Umax,INHIBITOR,rold(i,:),LcX,Dattractant,h_tophat,W);
% this is the chemotactic velocity component at the location where the particle is currently at, it
needs to be used to determine the path across which the fuel concentration must be integrated to
get the actual velocity.
    end
    [Vcx,Vcy] = Approx_Vc(dt,Vc,rold(i,:),Umax,INHIBITOR,LcX,h_tophat,
Dattractant,W,FIXED_GRADIENT,SIGMA_d,TYPE,Umin);
    if FIXED_GRADIENT == 1 %%% ESTABLISH CHEMOTACTIC EFFECT ON
ROTATIONAL DIFFUSIVITY
        C = concentration_c(rold(i,3),SIGMA_d,TYPE,h_tophat,W,LcX,Umax,Umin);
        if LINEAR_DEFF == 0
            Vtheta_chemo =
Drot_ROTATIONAL_FUNCTION(C,DrotMAX,ANGULAR_INHIBITOR,theta_relator);
        else
            if INHIBITOR == 1
                D_rot = interp1(C_FINAL_INHIB,DROT_FINAL, C,'nearest');
                Vtheta_chemo = sqrt(D_rot/theta_relator)*180/pi;
            else

```



```

        D_rot = interp1(C_FINAL,DROT_FINAL, C,'nearest');
        Vtheta_chemo = sqrt(D_rot/theta_relator)*180/pi;
    end
end
else
    if ANGULAR_INHIBITOR == 1
        Vtheta_chemo = -
chemotactic_velocity(VthetaMAX,0,rold(i,:),LcX,Dattractant,h_tophat,W);
    else
        Vtheta_chemo =
chemotactic_velocity(VthetaMAX,0,rold(i,:),LcX,Dattractant,h_tophat,W);
    end
end
rold(i,6) = (Vtheta+Vtheta_chemo)*rand*sign(rand-rand);
X_0(i) = rold(i,3);
Y_0(i) = rold(i,4);
theta_0(i) = rold(i,5);
if singlemotor == 1
    Rx(1) = rold(i,3);
    Ry(1) = rold(i,4);
    Theta(1) = rold(i,5);
end
end
CI(1) = 1;
if streamlined == 0
    for k = 1:GridPoints % This loop is for establishing X & Y for contour plots and for the
contours in the fixed gradient case.
        X(k,:) = linspace(-W/10,W+W/10,GridPoints);
        Y(:,k) = linspace(-H/10,H+H/10,GridPoints);
        if FIXED_GRADIENT == 1 % This loop is for plotting constant gradients on the contour
plots.
            A(1,k) = concentration_c(X(1,k),SIGMA_d,TYPE,h_tophat,W,LcX,Umax,Umin);
        end
    end
    movie_frame_captured_count = 0;
end
[NNNN(1,:),XXXX]=hist(rold(:,3),100);
for j = 2:N; % % % % This is the bulk of the code % % % %
    if streamlined == 0
        if FIXED_GRADIENT == 0 % % % CONTOUR PLOT CODE FOR TRANSIENT
GRADIENT
            for m = 1:GridPoints % This loop is for transient gradients (contour plots)
                A(1,m) = tophat_master(X(1,m),(j-1)*dt,h_tophat,W,Umax,Dattractant,LcX);
            end
        end
        for k = 2:GridPoints
            A(k,:) = A(1,:);
        end
    end
end
del_mean_L = 0;
del_theta = 0;
for i = 1:M
    Vx = Vt*rand*sign(rand-rand);

```

```

Vy = sqrt(Vt^2-Vx^2)*rand*sign(rand-rand);           % sign(rand-rand) returns plus or
minus values at random.
if FIXED_GRADIENT == 1
    C = concentration_c(roid(i,3),SIGMA_d,TYPE,h_tophat,W,LcX,Umax,Umin);
    Vc = VELOCITY_FUNCTION(C,Umax,INHIBITOR);
else
    Vc = chemotactic_velocity(Umax,INHIBITOR,roid(i,:),LcX,Dattractant,h_tophat,W);
% this is the chemotactic velocity component at the location where the particle is currently at, it
needs to be used to determine the path across which the fuel concentration must be integrated to
get the actual velocity.
end
[Vcx,Vcy] = Approx_Vc(dt,Vc,roid(i,:),Umax,INHIBITOR,LcX,h_tophat,
Dattractant,W,FIXED_GRADIENT,SIGMA_d,TYPE,Umin);
Vax = Vcx + (baseV)*cos(roid(i,5)*pi/180);           % Chemotaxis x-velocity
component.
Vay = Vcy + (baseV)*sin(roid(i,5)*pi/180);           % Chemotaxis y-velocity
component.
Uadv = sqrt(Vcx^2+Vcy^2);
if stickywall == 1;   %%%% STICKY WALL CASE
    if roid(i,3) <= left_sticywall_position
        r(i,:) = [(j-1)*dt,   i, left_sticywall_position ,   roid(i,4) ,   roid(i,5) + roid(i,6)*dt,
Vtheta*rand*sign(rand-rand),   Vx,   Vy, Vax,   Vay];
    else
        r(i,:) = [(j-1)*dt,   i,   roid(i,3) + Vx*dt + Vax*dt,   roid(i,4) + Vy*dt + Vay*dt,
roid(i,5) + roid(i,6)*dt,   Vtheta*rand*sign(rand-rand),   Vx,   Vy, Vax,   Vay];
    end
else
    r(i,:) = [(j-1)*dt,   i,   roid(i,3) + Vx*dt + Vax*dt,   roid(i,4) + Vy*dt + Vay*dt,
roid(i,5) + roid(i,6)*dt,   (Vtheta)*rand*sign(rand-rand),   Vx,   Vy, Vax,   Vay];
end
if FIXED_GRADIENT == 1
    if LINEAR_DEFF == 0
        Vtheta_chemo =
Drot_ROTATIONAL_FUNCTION(C,DrotMAX,ANGULAR_INHIBITOR,theta_relator);
    else
        if INHIBITOR == 1
            D_rot = interp1(C_FINAL_INHIB,DROT_FINAL, C,'nearest');
            Vtheta_chemo = sqrt(D_rot/theta_relator)*180/pi;
        else
            D_rot = interp1(C_FINAL,DROT_FINAL, 'nearest');
            Vtheta_chemo = sqrt(D_rot/theta_relator)*180/pi;
        end
    end
else
    if ANGULAR_INHIBITOR == 1
        Vtheta_chemo = -
chemotactic_velocity(VthetaMAX,0,r(i,:),LcX,Dattractant,h_tophat,W);
    else
        Vtheta_chemo =
chemotactic_velocity(VthetaMAX,0,r(i,:),LcX,Dattractant,h_tophat,W);
    end
end
r(i,6) = (Vtheta+Vtheta_chemo)*rand*sign(rand-rand);

```

```

    %%%%%%%%%% SIDE
WALLS%%%%%%%%%
    if right==1 && r(i,3)>W    %%%%%%%%%% RIGHT WALL CODE
% These conditional statements bound the particles to the box defined by W,H.
    r(i,3) = 2*W-r(i,3);      %%%%%%%%%% ***** HEY!!!! THESE DON'T
ACCOUNT FOR ANGLE CHANGES WITH WALL INTERACTIONS
    if reflect_orientation == 1
        r(i,5) = 180 - r(i,5);
    end
end
if left ==1 && r(i,3) < 0    %%%%%%%%%% LEFT WALL CODE
    r(i,3) = -r(i,3);
    if reflect_orientation == 1
        r(i,5) = 180 - r(i,5);
    end
end

if top == 1 && r(i,4)>H    %%%%%%%%%% TOP WALL CODE
    r(i,4) = 2*H-r(i,4);
    if reflect_orientation == 1
        r(i,5) = 360 - r(i,5);
    end
end
if bottom ==1 && r(i,4) < 0 %%%%%%%%%% BOTTOM WALL CODE
    r(i,4) = -r(i,4);
    if reflect_orientation == 1
        r(i,5) = 360 - r(i,5);
    end
end

%%%%%%%%%
% %%%%%%%%%%
    if streamlined == 0
        if ARROWS == 1
            arrowTip(i,:) =
[r(i,3)+ArrowLength*cos(r(i,5)*pi/180),r(i,4)+ArrowLength*sin(r(i,5)*pi/180)];
        end
        if RODS == 1
            frontTip(i,:) =
[r(i,3)+RodLength/2*cos(r(i,5)*pi/180),r(i,4)+RodLength/2*sin(r(i,5)*pi/180)];
            backTip(i,:) = [r(i,3)-RodLength/2*cos(r(i,5)*pi/180),r(i,4)-
RodLength/2*sin(r(i,5)*pi/180)];
        end
        if TRACERS == 1
            Xtrace(i,j) = r(i,3);
            Ytrace(i,j) = r(i,4);
        end
    end
    rold(i,:) = r(i,:);
    del_mean_L = del_mean_L + (sqrt((rold(i,4)-Y_0(i))^2+(rold(i,3)-X_0(i))^2))/M;    %%%%%%%%%
These values are used for determining the effective diffusion coefficient of the nanomotors.
    del_theta = del_theta + abs(r(i,5)-theta_0(i))/M;
end
del_theta_mean_squared(j) = (del_theta*pi/180)^2;          %%%%%%%%% [rad^2/s]

```

```

del_mean_L_squared(j) = del_mean_L^2;          %%% These values are used for
determining the effective diffusion coefficient of the nanomotors.
del_time(j) = rold(i,1);                       %%% These values are used for determining
the effective diffusion coefficient of the nanomotors.
if singlemotor == 1
    Rx(j) = rold(i,3);
    Ry(j) = rold(i,4);
    Theta(j) = rold(i,5);
end
CI(j) = chemotactic_index(rold(:,3),SIGMA_d,W,LcX);
if streamlined == 0
    if mod(j-1,N/frameCap) == 0 %%% %%% %%% MOVIE FRAMES CREATED
        mean_r_green = mean(abs(r(:,3)-LcX)+LcX);
        figure(1)
        set(gcf,'Color',[1 1 1]);
        set(gcf,'Position',[102 26 749 690]);
        [Yhist,YhistBin] = hist(r(:,4),M);
        subplot(2,2,2)
        plot(Yhist,YhistBin)
        set(gca,'Position',[0.798533 0.156522 0.15711 0.806159])
        set(gca,'XLim',[0,7.5])
        set(gca,'YLim',[-H/10,H+H/10])
        set(gca,'XTick',[])
        set(gca,'YTick',[])

        subplot(2,2,3)
        [NNNN(j,:),XXXX]=hist(rold(:,3),100);
        hist(r(:,3),100);
        set(gca,'Position',[0.056422 0.0173913 0.741976 0.142443])
        set(gca,'XLim',[-W/10,W+W/10])
        set(gca,'YLim',[0,200])
        set(gca,'XTick',[])
        set(gca,'YTick',[])
        hold on
        % plot([mean_r_green,mean_r_green],[0,7.5],'g') Not
        % sure what this green line is for, I do not recall, it is
        % from two years ago.
        % plot([LcX-(mean_r_green-LcX),LcX-(mean_r_green-LcX)],[0,7.5],'g')
        if FIXED_GRADIENT == 1
            plot(X(1,:),A(1,:)*7,'k') % in this case A is the nondimensional concentration from 0
            to 1.
        else
            plot(X(1,:),A(1,:)/Umax*7,'k'); % in this case A is the dimensional velocity from 0 to
            Umax.
        end
        hold off
        subplot(2,2,1)
        %%% %%% %%% Plot Chemotactic Contours
        contour(X,Y,A,100,':')
        set(gca,'PlotBoxAspectRatio',[W,H,1])
        set(gca,'Position',[0.00629285 0.156522 0.841812 0.805967])
        time_title = ['t = ' num2str((j-1)*dt) ' s'];

        title(time_title)

```

```

hold on
%%%%%%%% Plot Spheres
xwall_adjust = 1*W/100;
ywall_adjust = 3*H/100;
thickness = 3;
if RODS == 0
    plot(r(:,3),r(:,4),'o');
elseif RODS == 1
    for i = 1:M
        line([r(i,3),frontTip(i,1)],[r(i,4),frontTip(i,2)],'Color',[0 0 0],'LineWidth',1.5);
        line([r(i,3),backTip(i,1)],[r(i,4),backTip(i,2)],'Color',[1 .7 0],'LineWidth',1.5);
    end
end
if TRACERS == 1
    for i = 1:M
        plot(Xtrace(i,2:j),Ytrace(i,2:j),'b','LineWidth',1);
    end
end

if ARROWS == 1 %%%%%%%%% ARROWS CODE
    arrow([r(:,3),r(:,4)],arrowTip(:,:),'Length',5)
end

if bottom == 1 %%%%%%%%% BOTTOM WALL PLOT
    plot([-W/10,W+W/10],[-ywall_adjust,-ywall_adjust],'k','LineWidth',thickness)
% Complete bottom wall
%     plot([-xwall_adjust,W+xwall_adjust],[-ywall_adjust,-
ywall_adjust],'k','LineWidth',thickness) % bottom wall
end
if top == 1 %%%%%%%%% TOP WALL PLOT
    plot([-W/10,W+W/10],[H+ywall_adjust,H+ywall_adjust],'k','LineWidth',thickness)
% Complete top wall
%     plot([-
xwall_adjust,W+xwall_adjust],[H+ywall_adjust,H+ywall_adjust],'k','LineWidth',thickness)
% top wall
end
if left == 1 %%%%%%%%% LEFT WALL PLOT
    plot([-xwall_adjust,-xwall_adjust],[-H/10,H+H/10],'k','LineWidth',thickness)
% Complete Left wall
%     plot([-xwall_adjust,-xwall_adjust],[-
ywall_adjust,H+ywall_adjust],'k','LineWidth',thickness) % Left wall
end
if right == 1 %%%%%%%%% RIGHT WALL PLOT
    plot([W+xwall_adjust,W+xwall_adjust],[-H/10,H+H/10],'k','LineWidth',thickness)
% Complete Right wall
%     plot([W+xwall_adjust,W+xwall_adjust],[-ywall_adjust,H+ywa
%     ll_adjust],'k','LineWidth',thickness) %
%     Right wall for when other walls are present.
end
set(gca,'XLim',[-W/10,W+W/10])
set(gca,'YLim',[-H/10,H+H/10])
hold off
Movie1 = getframe(gcf);

```

```

mov1 = addframe(mov1,Movie1);
if FREEZE_FRAMES == 1
    if j == 2 || j == N
        fig_time = num2str(del_time(j));
        figNAME = [general_figure_name fig_time 'frame'];
        saveas(gcf,figNAME,'fig')
    elseif j >=N/2 && movie_frame_captured_count<1;
        movie_frame_captured_count = movie_frame_captured_count +1;
        fig_time = num2str(del_time(j));
        figNAME = [general_figure_name fig_time 'frame'];
        saveas(gcf,figNAME,'fig')
    end
end
end
end
end
end

save outputname CI NNNN XXXX

%% %% %% Single Particle Diffusivity
if singlemotor == 1
    for k = 1:N-1 % this loop cycles through the dt step size, this loop also determines the
    limit of applicable particles to be analyzed.
        count = 0;
        for j = 1:N-k
            count = count+1;
            R_squared(count) = (Rx(j)-Rx(j+k))^2 + (Ry(j)-Ry(j+k))^2;
            theta_squared(count) = ((Theta(j)-Theta(j+k))*pi/180)^2;
        end
        mean_squared_R(k) = mean(R_squared);
        mean_squared_theta(k) = mean(theta_squared);
        clear R;
        delta_t(k) = k*dt;
    end
    figure(2)
    plot(Rx,Ry,'ko')
    hold on
    plot(Rx,Ry)
    plot(Rx(1),Ry(1),'go')
    plot(Rx(N),Ry(N),'ro')
    hold off

    figure(3)
    plot(delta_t, mean_squared_R)
    ylabel('del L^2 (m^2)')
    xlabel('time (s)')
    title('Oversampled Data for a Single Particle')

    figure(4)
    plot(delta_t, mean_squared_theta)
    xlabel('time (s)')
    ylabel('del theta^2 (rad^2)')
    title('Oversampled Data for a Single Particle')

```

```

Diffusivity = polyfit(delta_t(1:round(N/10)),mean_squared_R(1:round(N/10)),1);
Deff_oversampled = Diffusivity(1)
Diffusivity = polyfit(delta_t(1:round(N/10)),mean_squared_theta(1:round(N/10)),1);
Drot_oversampled = Diffusivity(1)
matNAME = [general_figure_name '---Diffusivities_oversampled.mat'];
save(matNAME,'Deff_oversampled','Drot_oversampled')
end
%% %%%%%%%%%% DIFFUSIVITY PLOTS %%%%%%%%%%
if streamlined == 0
    mov1 = close(mov1);
    mean_r_green;
end

figure(5)
plot(del_time,del_mean_L_squared)
ylabel('del L^2 (m^2)')
xlabel('time (s)')
figure(6)
plot(del_time,del_theta_mean_squared)
xlabel('time (s)')
ylabel('del theta^2 (rad^2)')

Diffusivity = polyfit(del_time,del_mean_L_squared,1);
Deff = Diffusivity(1)
Diffusivity = polyfit(del_time,del_theta_mean_squared,1);
Drot = Diffusivity(1)
matNAME = [general_figure_name '---Diffusivities.mat'];
save(matNAME,'Deff','Drot')

if M > 1
    figure(7)
    size(del_time)
    size(CI)
    plot(del_time,CI)
    xlabel('time (s)')
    ylabel('CI')
    figNAME = [general_figure_name '---Chemotactic Index'];
    saveas(gcf,figNAME,'fig')
    matNAME = [general_figure_name '---Chemotactic Index.mat'];
    save(matNAME,'CI')
end
matNAME2 = [pname '---CI.mat'];
save(matNAME2,'CI')

toc

end

%% SUB-FUNCTIONS
function a = chemotactic_velocity(Umax,INHIBITOR,rold,LcX,Dattractant,h_tophat,W)
if INHIBITOR ==1;
    a = Umax - tophat_master(rold(3),rold(1),h_tophat,W,Umax,Dattractant,LcX);

```

```

else
    a = tophat_master(roid(3),roid(1),h_tophat,W,Umax,Dattractant,LcX);
end
end

function [Vcx,Vcy] =
True_Vc(dt,Vc,roid,Umax,SOURCES,SOURCE_TYPE,INHIBITOR,LcX,LcX2,LcY2,sigmaX,L
cY,sigmaY)
    %%% See page 16 in my 5th Lab Notebook
    Vcxo = Vc*cos(roid(5)*pi/180);    % initial chemotactic velocity in the x-direction
    Vcyo = Vc*sin(roid(5)*pi/180);
    dVc_dx =
Vcxderivative(Umax,SOURCES,SOURCE_TYPE,INHIBITOR,roid,LcX,LcX2,LcY2,sigmaX,Lc
Y,sigmaY)*cos(roid(5)*pi/180);    % x-derivative of chemotactic velocity (dVcxo/dx)
    Vcx = Vcxo + 1/2 * Vcxo*dVc_dx*cos(roid(5)*pi/180) * dt;
    Vcy = Vcyo + 1/2 * Vcxo*dVc_dx*sin(roid(5)*pi/180) * dt;
end

function [Vcx,Vcy] = Approx_Vc(dt,Vc,roid,Umax,INHIBITOR,LcX,h_tophat,
Dattractant,W,FIXED_GRADIENT,SIGMA_d,TYPE,Umin)
global LINEAR_DEFF C_FINAL UADV_FINAL
    %%% This function is an alternative to True_Vc used primarily to
    %%% validate True_Vc, in this case, Vcx and Vcy are determined by averaging over the Vc
value for the starting position, and the Vc value for the ending position if Vc were the only
velocity.
    Vcxo = Vc*cos(roid(5)*pi/180);    % initial chemotactic velocity in the x-direction
    Vcyo = Vc*sin(roid(5)*pi/180);
    roid(3) = roid(3)+Vcxo*dt;
    roid(4) = roid(4)+Vcyo*dt;
    if FIXED_GRADIENT == 1
        C = concentration_c(roid(3),SIGMA_d,TYPE,h_tophat,W,LcX,Umax,Umin);
        Vcf = VELOCITY_FUNCTION(C,Umax,INHIBITOR);
    else
        Vcf = chemotactic_velocity(Umax,INHIBITOR,roid,LcX,Dattractant,h_tophat,W);
    end
    Vcxf = Vcf*cos(roid(5)*pi/180);
    Vcyf = Vcf*sin(roid(5)*pi/180);
    Vcx = (Vcxo+Vcxf)/2;
    Vcy = (Vcyo+Vcyf)/2;
end

function c = concentration_c(x,SIGMA_d,TYPE,h,w,LcX,Umax,Umin)
    %%% This code was written on 10/06/2009 to establish a fixed concentration
    %%% gradient for use in batch mode chemotaxis analysis.

    Co = 1;
    if TYPE == 1
        numREFLECTIONS = 4;    % Number of wall reflections using Green's
function
        c = tophat(x - LcX,Co,h,SIGMA_d);
        for k = 1:numREFLECTIONS
            if mod(k,2) == 1 % if odd
                c = c + tophat(x - (k+1)*w+LcX,Co,h,SIGMA_d);    % Right Odd Reflections
            end
        end
    end
end

```



```

    c = c + tophat(x + (k-1)*w+LcX,Co,h,SIGMA_d);    % Left Odd Reflections
else
    c = c + tophat(x - k*w-LcX,Co,h,SIGMA_d);    % Right Even Reflections
    c = c + tophat(x + k*w-LcX,Co,h,SIGMA_d);    % Left Even Reflections
end
end
elseif TYPE == 2
    c = Co*exp(-(x-LcX)^2/(2*SIGMA_d^2));
elseif TYPE == 3
    c = Co;
elseif TYPE == 4
    c = 1 -x*(Umax-Umin)/(w*Umax);    % This is for a linear gradient in velocity with respect
to position.
end

end

function c=tophat_master(x,t,h,w,Co,D,LcX)
%% This is extracted from "testfile.m" the file used to test the time developing gradient used in
%% Chemotaxis. This code was written on 10/01/2009

d= sqrt(2*D*t);
numREFLECTIONS = 4;    % Number of wall reflections using Green's
function
c = tophat(x - LcX,Co,h,d);
for k = 1:numREFLECTIONS
    if mod(k,2) == 1 % if odd
        c = c + tophat(x - (k+1)*w+LcX,Co,h,d);    % Right Odd Reflections
        c = c + tophat(x + (k-1)*w+LcX,Co,h,d);    % Left Odd Reflections
    else
        c = c + tophat(x - k*w-LcX,Co,h,d);    % Right Even Reflections
        c = c + tophat(x + k*w-LcX,Co,h,d);    % Left Even Reflections
    end
end
end

function c = tophat(x,Co,h,d)
c = Co/2 * (erf((h-x)/(sqrt(2)*d)) + (erf((h+x)/(sqrt(2)*d))));
end

function Vc = VELOCITY_FUNCTION(C,Umax,inhibitor)    % This relates velocity to
concentration.
global C_FINAL_INHIB C_FINAL UADV_FINAL LINEAR_DEFF
if LINEAR_DEFF == 0
    if inhibitor == 1
        Vc = Umax*(1-C);    % LINEAR RELATIONSHIP CASE!
    else
        Vc = Umax*C;    % LINEAR RELATIONSHIP CASE!
    end
else
    if inhibitor == 1
        Vc = interp1(C_FINAL_INHIB,UADV_FINAL, 'nearest');
    else

```

```

    Vc = interp1(C_FINAL,UADV_FINAL, C,'nearest');
end
end

end

function VthetaC = ROTATIONAL_FUNCTION(C,VthetaMAX,inhibitor) %%% This relates
rotational velocity to concentration.
if inhibitor == 1
    VthetaC = -VthetaMAX*C; % LINEAR RELATIONSHIP CASE!
else
    VthetaC = VthetaMAX*C; % LINEAR RELATIONSHIP CASE!
end
end

function VthetaC = Drot_ROTATIONAL_FUNCTION(C,DrotMAX,inhibitor,theta_relator)
if inhibitor == 1
    VthetaC = -sqrt(DrotMAX*C/theta_relator)*180/pi; % LINEAR RELATIONSHIP CASE!
else
    VthetaC = sqrt(DrotMAX*C/theta_relator)*180/pi; % LINEAR RELATIONSHIP CASE!
end
end

function CI = chemotactic_index(r,SIGMA_d,w,LcX)
global TYPE
noise = 0;
signal = 0;
SIGMA_d = 2*SIGMA_d;
if TYPE == 1 || TYPE == 2 || TYPE == 3
    for i = 1:length(r)
        if r(i)<SIGMA_d || r(i)>(w-SIGMA_d)
            noise = noise+1;
        elseif r(i)> (LcX-SIGMA_d) && r(i)<(LcX+SIGMA_d)
            signal = signal + 1;
        end
    end
elseif TYPE == 4
    for i = 1:length(r)
        if r(i) < SIGMA_d
            noise = noise+1;
        elseif r(i)>(w-SIGMA_d)
            signal = signal + 1;
        end
    end
end
CI = signal/noise;
end

function name=value_name(aa)
if aa==0
    name = num2str(0);
else

```

```
bb = floor(log10(aa));
cc = aa*10^-bb;
dd = floor(cc);
ee = mod(cc,1);
ff = ee*100;
gg = num2str(ff,'%4.0f');
dd1 = num2str(dd);
bb1 = num2str(bb);
name = [dd1,'p',gg,'e',bb1];
end
end
```

APPENDIX C
COPYRIGHT RELEASE AGREEMENTS

APPENDIX C

COPYRIGHT RELEASE AGREEMENTS

Wiley-VCH Verlag GmbH & Co. KGaA

PERMISSION:

Dear Philip M. Wheat,

Thank you for your email.

We hereby grant permission for the requested use expected that due credit is given to the original source.

If material appears within our work with credit to another source, authorisation from that source must be obtained.

Credit must include the following components:

- Books: Author(s)/ Editor(s) Name(s): Title of the Book. Page(s). Publication year. Copyright Wiley-VCH Verlag GmbH & Co. KGaA. Reproduced with permission.

- Journals: Author(s) Name(s): Title of the Article. Name of the Journal. Publication year. Volume. Page(s). Copyright Wiley-VCH Verlag GmbH & Co. KGaA. Reproduced with permission.

With kind regards

Bettina Loycke

Bettina Loycke

Senior Rights Manager

Wiley-VCH Verlag GmbH & Co. KGaA

Boschstr. 12

69469 Weinheim

Germany

Phone: +49 (0) 62 01- 606 - 280

Fax: +49 (0) 62 01 - 606 - 332

Email: rights@wiley-vch.de

Wiley-VCH Verlag GmbH & Co. KGaA

Location of the Company: Weinheim

Chairman of the Supervisory Board: Stephen Michael Smith

Trade Register: Mannheim, HRB 432833

General Partner: John Wiley & Sons GmbH, Location: Weinheim

Trade Register Mannheim, HRB 432296

Managing Directors : Christopher J. Dicks, Bijan Ghawami, William Pesce

REQUEST:

TITLE: Powering Nanodevices with Biomolecular Motors

YEAR: 2004

AUTHORS: Hess, H., Bachand, G. D., and Vogel, V.

CONTENT: Figure 1

PAGE: 2111

The American Association for the Advancement of Science:

Dear Mr. Philip Wheat,

Thank you for placing your order through Copyright Clearance Center's RightsLink service. The American Association for the Advancement of Science has partnered with RightsLink to license its content.

Your order details and publisher terms and conditions are available by clicking the link below:

http://s100.copyright.com/CustomerAdmin/PLF.jsp?IID=2011031_1301515284693

Order Details

Licensee: Philip M. Wheat

License Date: Mar 30, 2011

License Number: 2638950444693

Publication: Science

Title: Powering an Inorganic Nanodevice with a Biomolecular Motor

Type Of Use: Thesis / Dissertation

Total: 0.00 USD

**THE AMERICAN ASSOCIATION FOR THE ADVANCEMENT OF SCIENCE
LICENSE
TERMS AND CONDITIONS**

Apr 15, 2011

This is a License Agreement between Philip M. Wheat ("You") and The American Association for the Advancement of Science ("The American Association for the Advancement of Science") provided by Copyright Clearance Center ("CCC"). The license consists of your order details, the terms and conditions provided by The American

Association for the Advancement of Science, and the payment terms and conditions.

All payments must be made in full to CCC. For payment instructions, please see information listed at the bottom of this form.

License Number	2638950444693
License date	Mar 30, 2011
Licensed content publisher	The American Association for the Advancement of Science
Licensed content publication	Science
Licensed content title	Powering an Inorganic Nanodevice with a Biomolecular Motor
Licensed content author	Ricky K. Soong, George D. Bachand, Hercules P. Neves, Anatoli G. Olkhovets, Harold G. Craighead, Carlo D. Montemagno
Licensed content date	Nov 24, 2000
Volume number	290
Issue number	5496
Type of Use	Thesis / Dissertation
Requestor type	Other Individual
Format	Print and electronic
Portion	Figure
Number of figures/tables	1
Order reference number	
Title of your thesis / dissertation	Collective Behavior of Swimming Bimetallic Motors in Chemical Concentration Gradients.
Expected completion date	Apr 2011
Estimated size(pages)	150
Total	0.00 USD


The Journal of cell biology

Order detail ID: 52983220 ISSN: 0021-9525 Publication year: 2011 Publication
Type: Journal Publisher: ROCKEFELLER UNIVERSITY PRESS Rightsholder:
ROCKEFELLER UNIVERSITY PRESS Author/Editor: Zigmond Your reference:
Wheat Dissertation

Permission Status: Granted

Permission type: Republish or display content Type of use: Republish in a
dissertation Requested use: Dissertation Republication title: Collective Behavior of
Swimming Bimetallic Motors in Chemical Concentration Gradients. Republishing
organization: Arizona State University Organization status: For-
profit Republication date: 04/11/2011 Circulation/ Distribution: 20000 Type of
content: Figure/ diagram/ table Description of requested content: Figure 3 Page
range(s): 609 Translating to: No Translation Requested content's publication date:
03/30/2011 Copy \$ 6.50

Journal of the American Chemical Society

- Order detail ID: 52982249
- Article Title: Synthetic Nanomotors in Microchannel Networks: Directional Microchip Motion and Controlled Manipulation of Cargo
- Author(s): Burdick, Jared
- DOI: 10.1021/JA803529U
- Date: Jul 01, 2008
- ISSN: 0002-7863
- Publication Type: Journal
- Volume: 130
- Issue: 26
- Start page: 8164
- Publisher: AMERICAN CHEMICAL SOCIETY]
- Author/Editor: AMERICAN CHEMICAL SOCIETY.
- Permission Status:  Granted
- Permission type: Republish or display content
- Type of use: reuse in a Thesis/Dissertation
-

Order License Id: 2638881170291
Order ref number: 10003

Are you the Author of original No
article?


Format Print and Electronic
Portion Table/Figure/Micrograph
Number of 1
Tables/Figures/Micrographs

Order reference number 10003

Title of the thesis / dissertation Collective Behavior of Swimming
Bimetallic Motors in Chemical
Concentration Gradients.

Expected completion date Apr 2011

Estimated size(pages) 150

- Order detail ID: 52982255
- Article Title: Catalytically Induced Electrokinetics for Motors and Micropumps
- Author(s): Baker, Paul T.
- DOI: 10.1021/JA0643164
- Date: Nov 01, 2006
- ISSN: 0002-7863
- Publication Type: Journal
- Volume: 128
- Issue: 46
- Start page: 14881
- Publisher: AMERICAN CHEMICAL SOCIETY]
- Author/Editor: AMERICAN CHEMICAL SOCIETY.
- Permission Status:  Granted
- Permission type: Republish or display content
- Type of use: reuse in a Thesis/Dissertation
-

Order License Id: 2638881193508

Are you the Author of original No
article?

Format Print and Electronic
Portion Table/Figure/Micrograph
Number of 1
Tables/Figures/Micrographs

Order reference number

Title of the thesis / dissertation Collective Behavior of Swimming
Bimetallic Motors in Chemical
Concentration Gradients.

Expected completion date Apr 2011

Estimated size(pages) 150

- Order detail ID: 52982268
- Article Title: Chemical Sensing Based on Catalytic Nanomotors: Motion-Based Detection of Trace Silver
- Author(s): Balasubramanian, Shankar
- DOI: 10.1021/JA905142Q
- Date: Sep 02, 2009
- ISSN: 0002-7863
- Publication Type: Journal
- Volume: 131
- Issue: 34
- Start page: 12082
- Publisher: AMERICAN CHEMICAL SOCIETY]
- Author/Editor: AMERICAN CHEMICAL SOCIETY.
- Permission Status: Granted
- Permission type: Republish or display content
- Type of use: reuse in a Thesis/Dissertation
-

Order License Id: 2638881235460

Are you the Author of original No
article?


Format Print and Electronic
Portion Table/Figure/Micrograph
Number of 1
Tables/Figures/Micrographs

Order reference number

Title of the thesis / dissertation Collective Behavior of Swimming
Bimetallic Motors in Chemical
Concentration Gradients.

Expected completion date Apr 2011

Estimated size(pages) 150

- Order detail ID: 52982259
- Article Title: Carbon-Nanotube-Induced Acceleration of Catalytic Nanomotors
- Author(s): Burdick, Jared
- DOI: 10.1021/NN800154G
- Date: May 01, 2008
- ISSN: 1936-0851
- Publication Type: Journal
- Volume: 2
- Issue: 5
- Start page: 1069
- Publisher: AMERICAN CHEMICAL SOCIETY
- Author/Editor: American Chemical Society.
- Permission Status:  Granted
- Permission type: Republish or display content
- Type of use: reuse in a Thesis/Dissertation
-

Order License Id: 2638881215992

Are you the Author of original No
article?

Format Print and Electronic
Portion Table/Figure/Micrograph
Number of 1
Tables/Figures/Micrographs


Order reference number

Title of the thesis / dissertation Collective Behavior of Swimming
Bimetallic Motors in Chemical
Concentration Gradients.

Expected completion date Apr 2011

Estimated size(pages) 150

Langmuir : the ACS journal of surfaces and colloids

- Order detail ID: 52982240
- Article Title: Rapid Fabrication of Bimetallic Spherical Motors
- Author(s): Marine, Nathan A.
- DOI: 10.1021/LA102218W
- Date: Aug 17, 2010
- ISSN: 0743-7463
- Publication Type: Journal
- Volume: 26
- Issue: 16
- Start page: 13052
- Publisher: AM CHEM SOC
- Author/Editor: American Chemical Society.
- Permission Status:  Granted
- Permission type: Republish or display content
- Type of use: reuse in a Thesis/Dissertation
-

Order License Id: 2638880446136
Order ref number: 10006

Are you the Author of Yes
original article?

Format Print and Electronic
Portion 50% or more of original article


Order reference number 10006

Title of the thesis / Collective Behavior of Swimming Bimetallic
dissertation Motors in Chemical Concentration Gradients.

Expected completion Apr 2011
date

Estimated size(pages) 150

ACS nano

- Order detail ID: 52981726
- Article Title: Carbon-Nanotube-Induced Acceleration of Catalytic Nanomotors
- Author(s): Burdick, Jared
- DOI: 10.1021/NN800154G
- Date: May 01, 2008
- ISSN: 1936-0851
- Publication Type: Journal
- Volume: 2
- Issue: 5
- Start page: 1069
- Publisher: AMERICAN CHEMICAL SOCIETY
- Author/Editor: American Chemical Society.
- Permission Status:  Granted
- Permission type: Republish or display content
- Type of use: reuse in a Thesis/Dissertation
-

Order License Id: 2638880310548

Are you the Author of original No article?

Format Print and Electronic
Portion Table/Figure/Micrograph
Number of 1
Tables/Figures/Micrographs


Order reference number

Title of the thesis / dissertation Collective Behavior of Swimming Bimetallic Motors in Chemical Concentration Gradients.

Expected completion date Apr 2011

Estimated size(pages) 150

Nano letters

- Order detail ID: 52980295
- Article Title: Catalytic Motors for Transport of Colloidal Cargo
- Author(s): Crespi, Vincent H.
- DOI: 10.1021/NL072275J
- Date: May 01, 2008
- ISSN: 1530-6984
- Publication Type: Journal
- Volume: 8
- Issue: 5
- Start page: 1271
- Publisher: AMERICAN CHEMICAL SOCIETY
- Author/Editor: American Chemical Society.
- Permission Status:  Granted
- Permission type: Republish or display content
- Type of use: reuse in a Thesis/Dissertation
-

Order License Id: 2638861241032

Order ref number: 10002

Are you the Author of original No
article?

Format Print and Electronic
Portion Table/Figure/Micrograph
Number of 1
Tables/Figures/Micrographs

Order reference number 10002

Title of the thesis / dissertation Collective Behavior of Swimming
Bimetallic Motors in Chemical
Concentration Gradients.

Expected completion date Apr 2011

Estimated size(pages) 150

The Royal Society of Chemistry

Dear Philip

The Royal Society of Chemistry hereby grants permission for the use of the material specified below in the work described and in all subsequent editions of the work for distribution throughout the world, in all media including electronic and microfilm. You may use the material in conjunction with computer-based electronic and information retrieval systems, grant permissions for photocopying, reproductions and reprints, translate the material and to publish the translation, and authorize document delivery and abstracting and indexing services. The Royal Society of Chemistry is a signatory to the STM Guidelines on Permissions (available on request).

Please note that if the material specified below or any part of it appears with credit or acknowledgement to a third party then you must also secure permission from that third party before reproducing that material.

Please ensure that the published article carries a credit to The Royal Society of Chemistry in the following format:

[Original citation] – Reproduced by permission of The Royal Society of Chemistry

and that any electronic version of the work includes a hyperlink to the article on the Royal Society of Chemistry website. The recommended form for the hyperlink is <http://dx.doi.org/10.1039/DOI> suffix, for example in the link <http://dx.doi.org/10.1039/b110420a> the DOI suffix is 'b110420a'. To find the relevant DOI suffix for the RSC paper in question, go to the Journals section of the website and locate your paper in the list of papers for the volume and issue of your specific journal. You will find the DOI suffix quoted there.

Best wishes

Gill

Gill Cockhead (Mrs), Contracts & Copyright Executive
Royal Society of Chemistry, Thomas Graham House
Science Park, Milton Road, Cambridge CB4 0WF, UK
Tel +44 (0) 1223 432134, Fax +44 (0) 1223 423623
<http://www.rsc.org>

-----Original

From:

pmwheat@cox.net

Message-----

[\[mailto:pmwheat@cox.net\]](mailto:pmwheat@cox.net)

Sent: 29 March 2011 20:44
To: CONTRACTS-COPYRIGHT (shared)
Subject: Permission Request Form: Philip M. Wheat

Name : Philip M. Wheat
Address :

633 W. Southern Ave
Unit 1121
Tempe, AZ 85282

Tel : 1-602-577-1180
Fax :
Email : pmwheat@cox.net

I am preparing the following work for publication:

Article/Chapter Title : Collective Behavior of Swimming Bimetallic Motors in
Chemical Concentration Gradients.
Journal/Book Title : PhD Dissertation
Editor/Author(s) : Philip M. Wheat
Publisher : Arizona State University

I would very much appreciate your permission to use the following material:

Journal/Book Title : Chemical Communications/Electrochemically-triggered
motion of catalytic nanomotors
Editor/Author(s) : Manesh, K. M., Kagan, D., Balasubramanian, S., Cardona,
M., Flechsig, G. U., Posner, J., Wang, J.
Volume Number :
Year of Publication : 2009
Description of Material : Figure 1, SI Figure 1, SI Scheme 1
Page(s) : 4509, SI 4, SI 6
Journal/Book Title : Chemical Communications/6) Synthetic self-propelled
nanorotors
Editor/Author(s) : Fournier-Bidoz, S., Arsenault, A. C., Manners, I., Ozin, G.
A.
Volume Number :
Year of Publication : 2004
Description of Material : Figure 2
Page(s) : 442
Journal/Book Title : Lab on a Chip/T cell chemotaxis in a simple microfluidic

device
Editor/Author(s) : Lin, F., Butcher, E. C.
Volume Number : 6
Year of Publication : 2006
Description of Material : Figure 1
Page(s) : 1464

Any Additional Comments :

SI in the first reference refers to the supplemental information.

DISCLAIMER:

This communication (including any attachments) is intended for the use of the addressee only and may contain confidential, privileged or copyright material. It may not be relied upon or disclosed to any other person without the consent of the RSC. If you have received it in error, please contact us immediately. Any advice given by the RSC has been carefully formulated but is necessarily based on the information available, and the RSC cannot be held responsible for accuracy or completeness. In this respect, the RSC owes no duty of care and shall not be liable for any resulting damage or loss. The RSC acknowledges that a disclaimer cannot restrict liability at law for personal injury or death arising through a finding of negligence. The RSC does not warrant that its emails or attachments are Virus-free: Please rely on your own screening.



April 14, 2011

Philip M. Wheat
Philip.Wheat@asu.edu

Ref # 10185

Thank you for your permission request dated on April 11, 2011. We are pleased to grant you a non-exclusive, non-transferable permission, English rights, limited to **print and electronic format**, provided you meet the criteria outlined below. Permission is for a one-time use and does not include permission for future editions, updates, databases, translations, or any other matters. Permission must be sought for each additional use. This permission does not include the right to modify APS material.

Please print the required copyright credit line on the first page that the material appears: "Reprinted (abstract/excerpt/figure) with permission from [FULL REFERENCE CITATION] as follows: authors names, journal title, volume number, page number and year of publication. Copyright (YEAR) by the American Physical Society.

The following language must appear somewhere on the website: "Readers may view, browse, and/or download material for temporary copying purposes only, provided these uses are for noncommercial personal purposes. Except as provided by law, this material may not be further reproduced, distributed, transmitted, modified, adapted, performed, displayed, published, or sold in whole or part, without prior written permission from the American Physical Society."

Provide a hyperlink from the reprinted APS material (the hyperlink may be embedded in the copyright credit line). APS's link manager technology makes it convenient and easy to provide links to individual articles in APS journals. For information, see: <http://link.aps.org/>

You must also obtain permission from at least one of the authors for each separate work, if you haven't done so already. The author's name and address can be found on the first page of the published Article.

Use of the APS material must not imply any endorsement by the American Physical Society.

Permission is granted for use of the following APS material only

Fig. 1, Phys. Rev. E Vol. 81, 065302 (2010)
Fig. 2, Phys. Rev. E Vol. 75, 011503 (2007)
Fig. 1, Phys. Rev. Lett. Vol. 104, 138302 (2010)
Fig. 4, Phys. Rev. Lett. Vol. 99, 048102 (2007)

Permission is limited to the single title specified or single edition of the publication as follows:
A PhD dissertation entitled "Collective Behavior of Swimming Bimetallic Motors in Chemical Concentration Gradients" to be published by Arizona State University.

If you have any questions, please refer to the Copyright FAQ at: <http://publish.aps.org/copyrightFAQ.html> or send an email to assocpub@aps.org

Sincerely,

Eileen LaManca
Publications Marketing Coordinator